Vortices in sinusoidal shear, with applications to Jupiter

by

Rohith Vilasur Swaminathan

Submitted to the Joint Program in Physical Oceanography
in partial fulfillment of the requirements for the degree of

Master of Science in Physical Oceanography

at the

MASSACHUSETTS INSTITUTE OF TECHNOLOGY

and the

WOODS HOLE OCEANOGRAPHIC INSTITUTION

June 2016

Author .....

Joint Program in Physical Oceanography
Massachusetts Institute of Technology
& Woods Hole Oceanographic Institution
February 16, 2016

Certified by .....

Glenn R. Flierl
Professor of Physical Oceanography
Massachusetts Institute of Technology
Thesis Supervisor

Accepted by .....

Larry J. Pratt
Senior Scientist
Woods Hole Oceanographic Institution
Chairman, Joint Committee for Physical Oceanography

Vortices in sinusoidal shear, with applications to Jupiter

by

Rohith Vilasur Swaminathan

Submitted to the Joint Program in Physical Oceanography
Massachusetts Institute of Technology
& Woods Hole Oceanographic Institution
on February 16, 2016, in partial fulfillment of the
requirements for the degree of
Master of Science in Physical Oceanography

Abstract

In this thesis, we have studied the existence of vortex steady states in a sinusoidal background shear flow in a 1.75 layer quasi-geostrophic model. Trying to find vortex structures by integrating the Hamiltonian system has the drawback that the vortices lose enstrophy by filamentation and numerical dissipation, while continuing to deform and wobble. Adopting the local optimization technique of Hamiltonian Dirac Simulated Annealing overcomes this drawback and allows us to obtain steady/quasi-steady vortices that have roughly the same area as that of the initial vortex. The steady states that we have generated range from elliptical with major axis aligned with the flow in the prograde shear region to triangular at the latitude where prograde and adverse shear meet and back to elliptical but with the major axis aligned perpendicular to the shear flow at the center of the adverse shear region. The steady states calculated by the above technique can be used for further analysis and as an initial condition to study the merger of vortices in background shear. This result is directly applicable to the kind of dynamics visible on planets like Jupiter, where vortices residing in zonal shear are a common occurrence.

Thesis Supervisor: Glenn R. Flierl
Title: Professor of Physical Oceanography
Massachusetts Institute of Technology

Acknowledgments

To begin with, I am extremely grateful to Prof. Glenn Flierl for agreeing to be my advisor under difficult circumstances. I would like to think that I struck the jackpot by getting a chance to work with Glenn. The combination of the two qualities of intelligence and niceness is very hard to come by in such a competitive environment, and I think Glenn is without a shadow of doubt one of the most intelligent and nicest guys in EAPS. Glenn has always been extremely supportive of me in difficult times, and has always backed me when needed. Further, he has always been encouraging and has exercised a great deal of patience when I have approached him with doubts and questions. I am astonished at his breadth and depth of knowledge in the fields of Physics, Oceanography and Meteorology . It is no wonder that many young professors in the EAPS department look up to Glenn. I feel MIT and EAPS are very lucky to have Glenn as a Professor.

During my time as a graduate student in the MIT/WHOI Joint program, I have come to realize that funding or financial security is the single most important thing for conducting good research. In this regard, I would like to express my gratitude to Prof. Raffaele Ferrari for giving me the opportunity to TA his course on the General Circulation of the Oceans. I am also grateful to Dr. Saif Rayyan for taking me on as a TA for the EdX Classical Mechanics course. I must mention that I got both my Teaching Assistantships in times of desperate need. Further, I am grateful to the Department of Earth Atmospheric and Planetary Sciences for awarding a Fellowship for two full semesters. In addition, I would like to thank the graduate committee for being extremely patient with me.

I would like to thank Jason Mcknight for being extremely kind, helpful and comforting when I needed it the most. Further, I would like to thank Vicki Mckenna and Ronni Schwartz for being extremely helpful and understanding in times of duress.

Of course, no acknowledgement is complete without the mention of friends. During my time in Boston/Cambridge, I have met a lot of interesting characters and shared a

ton of laughs. I truly enjoyed my time in my apartment in Tang Hall with my roommates Srinivas, Sanket, Karthik, Shaswat, Anshul, Pranay, Murthy and Paramveer. I will definitely miss the view and Marilyn Monroe. Next, I would like to mention my friends from EAPS, Dan and Deepak, both of whom have listened patiently to me and given excellent advise. Further, I would like to mention Brian, Joern, Diamy, Flora and Dana, all of whom made the coursework at MIT more interesting. Finally, a shout out to the homies Advith, Harish, Aanand, Ankur, Dheeman, Goutham and Bhuvan for keeping me company on google hangouts and .

Last but not the least, I would like to thank my brother Vikhram, my sister Yamini and my parents Uma and Swaminathan for their unwavering support and encouragement. I dedicate this thesis to all students who have gone through hell and beyond during their graduate program.

Contents

List of Figures

List of Tables

Chapter 1

Introduction

1.1 Motivation

The phenomenon of long lived vortices embedded in shear flows is ubiquitous in nature. What better example can one think of than the Great Red Spot (GRS) on Jupiter? The GRS is a giant anticyclonic (opposite to the direction of rotation of planet) storm or vortex at roughly $22°S$ latitude, roughly the size of two to three earths, that has been raging for at least the last 400 years. What makes it truly remarkable is the fact that this vortex has been surviving in the presence of a strong background shear flow and turbulence. This behavior is attractive to both the communities of fluid dynamicists who are interested in fundamental turbulence research, as well as of the meteorologists and oceanographers who are more concerned with applied research. Apart from the GRS, there are several other vortices on Jupiter (like the White Oval), which have been displaying a similar behavior to the GRS, albeit not on such a large scale. These vortices reside on east-west or zonal shear flows, the latter (like the former) being a common occurrence on planets like Jupiter, Neptune and Saturn (Ingersoll, 1990). The source of such East-West flows is a highly contested point among the research community with several speculative theories being advanced, the most convincing one being on baroclinic instabilities. For now, we are only concerned about the interaction between the vortex and the background

shear flow, which is a highly non-linear process.

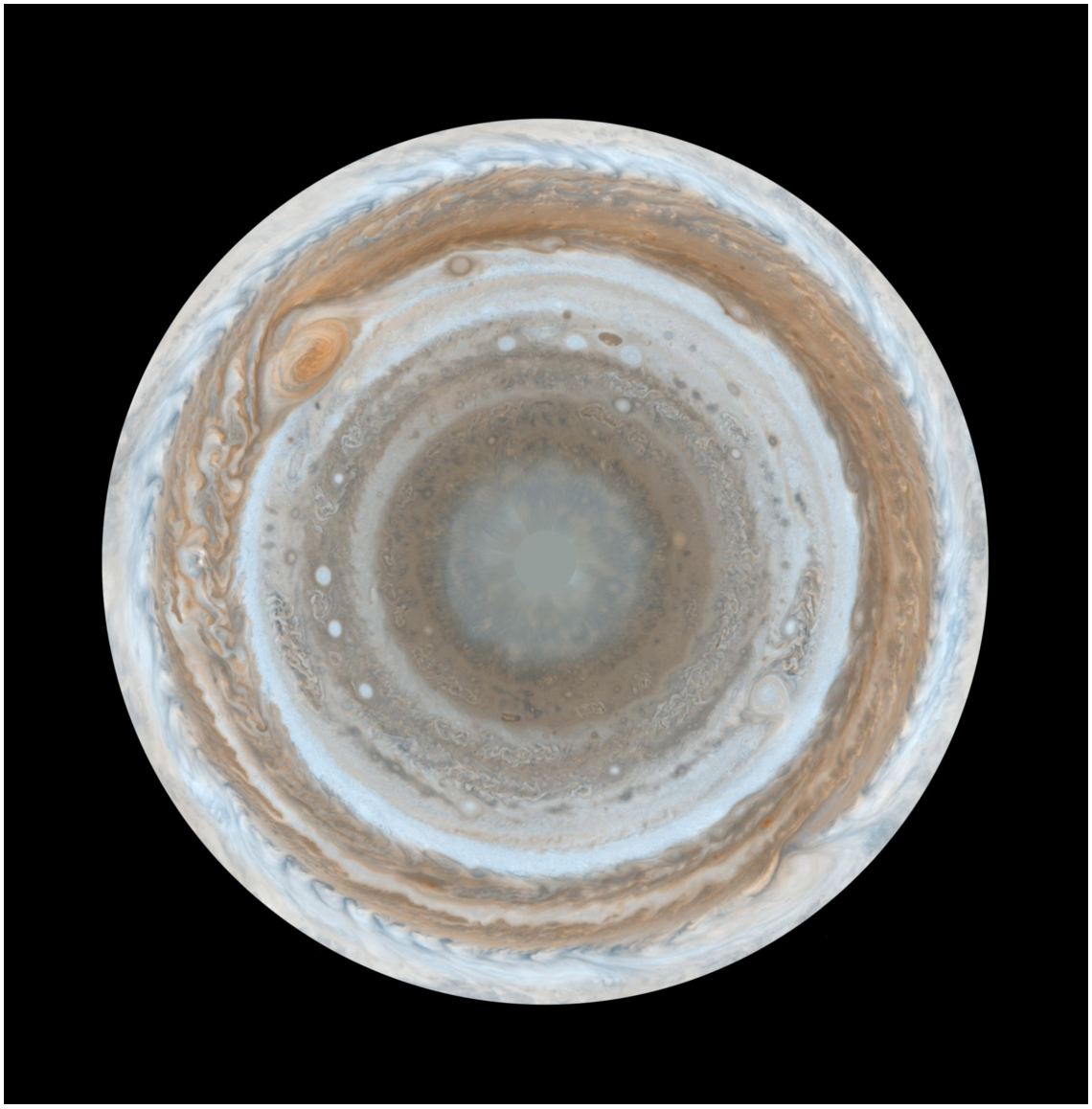

Figure 1-1: The most detailed color map of Jupiter constructed constructed from images taken by Cassini on Dec. 11 and 12, 2000, as the spacecraft neared Jupiter during a flyby on its way to Saturn. Source: http://www.nasa.gov/

Another important unknown is the vertical structure of the zonal flows as well as the GRS. As will be discussed later, this question will turn out to be another source of speculation. The other interesting fact about Jovian vortices is that of the shape of the vortex, which seems to be roughly oval or elliptical at first sight (Smith et al., 1979a,b). On further analysis from observations and data, we in fact find that the

vortices are a hybrid of the $m = 2$ (elliptical) and $m = 3$ (triangular) modes. Further, of late the GRS has also been on a downward trend as far as its size is concerned (Simon-Miller et al., 2002). Therefore, we have many posed many questions and are in pursuit of answers.

One of the popular theories explaining the persistence of the GRS and other vortices is that of vortex merger, a highly complicated non-linear interaction phenomenon of two or more vortices combining to form a larger vortex. This theory basically argues that a parent vortex like the GRS feeds on vortices of smaller or similar size, balancing the enstrophy loss due to dissipative and other processes. The reason this theory has received so much weight is mainly the direct observations of the phenomenon of vortex merger leading to an increase in size of the parent vortex, especially as those seen in the Voyager images (Mac Low and Ingersoll, 1986; Smith et al., 1979a,b). However, the basic premise of the theory is the presence of smaller vortices or eddies in the first place. Once again the source of such vortices is highly debatable, with equally convincing arguments in favor of a theory on moist convection (Ingersoll et al., 2000) giving rise to vortical flows as well as that on instabilities of the zonal shear flow giving rise to vortices. For now, we again turn a blind eye to this gaping hole, and lay our belief in observations, which clearly indicate the continuous appearance of vortices the size of the deformation radius. Placing our faith in the vortex merger theory, we would like to understand more about it order to answer some of the questions posed earlier. Thus, we would like to seed shear flows with vortices and observe how they merge. Our aim here is to first use a simple mathematical model and initial conditions in order to capture the basic physics in the problem. In order to do so, we first need to find steady or quasi-steady solutions of vortices embedded in shear flow.

The rest of Chapter 1 is dedicated to a literature review of the most relevant models and numerical simulations attempting to capture the physics of Jovian vortices embedded in background shear flows. In Chapter 2, we present the mathematical model adopted by us, the 1.75 layer Quasi-geostrophic model, and proceed to adopt a

relatively novel numerical optimization technique called simulated annealing in conjunction with the standard spatial and temporal numerical discretization schemes to solve this problem. Chapter 3 contains all the results and discussion from the numerical simulations for finding the steady states. We finally conclude in Chapter 4.

1.2 Literature

The rapid rotation (roughly 10 hours) of Jupiter had led Hide (1961) and Ingersoll (1969) to follow the Taylor-Proudman theorem and suggest that the GRS is a Taylor column or a fluid flow feature that is fixed to topographical feature. A few years later however, details of Jupiter's magnetic field led to the theory being debunked. Maxworthy and Redekopp (1976) proposed a solitary wave model for the GRS using a one layer beta plane quasi-qeostrophic framework. Here, they argued that the GRS is a soliton or a weakly non-linear solitary wave in zonal shear flows. Assuming the radius of curvature of background flow to be lesser than the radius of deformation ($L^2 < R_d^2$), they looked for neutral solutions in the long wavelength limit (the finite wavelength case made the background shear flow unstable). One of the main criticisms of this model, as pointed out by Ingersoll and Cuong (1981), was the inability for the solitons to interact in a way that is characteristic of Jovian vortices. The solitons obtained could not change shape or size and did not merge during soliton-soliton interactions.

Moore and Saffman (1971) found the steady states of line vortices in background irrotational strain and simple shear. In the case of simple shear, they were able to obtain a single steady elliptical shape for the prograde case (vortex and shear rotation in same sense) with the major axis parallel to the background flow, and two solutions elliptical shapes for the retrograde case (vortex and shear rotation in opposite sense) with the major axis perpendicular to the background flow - the less elongated one steady and the other unsteady. Kida (1981) analysed the unsteady

motion of an elliptic vortex of uniform vorticity in a uniform straining and vorticity flow in a barotropic system, and calculated solutions that precess, nutate, are steady (which came out as a special case of the unsteady solutions), or elongate. He also found the vortices to be area preserving, although it must be pointed out that he did not perform any stability analysis (unsteady elliptic vortices can break up into smaller vortices). Meacham et al. (1989) showed that these unsteady motions became unstable when the vortex elongated sufficiently.

Ingersoll and Cuong (1981) made the first attempt at trying to model Jovian vortices as isolated disturbances or eddies confined to a shallow upper layer embedded in a shear flow which extended down to an infinitely deep bottom layer (1.75 layer quasi-qeostrophic model). By assuming the radius of curvature of background flow to be greater than the radius of deformation ($L^2 > R_d^2$), their flow was rendered stable and they were able to obtain steady isolated vortex states (Using a scaling analysis and anelastic equations, Ingersoll and Pollard (1982) showed that the winds in Jupiter extend deep into the interior and take the system close to marginal stability.). Although Ingersoll and Cuong (1981) were able to show that vortices in background shear can interact, merge and change in shape and size, they also found vortex steady states translating at a velocity different from that of the background flow ($c \neq \bar{u}$). This clearly cast a doubt on their far-field assumptions and suggested the presence of non-linearities and transient effects, something they themselves acknowledged. Although they claim to have conducted a grid independence study, a 64×64 grid is arguably small, especially when they were attempting to resolve vortices which were much smaller than the domain size. However, they were probably constrained by the technology of the day. Further, they were able to observe some undesirable boundary effects in a few of their simulations. They were unable to shed any light on the shape or structure of the vortices, probably because they had very few grid points. In addition, they had issues is filtering out the ejected disturbances when calculating the eddy kinetic and potential energies. Next, by analyzing the velocity field from the Voyager images, Dowling and Ingersoll (1988) and Dowling and Ingersoll (1989)

(the former employing quasi-geostrophy and the latter employing shallow water) followed the absolute vorticity along the fluid streamlines to measure the structure of potential temperature surfaces in Jupiter's atmosphere. They found that the fluid in the deep lower layer has a zonal velocity that varies with latitude. Further these velocities although not exactly the same as that of the thin upper layer, were still in the same ball park. However, they questioned the $L^2 > R_d^2$ criterion used by Ingersoll and Cuong (1981) governing the compactness of vortices and suggested the presence of standing Rossby waves.

Marcus (1988), Sommeria et al. (1988) and Marcus (1990) attempted to model the GRS by conducting experiments in a rapidly rotating annulus. In all their works, they were able to capture the merger of smaller vortices to finally form a single giant vortex of roughly uniform potential vorticity. Marcus (1990) mainly found that vortices in prograde shear formed steady states while vortices in adverse shear became elongated and got expelled towards a region of prograde shear if present, and also tore apart in many cases as a consequence of the Kelvin-Helmholtz instability. In addition, he found that the vortices merged only when the radial separation of vortices was below a critical value. We must however remember that the quasi-geostrophic numerical simulations of Marcus (1988) and Marcus (1990) assumed a uniform background potential vorticity for most of the simulations, attributing potential vorticity homogenization along the way. He also defends his choice with the argument that the vortices cannot affect the uniform potential vorticity background. Although the potential vorticity of Jovian vortices like the GRS is roughly uniform (Rhines and Young (1982) potential vorticity (PV) homogenization in closed streamlines) with a sharp drop at the edges, the background flow has many changes of sign of PV gradient as seen in observations. Next, the dynamics is clearly influenced by the inner and outer walls of the annulus, especially in the case of infinite radius of deformation R_d. Further, while Marcus (1988) adopted a reduced gravity model with a constant deep flow and a linearly sloping bottom mimicking the β plane, Marcus (1990) ran simulations for a one layer model with a linearly sloping bottom. Also, the former

assigned uniform PV for the initial state of vortices (in line with observations) while the latter input uniform vorticity (generally not observed). We must also remember that it is difficult to compare the shapes of the final steady vortices with that of observations because of geometric considerations for polar coordinates. Sommeria et al. (1988) complemented the work done by Marcus by conducting laboratory simulations in a rigidly rotating annulus with a sloping bottom. The novelty in their problem was the Ekman friction and spindown, due to which they had to pump water from holes in the bottom, which lead to a counter-rotating jet by the action of Coriolis. In addition, they obtained some interesting secondary circulations in their system due to the effect of Ekman pumping, albeit with negligible effects on the dynamics. Finally, they were able to obtain vortices through the instability of the jets, which in turn gave rise to mergers and a single giant vortex for high pumping rates (similar to that observed in numerical simulations of Marcus).

Marcus (1993) summarized the work done by the research community on modeling the GRS till 1993, and appended some of his numerical experiments. First, assuming infinite R_d and a quadratic velocity profile, he found found steady states of uniform vorticity vortices ranging from elliptical to roughly triangular (or asymmetrical ellipse with a stagnation point at the top). Next, considering the finite R_d case for a cubic velocity profile, he found two families of vortices analogous to the previous case, and called them corner-like (with stagnation point) and band-like (without stagnation point). They key point he is that he realized that the background profile had to have a curvature in it to give realistic vortex shapes.

Zonal and meridional velocity profiles (Choi et al., 2007; Dowling and Ingersoll, 1988) show that most of the the vorticity is concentrated in a thing ring away from the axis of rotation. This would correspond to a Rankine like profile for the potential vorticity in a QG system. Further, the maximum Rossby number for the GRS and White Oval has been found to be around 0.35 (Mitchell et al., 1979, 1981). And more importantly, we have talked about many studies in the literature that have justified the assumption that the zonal velocity extends deep into the interior. Hence, we

adopt a 1.75 layer quasi-geostrophic model with initial conditions of a vortex (with a potential vorticity profile close that of a Rankine profile – uniform PV in the interior) embedded in a sinusoidal shear flow for our studies and simulations.

Chapter 2

Governing equations and numerical methodology

2.1 1.75 layer Quasi-geostrophic equations

First, we consider a two-layer stably stratified fluid system with a rigid lid at the top and bottom. Assuming the horizontal scales to be much greater than the vertical scales, we can make the hydrostatic approximation for each layer. Further, we assume the layer thickness variations to be much smaller than the mean depth of each layer. Finally, making the small Rossby number approximation ($Ro = \frac{\zeta}{f} = \frac{U}{fL} =$ where U is the velocity scale, L is the length scale, ζ is the vorticity scale of the flow and f is the planetary vorticity), we can write down the two-layer Quasi-geostrophic potential vorticity equations following Pedlosky (1987) as

$$q_1 = \nabla^2\psi_1 + \beta y + F_1\left(\psi_2 - \psi_1\right), \tag{2.1}$$

$$q_2 = \nabla^2\psi_2 + \beta y + F_2\left(\psi_1 - \psi_2\right), \tag{2.2}$$

$$\frac{\partial}{\partial t}q_i + [\psi_i, q_i] = 0, \qquad i = 1, 2\ ; \tag{2.3}$$

where q_i is the potential vorticity of each layer, ψ_i is the streamfunction of each layer, $[\ ,\ ]$ is the Jacobian operator and $F_1 + F_2 = \dfrac{1}{{R_d}^2} = \dfrac{f_o^2}{g'}\dfrac{(H_1+H_2)}{H_1 H_2}$ and $\dfrac{F_2}{F_1} = \dfrac{H_1}{H_2}$ (R_d is the deformation radius, $g' = g\dfrac{\Delta\rho}{\rho}$ is the reduced gravity and H_i is the layer thickness). Now, assuming that the bottom layer (layer 2) is infinitely deep ($\delta = \dfrac{H_1}{H_2} \to 0$) and starting with flow given by $\psi_2(y)$ which will remain steady, we get the 1.75 layer QG equations as

$$q_1 = \nabla^2\psi_1 + \beta y + F\left(\psi_2 - \psi_1\right), \tag{2.4}$$

$$q_2 = \nabla^2\psi_2 + \beta y, \tag{2.5}$$

$$\frac{\partial}{\partial t}q_1 + [\psi_1, q_1] = 0; \tag{2.6}$$

with the radius of deformation $R_d = \dfrac{\sqrt{g'H_1}}{f_o}$and $F = F1 = \dfrac{1}{R_d^2}$. We can clearly observe that the infinitely deep bottom layer does not evolve with time, although it does have a flow (unlike the equivalent barotropic model which starts out and stays without any bottom layer flow).

2.2 Simulated annealing

Simulated annealing is a method for solving constrained and unconstrained optimization problems. As the name suggests, we can draw an analogy with annealing in Materials science, which is basically the process of heating a material and then cooling at a slow rate, thereby reducing the defects and minimizing the energy of the system. In simulated annealing, the slow cooling corresponds to a slow decrease in the probability of accepting worse solutions. In the case of vortex dynamics, we are effectively attempting to advect vorticity by a modified or effective streamfunction such that the area between two vorticity contours is preserved in addition to other constraints that may have been imposed. In the process of doing so, we extremize the energy or Hamiltonian of the system. For preliminaries related to this section,

on functionals, functional derivatives, Poisson brackets and symmetric brackets, we refer the reader to Morrison (1982), Morrison (1993), Vallis et al. (1989) and Flierl and Morrison (2011).

2.2.1 Original Hamiltonian dynamics (H)

The Hamiltonian dynamics can be generated from the Poisson bracket of functionals q (Potential vorticity) and H (Hamiltonian), and is given by

$$\frac{\partial}{\partial t} q = -\left[\psi, q\right], \tag{2.7}$$

$$q = \left(\nabla^2 - F\right)\psi + F\psi_2\left(y\right) = \left(\nabla^2 - F\right)\psi + T, \tag{2.8}$$

where we have omitted β for now due to issues with symmetry and periodicity. This is effectively the same evolution equation as we had discussed in the previous section with the unaltered streamfunction ψ given by

$$\psi\left(\mathbf{x}\right) = \int d\mathbf{x}'\, G\left(\mathbf{x} - \mathbf{x}'\right)\left(q\left(\mathbf{x}'\right) - T\left(\mathbf{x}'\right)\right). \tag{2.9}$$

The ψ_2 term behaves like β and does not contribute to the total upper layer energy E. Hence, the energy or the Hamiltonian is given by

$$H = E = \frac{1}{2}\int d\mathbf{x}\ |\nabla\psi|^2 + F|\psi|^2, \tag{2.10}$$

where the first term represents the kinetic energy and the second the available potential energy. Now we can show that the energy is conserved by integrating by parts as

follows

$$\begin{aligned}\frac{\partial}{\partial t}E &= \int \nabla\psi\cdot\nabla\psi_t + F\psi\psi_t \\ &= -\int \psi\left(\nabla^2 - F\right)\psi_t \\ &= -\int \psi q_t \\ &= \int \psi\left[\psi, q\right] \\ &= 0.\end{aligned} \tag{2.11}$$

Note that the energy E (or H) is not $-\frac{1}{2}\int \psi q$, but is in fact given by

$$H = -\frac{1}{2}\int \psi\left(q - T\right) = -\frac{1}{2}\int\int d\mathbf{x}\; d\mathbf{x}'\left(q\left(\mathbf{x}\right) - T\left(\mathbf{x}\right)\right)G\left(\mathbf{x}-\mathbf{x}'\right)\left(q\left(\mathbf{x}'\right) - T\left(\mathbf{x}'\right)\right). \tag{2.12}$$

Hence, we would need ψ_2 to depend on t to change the energy.

2.2.2 Simulated Annealing (SA)

SA dynamics can be generated by advecting the Potential vorticity with a modified streamfunction given by

$$\phi = a\int K\left(\mathbf{x}-\mathbf{x}'\right)\left[\psi, q\right]', \tag{2.13}$$

where $[\,]'$ indicates that it is a function of $\mathbf{x}'$ and K is the Green's function satisfying $\nabla^2 G\left(\mathbf{x}\right) = \delta\left(\mathbf{x}\right)$, which just leads to a smoothing. Now, the SA dynamics, effectively mimicking dissipation can be generated with a symmetric bracket of functionals q and H and is given by

$$\frac{\partial}{\partial t}q = -\left[\phi, q\right]. \tag{2.14}$$

Hence the rate of change of energy is now given by

$$\frac{\partial}{\partial t}E = \int \psi\left[\phi, q\right] = -\int \phi\left[\psi, q\right] = a\int\int K\left(\mathbf{x}-\mathbf{x}'\right)\left[\psi, q\right]'\left[\psi, q\right], \tag{2.15}$$

which is clearly sign definite. Further as $\frac{\partial}{\partial t}E \to 0$, we have $[\psi, q] \to 0$.

2.2.3 Hamiltonian Dirac (HD)

Let us define the Dirac bracket as

$$\left[A, B\right]_D = \left[A, B\right] + \frac{\left[A, c_1\right]\left[c_2, B\right] - \left[A, c_2\right]\left[c_1, B\right]}{\left[c_1, c_2\right]}, \tag{2.16}$$

where $c_1(\mathbf{x})$ and $c_2(\mathbf{x})$ are constraints applied according to the spatial symmetry in the flow. Then, we can show that

$$\left[c_1, B\right]_D = \left[c_2, B\right]_D = 0 \tag{2.17}$$

for any B. Now, the Hamiltonian Dirac dynamics can be generated using a Poisson bracket of q and H with an even number of constraints that are not Casimirs (the latter being functions of q which are automatically conserved) and is given by

$$\frac{\partial}{\partial t}q = -\left[\psi, q\right]_D = \left[q, \psi\right] + \frac{\left[q, c_1\right]\left[c_2, \psi\right] - \left[q, c_2\right]\left[c_1, \psi\right]}{\left[c_1, c_2\right]}. \tag{2.18}$$

Therefore, under HD dynamics

$$\frac{\partial}{\partial t}\int c_1 q = -\int c_1\left[\psi, q\right]_D = \int \psi\left[c_1, q\right]_D = 0, \tag{2.19}$$

assuming there are no boundary condition issues while integrating by parts. Indeed, q not going to zero is a concern for all integrations by parts. However, this issue can be sorted out by selecting suitably periodic functions.

2.2.4 Hamiltonian Dirac Simulated Annealing (HDSA)

The HDSA dynamics is a combination of HD and SA dynamics and is given by

$$\frac{\partial}{\partial t}q = -\left[\phi, q\right]_D ; \qquad \phi = a\int K\left(\mathbf{x}-\mathbf{x}'\right)\left[\psi, q\right]'_D . \tag{2.20}$$

The key here is to use $[\,]'_D$ in both the dynamics and the definition of ϕ, ensuring that E will grow or decay consistently.

To summarize, we have the following types of dynamics:

$$H: \qquad \frac{\partial}{\partial t}q = \left[q, \psi\right], \tag{2.21}$$

$$HD: \qquad \frac{\partial}{\partial t}q = \left[q, \psi\right]_D , \tag{2.22}$$

$$SA: \qquad \frac{\partial}{\partial t}q = \sigma\left[q, \psi\right] + \alpha\left[q, \phi\right], \qquad \phi = a\int K\left(\mathbf{x}-\mathbf{x}'\right)\left[\psi, q\right]', \tag{2.23}$$

$$HDSA: \qquad \frac{\partial}{\partial t}q = \sigma\left[q, \psi\right]_D + \alpha\left[q, \phi\right]_D , \qquad \phi = a\int K\left(\mathbf{x}-\mathbf{x}'\right)\left[\psi, q\right]'_D \tag{2.24}$$

where we have assigned weights σ and α for ideal and dissipative dynamics respectively.

2.3 Spatial and temporal discretization

For our simulations, we have worked with an in-house pseudo-spectral solver which has been passed down through generations of researchers. Of course, we have modified this by incorporating the simulated annealing dynamics, which can be tricky to code. The numerical scheme essentially consists of a doubly periodic spatial domain with Fourier basis (Discrete Fourier transform), and an explicit second order Adams-Bashforth time marching (by updating either q or $\dot{q}$) algorithm. The term 'pseudo-spectral' is derived from the fact that we return to the physical space to compute the non-linear terms. In the process of computing these advection terms, we need to ensure that the contribution from higher wavenumbers does not alias onto that from the lower

wavenumbers. In order to achieve this, we truncate the wavenumbers higher than the Nyquist wavenumbers. This method has been found to perform very well and rivals the more complicated modern de-aliasing techniques. Further, we stabilize the code by filtering out the small scales using an exponential wavenumber cut-off filter (Canuto et al., 2006). As mentioned earlier, implementing the simulated annealing dynamics poses a potential banana skin and is not to be underestimated. For the benefit of the reader, we have attached the simulated annealing portion of the code in Appendix A with sufficient explanation of each line in the comments.

Chapter 3

Results and discussion

3.1 Problem setup

The initial condition here consists of a vortex embedded in a background sinusoidal shear flow. We have chosen a sinusoidal shear because of the simplicity in applying the numerical technique, where we have used a doubly periodic domain with Fourier basis. The actual zonal velocities on Jupiter are much more sharper and asymmetric than a smooth symmetric sinusoidal background. However, our idea is to primarily capture the physics with a toy model that is not too far off the actual observations. The initial condition is given by

$$q_{1i} = \left(\nabla^2 - F\right)\psi_{1i} + F\psi_{2i}, \tag{3.1}$$

$$q_{2i} = \nabla^2\psi_{2i}, \tag{3.2}$$

$$\psi_{1i} = \psi_{1vi} + \psi_{1bi}, \tag{3.3}$$

$$\psi_{2i} = \psi_{2bi}, \tag{3.4}$$

$$q_{1pi} = \left(\nabla^2 - F\right)\psi_{1vi} = A \times \exp\left\{-\left(\frac{r}{a}\right)^4\right\}, \tag{3.5}$$

$$\nabla^2\psi_{1bi} = \nabla^2\psi_{2bi} = \cos\left(y + y_o\right). \tag{3.6}$$

where the upper layer streamfunction has been split into a vortex (ψ_{1vi}) and a background flow (ψ_{1bi}) contribution, the infinitely deep lower layer streamfunction contains only the background flow streamfunction ψ_{2bi}, the potential vorticity of the vortex is q_{1pi} which is close to the observed roughly uniform potential vorticity profiles on Jupiter, a is the size or radius of the vortex and y_o is the position of the vortex. Remember that we actually center the vortex and shift the background shear in our simulations. This is especially helpful for the HDSA simulations where we have periodic constraints. The range of the domain is given by $-\pi < x < \pi$ and $-\pi < y < \pi$ for a $2\pi \times 2\pi$ domain, and $-2\pi < x < 2\pi$ and $-2\pi < y < 2\pi$ for a $4\pi \times 4\pi$ domain. We have used either 256^2 or 512^2 grid points, the latter in most cases. We have chosen our length scale as $L = 1$. Our vorticity scale is the maximum vorticity of the background flow, which we have chosen as $q_o = 1$.

3.2 Original Hamiltonian dynamics

First, we run preliminary simulations in the original Hamiltonian dynamics framework to get a rough idea of the range of values for the various parameters that we need to search for vortex steady states. In addition to this, we will also see firsthand the drawbacks of using simple H dynamics.

To begin with, we try to understand the effect of varying the magnitude of potential vorticity of the vortex A from 1 to 50, keeping the other parameters constant. Also, we prefer to stay on the f-plane and keep $A > 0$ for now. When the sign of background flow vorticity and that of the vortex match, we consider the vortex to be in a prograde shear region. If the signs don't match, then the vortex is in an adverse shear region. We have chosen $a = \pi/6$, $R_d/a = 0.25$, $y_o = 0$, and $\beta = 0$ for these simulations. In Fig. 3-1, we observe that the vortex elongates continuously due to the background shear. At this radius of deformation $R_d/a = 0.25$ and latitude $y_o = 0$ (where the shear is symmetric and same signed North or South of the center of vorticity), $A = 1$ is simply too small for the vortex to hold its structure. The elongation

goes on until the vortex is thin enough for Kelvin Helmholtz (KH) instability to take over and roll up into tiny vortices (although we haven't run the simulation for long enough to observe the tiny vortices). Of course, since we filter small scales, the enstrophy is no longer maintained at longer times. If we a-priori decide that the maximum elongation is limited to the size of the domain and that the final area of the vortex is roughly the same as the initial area for us to consider the final vortex state to be a steady state, we can clearly see that this is not a steady state. In the next run of $A = 5$ in Fig. 3-2, we can observe a similar phenomenon of elongation, although not as long as the previous case. Here the vortex goes unstable to KH instability much faster and we are able to clearly see the elongated vortex roll up into smaller vortices, the sizes of which depend of the wavenumber (wavelength) of the instability. Once this happens, the code filters the scales beyond the cutoff wavenumber and hence there is a drop in enstrophy (filamentation). However, we can observe merger of the tiny vortices back into larger vortices, in agreement with QG turbulence. At $A = 20$ (Fig. 3-3), the vortex elongates much lesser than before, precesses in the counter clockwise direction such that it aligns itself with the background flow. However, the vortex is unstable since its aspect ratio is very large and R_d is small. It splits into three vortices, two larger ones of the same size and a central smaller vortex. Due to asymmetries and a bit of wobbling, the background shear brings the larger vortices closer to the smaller one and they appear to merge. Of course, we once again observe filamentation and loss of enstrophy due to the scale selective filtering. However, we are much closer to the steady state than before. Next, at $A = 50$ (Fig. 3-5), the vortex is strong enough to maintain its structure and area approximately. Here its aspect ratio increases initially (becomes elliptical) and it then precesses in the counter clockwise direction to try and align itself with the background flow. Some filamentation is observed during the precession and some vorticity is lost to the filaments. However, the elliptic vortex overshoots the axis. Once that happens, the vortex goes back to a roughly circular shape due the the symmetric shear at $y_o = 0$. It then once again elongates to form an ellipse and the cycle repeats. Hence this is some kind of

oscillatory state that the vortex attains. We have also performed simulations for a vortex double the size of the one described above, i.e $a = \pi/3$, and find very similar behavior at this $R_d/a = 0.25$ (Fig. 3-9,3-10 and 3-11). What this means is that the vortex is still too small to feel the effects of curvature in the flow.

Next, we increase the R_d/a to 1 and once again look at the effect of increasing A. It is clear from Figs. 3-6,3-7 and 3-8, that a R_d which is equal to or of the order of the radius of the vortex, is able to hold its structure better than the $R_d/a = 0.25$ case due to the fact that the vorticity dominates for $a < R_d$. Although we do observe the elongation and rolling up into vortices for the $A = 1$ case, the moderate values of $A = 5$ and $A = 20$ do give rise to elliptical steady states. However, we do observe a some vorticity being lost as filaments in the $A = 5$ case. Further, it appears that the vortex in fact alters the background slightly. In the $A = 20$ case, the vortex dominates and although it appears to have settled into an elliptical steady state, it has dramatically altered the background flow especially locally. Further, it is clear that as we increase the radius of deformation, the aspect ratio of the ellipse, if formed, decreases.

Going back to $R_d/a = 0.25$, we now place the vortex at $y_o = \pi/2$ where the shear is asymmetric about the center of vorticity in the meridional direction and has opposite signed shear North and South of the center of vorticity. In other words, half the vortex is in prograde shear and the other half in adverse shear to begin with along with the fact that the vortex resides in a region where the flow has maximum positive curvature. Of course, here the velocity is non-zero and the vortex is advected with the flow. It is difficult to point out for now if the vortex is stationary in the flow frame of reference. We now vary A and the results are shown in Figs. 3-12,3-13,3-14,3-15. For $A = 1$, the vortex initially evolves into an $m = 3$ vortex due to the fact that shear is opposite signed on the North and South sides of the center of vorticity. The vortex is hence like an arrow pointing towards the direction in which it moves. The vortex then begins to precess in the counter clockwise direction along with the formation of tines which carry away the vorticity from the vortex through a stagnation point on the

north side. as filaments. The vortex rotates till one of its sides (assuming the $m = 3$ is roughly a triangle) is aligned with the flow. The magnitude of vorticity here is on the lower end and the adverse region of shear pushes the vortex South. Finally, most of the vorticity ends up in the prograde shear region. As A increases, the extent to which the vortex moves South into the prograde region decreases. Further, the $m = 3$ becomes clearer and the filaments reduce. Hence less vorticity is lost in the filaments, and enstrophy does not drop as much.If the final vortex is exactly at $y_o = \pi/2$, then the shape should be a near perfect $m = 3$. However, as the vortex is pushed further into the prograde shear region, the shape becomes a mix of $m = 2$ and $m = 3$ modes.

Next, staying at $y_o = \pi/2$, we look at the case where $R_d/a = 1$ in Figs. 3-16, 3-17, 3-18 and 3-19. For small A, the vortex loses a lot of vorticity through tines and filaments but shows similar behavior to the smaller R_d case where the vortex was pushed or expelled from the adverse region into the prograde region. Further, the background is altered much more than the previous case when $R_d/a = 0.25$. When R_d is large or the same order as the size of the vortex, the vortex has a much greater influence on the background and alters it to such an extent that the local background flow is no longer zonal, especially for the moderate and high A cases. The higher the A, the more the vortex wraps the background vorticity around itself. By wrapping the vorticity around itself, the vortex can now translate South (conservation of y center of vorticity or linear momentum in the x direction. However, beyond a particular magnitude, the vortex translates less since it is much more dominant than the background shear. Further, higher the A, the more circular the vortex becomes.

Now, we consider simulations in which the vortex is placed at $y_o = \pi$ or in a region of maximum adverse shear (Figs. 3-20, 3-21, 3-22 and 3-23. In this region the shear is symmetric and single signed about the center of vorticity in the North South direction. Although the values of A seem unphysical, it is still interesting to observe the effect of adverse shear. For $A = 50$, the vortex just elongates due to the shear at an angle to the flow and goes KH unstable when it reaches a critical aspect ratio. Of course, a lot of vorticity is lost in filaments (enstrophy goes down). The resulting vortices then

form elliptical steady states which are aligned perpendicular to the background flow direction. As A increases from 50 to 100 and then 200, the number of vortices formed after elongation decreases to 4 and 2 respectively. For $A = 400$, we obtain a stable steady state where the elliptical vortex is aligned perpendicular to the background flow direction. The resulting vortex is seen to show some oscillations about its major axis.

Finally, we look at the non-zero β case (Figs. 3-24, 3-25, 3-26 and 3-27). Here, we first vary the meridional position of the vortex and fix the rest of the parameters at $A = 2$, $a = \pi/6$, $R_d/a = 1$, $\beta = 1$. We tried $y_o = \pi/2$, $y_o = 0$ and $y_o = -\pi/2$. At $y_o = \pi/2$, the total background vorticity gradient becomes 0 (changes sign). Hence the vortex gets stuck at this latitude, at the same time undergoing a change of shape to the $m = 3$ vortex. We can also clearly see the tine that carries away the vorticity from the vortex. Therefore, it is more like a quasi-steady state until enough vorticity has been lost. At $y_o = 0$, the background PV gradient is now equal to 1. Hence this gives the vortex the opportunity to drift Northwest. Since Rd is on the higher side, there is a bit of dispersion and loss of vorticity through filaments. For the $y_o = -\pi/2$, we have the background PV gradient equal to 2. Hence the Northward drift and the dispersion is higher than in the $y_o = 0$ case. Further, the background is altered by a greater extent than the $y_o = 0$ case. For $\beta = 10$, we get lots of dispersion, and both the vortex and the background completely lose their character.

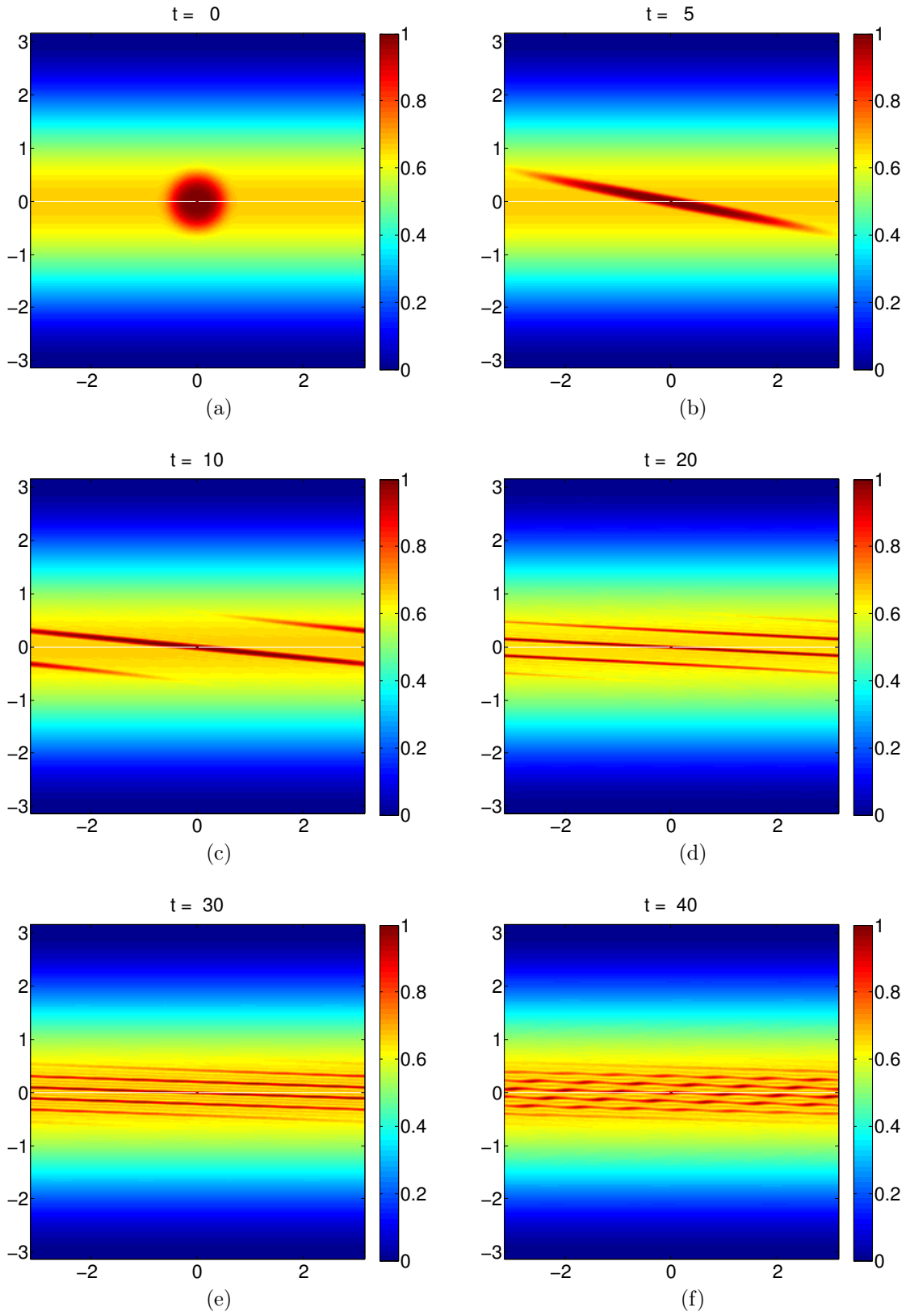

Figure 3-1: $A = 1$, $a = \pi/6$, $R_d/a = 0.25$, $y_o = 0$, $\beta = 0$.

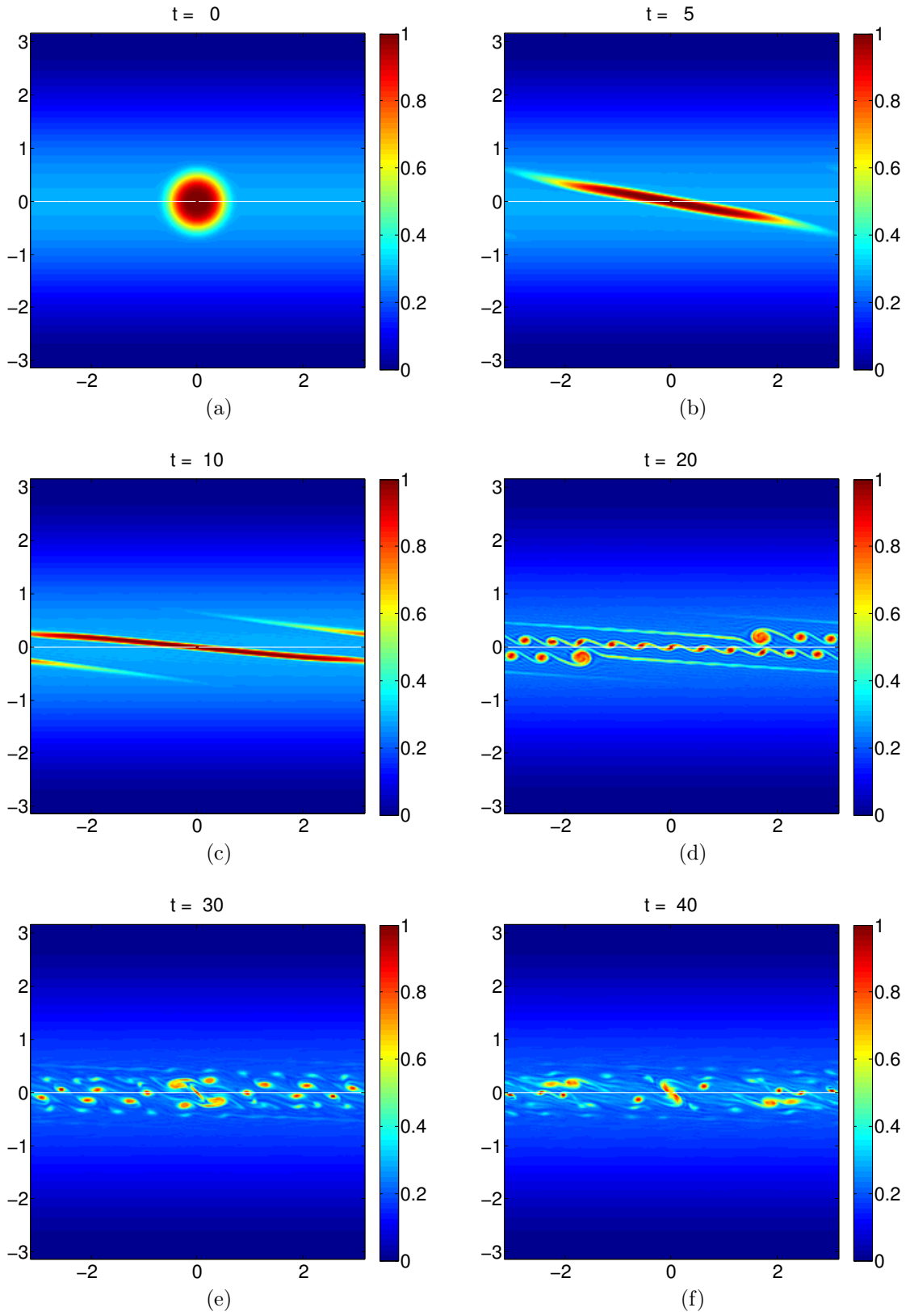

Figure 3-2: $A = 5$, $a = \pi/6$, $R_d/a = 0.25$, $y_o = 0$, $\beta = 0$.

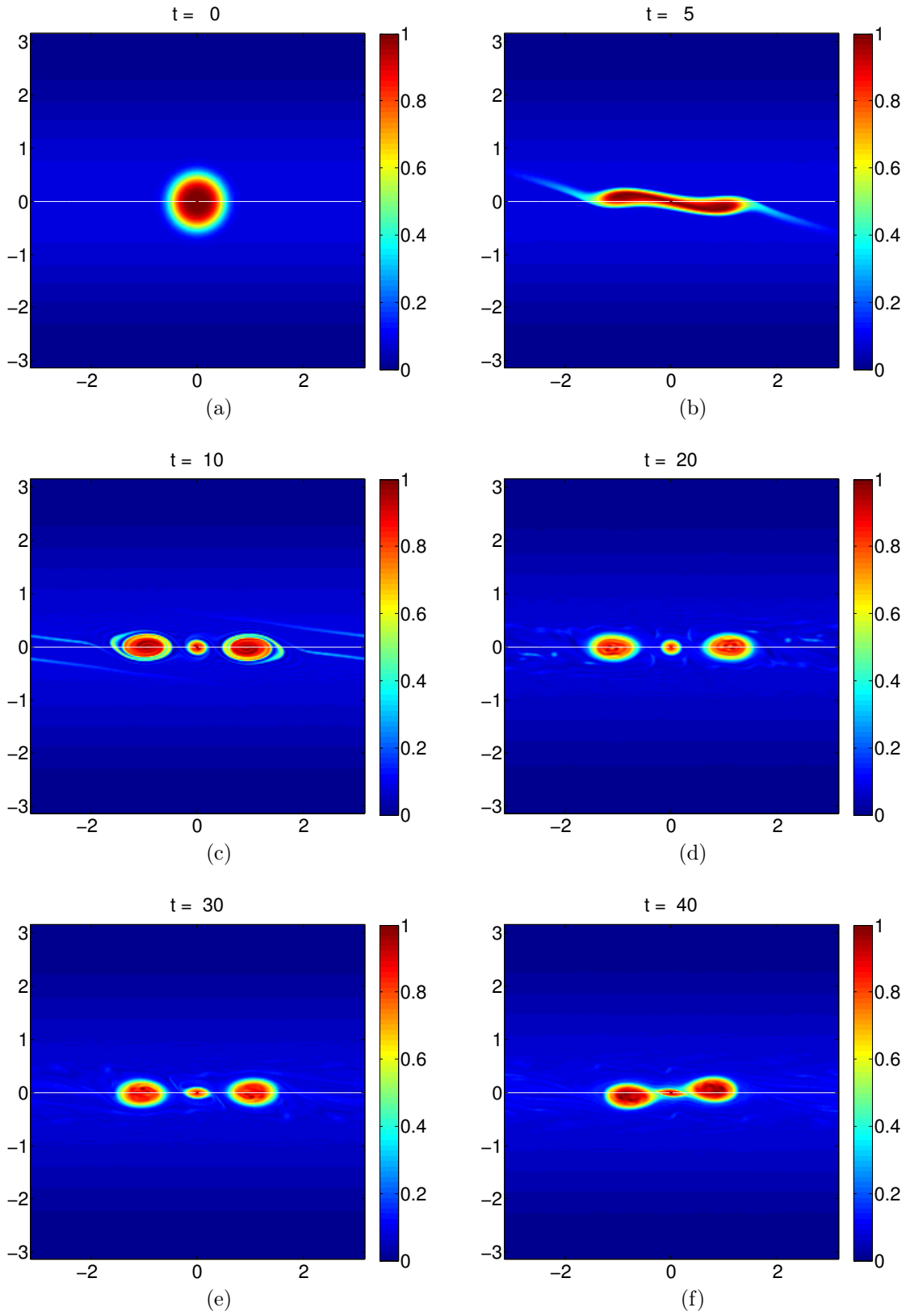

Figure 3-3: $A = 20$, $a = \pi/6$, $R_d/a = 0.25$, $y_o = 0$, $\beta = 0$.

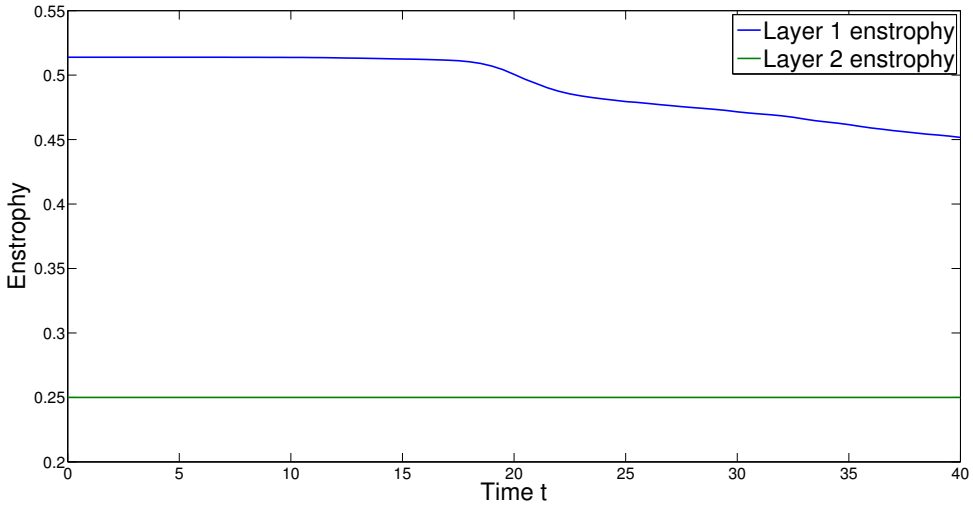

(a) $A = 5$

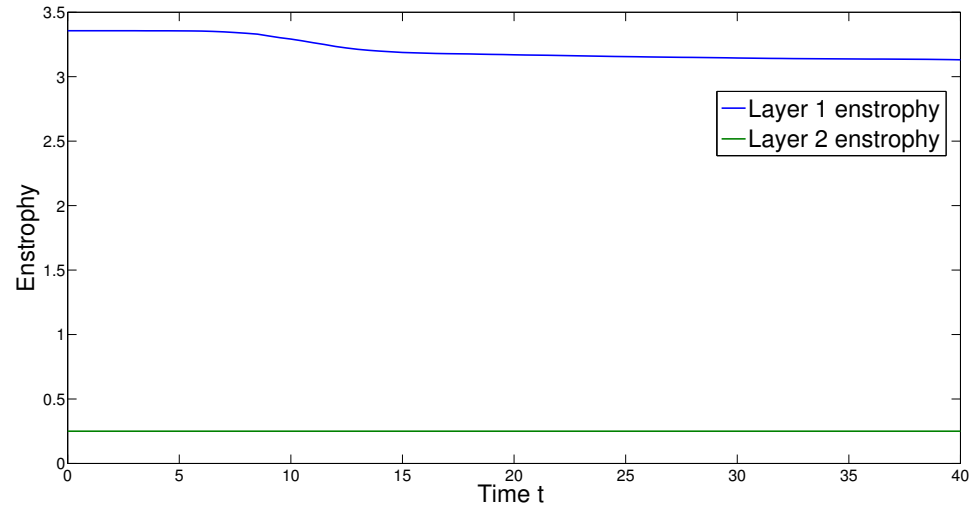

(b) $A = 20$

Figure 3-4: $a = \pi/6$, $R_d/a = 0.25$, $y_o = 0$, $\beta = 0$. Enstrophy loss.

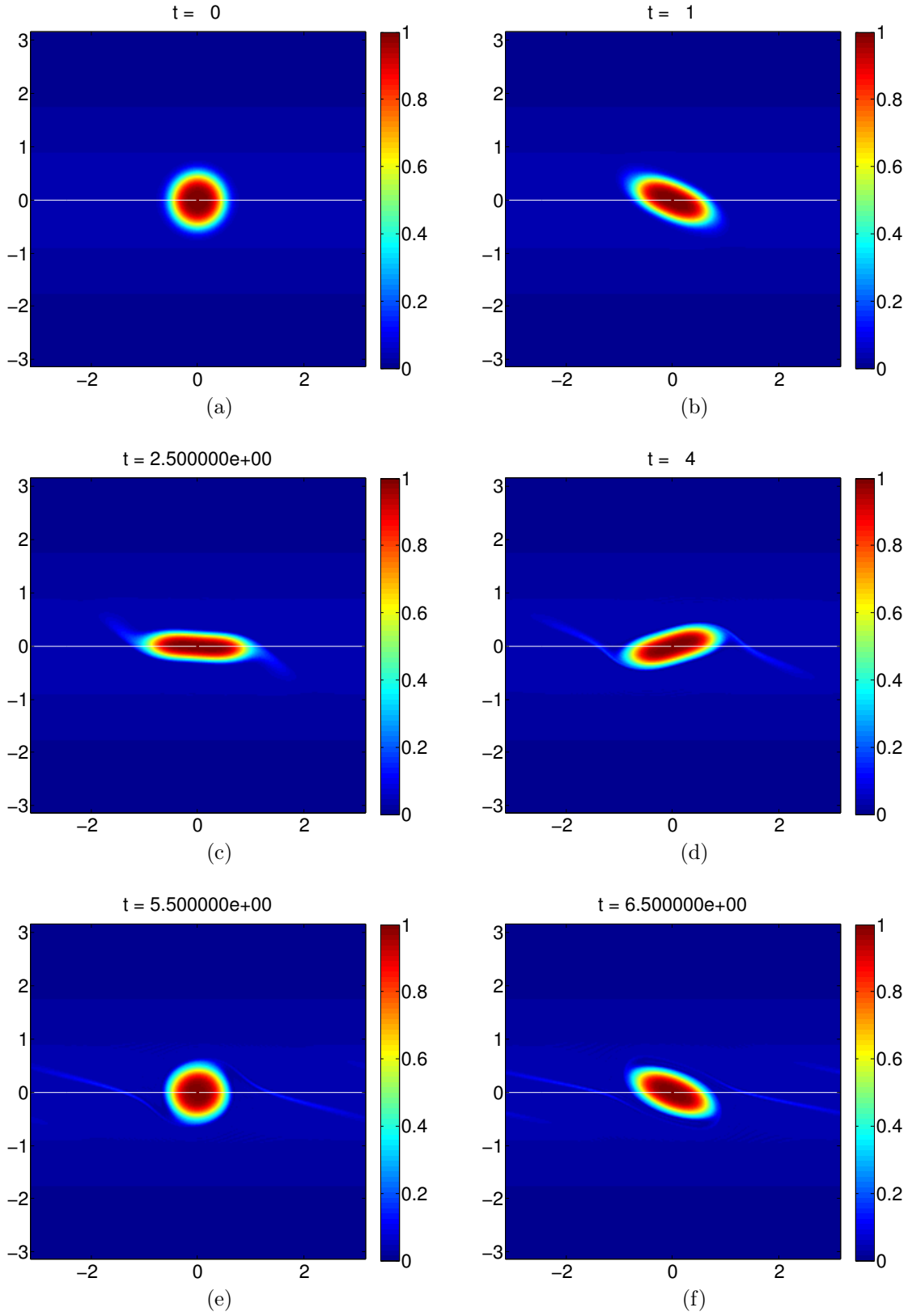

Figure 3-5: $A = 50$, $a = \pi/6$, $R_d/a = 0.25$, $y_o = 0$, $\beta = 0$.

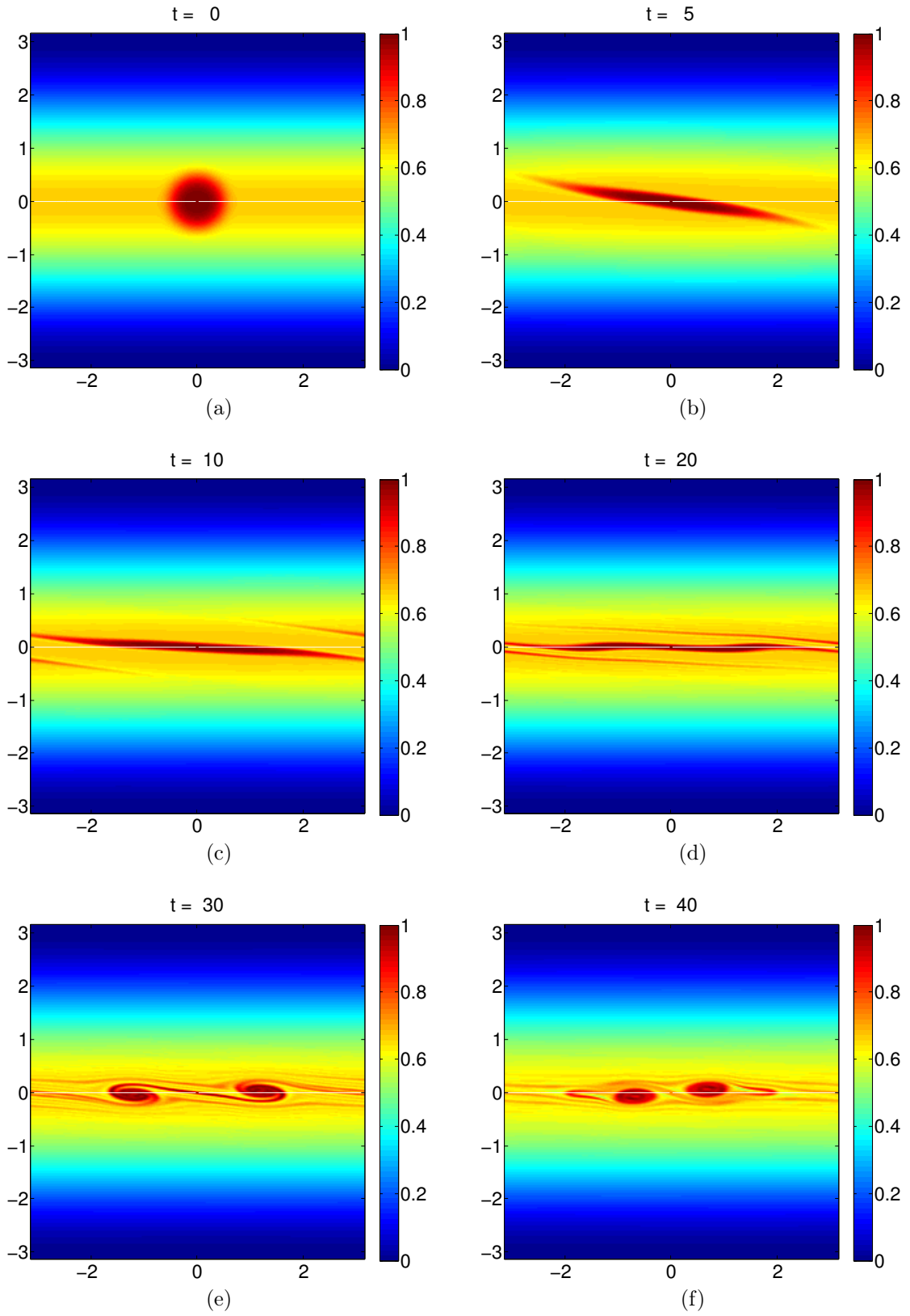

Figure 3-6: $A = 1$, $a = \pi/6$, $R_d/a = 1$, $y_o = 0$, $\beta = 0$.

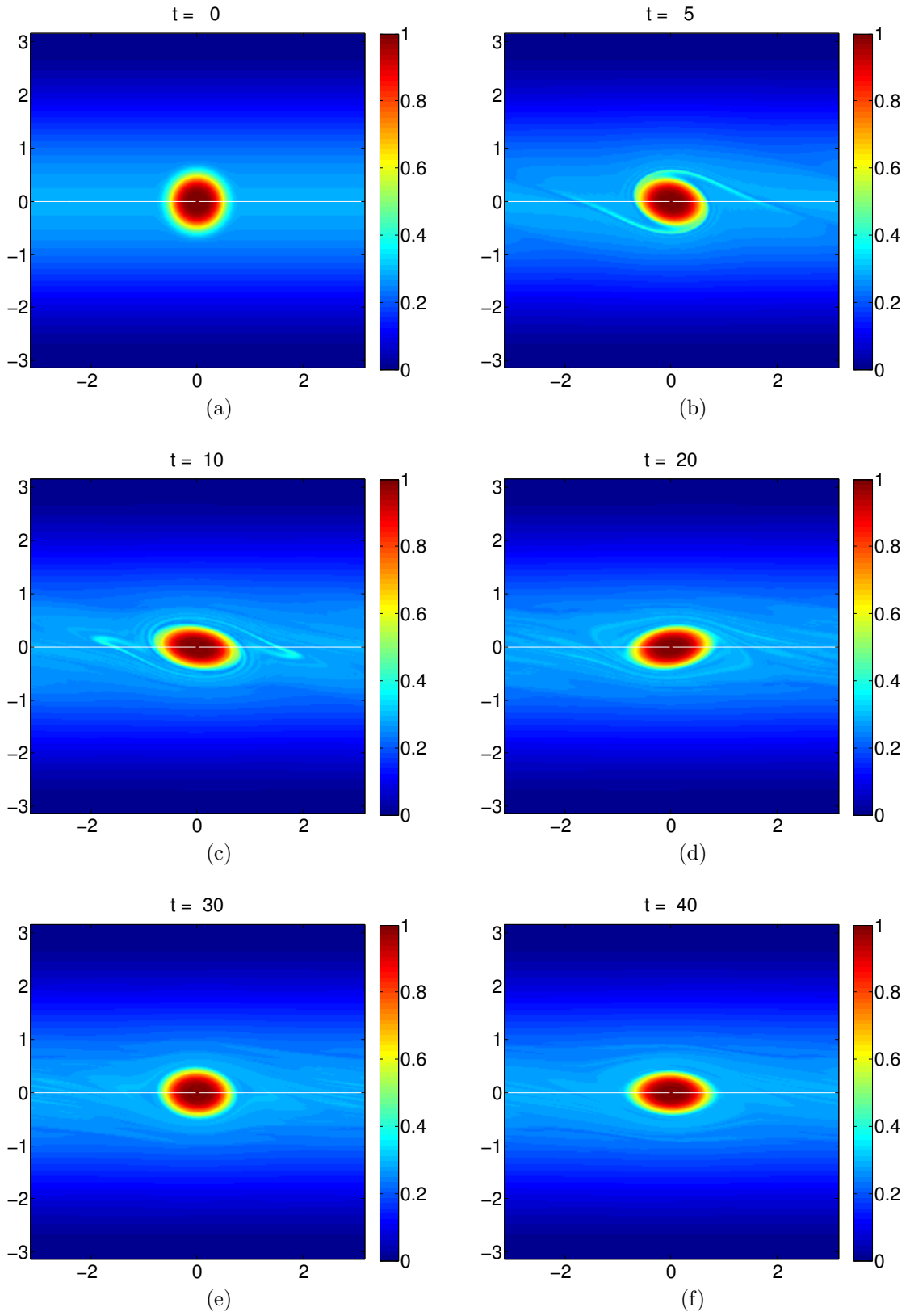

Figure 3-7: $A = 5$, $a = \pi/6$, $R_d/a = 1$, $y_o = 0$, $\beta = 0$.

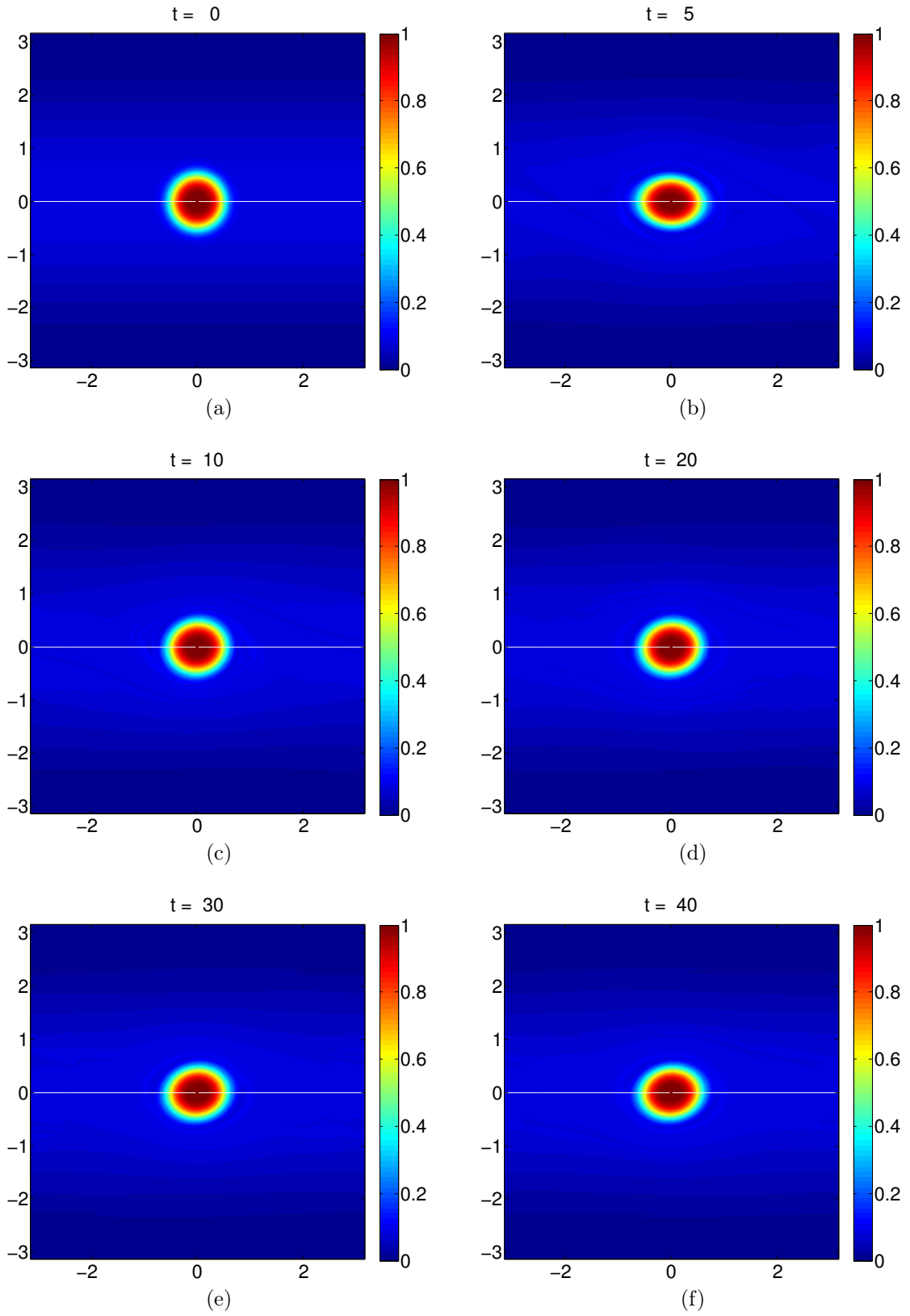

(a) (b) (c) (d) (e) (f)

Figure 3-8: $A = 20$, $a = \pi/6$, $R_d/a = 1$, $y_o = 0$, $\beta = 0$.

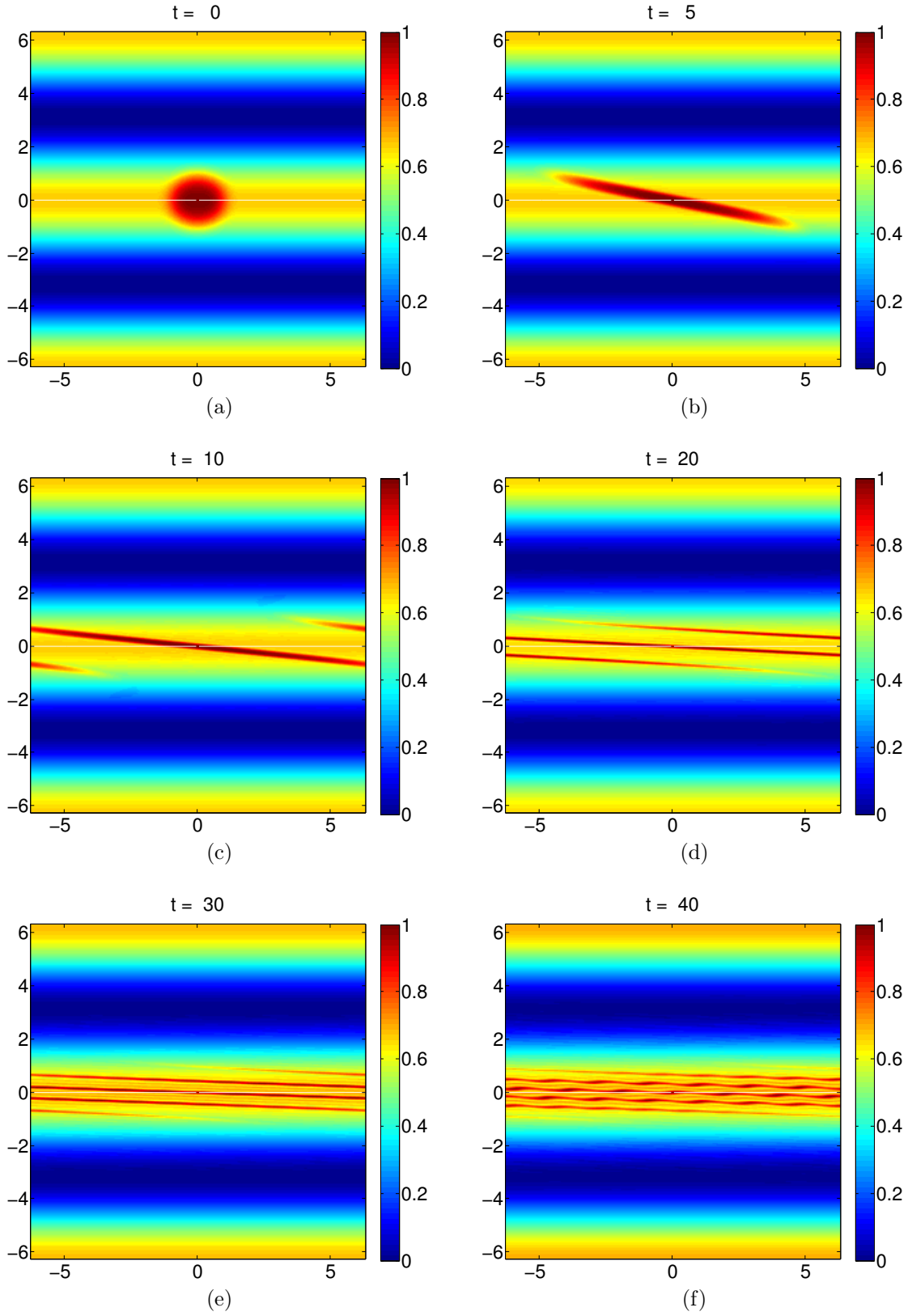

Figure 3-9: $A = 1$, $a = \pi/3$, $R_d/a = 0.25$, $y_o = 0$, $\beta = 0$.

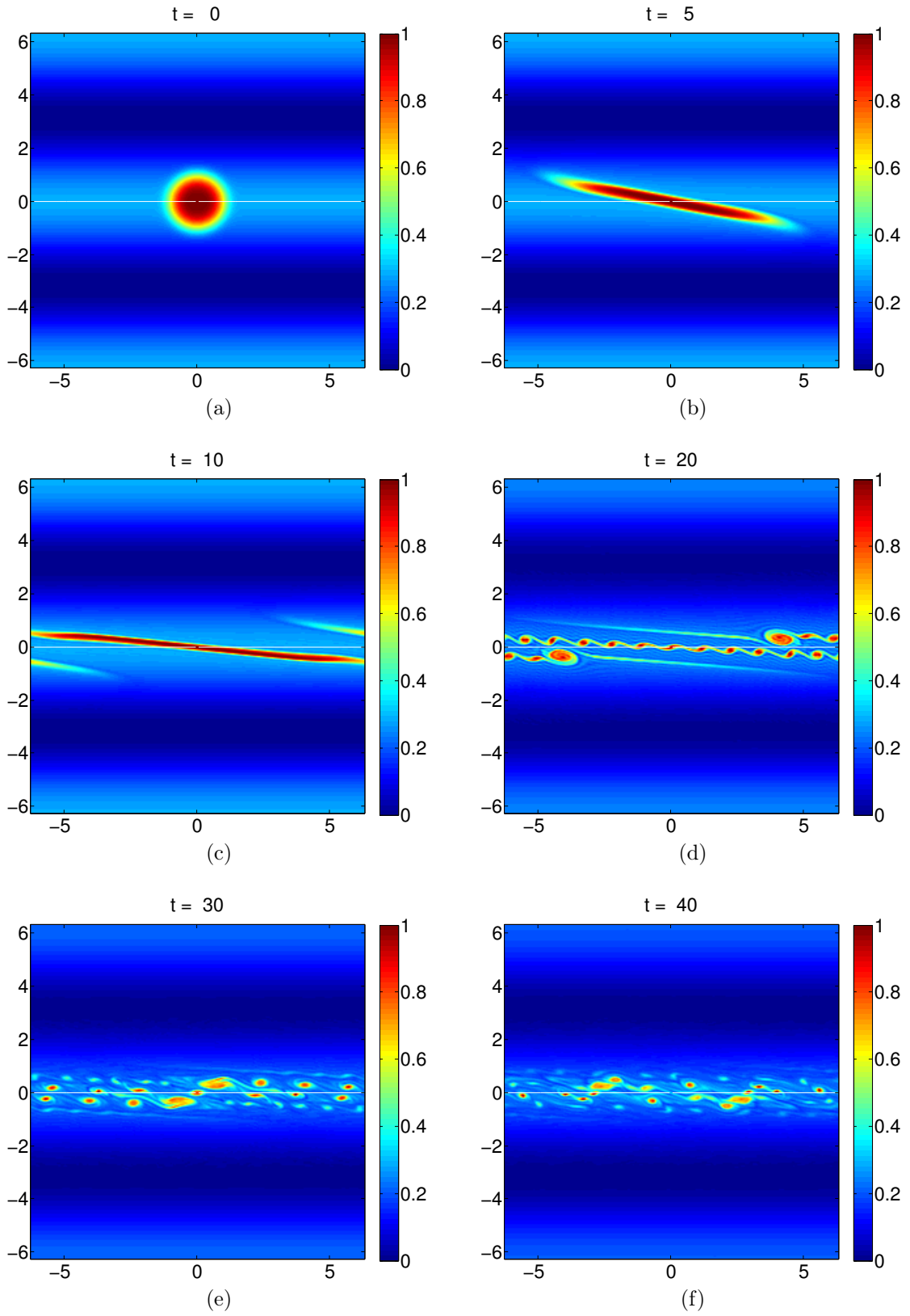

Figure 3-10: $A = 5$, $a = \pi/3$, $R_d/a = 0.25$, $y_o = 0$, $\beta = 0$.

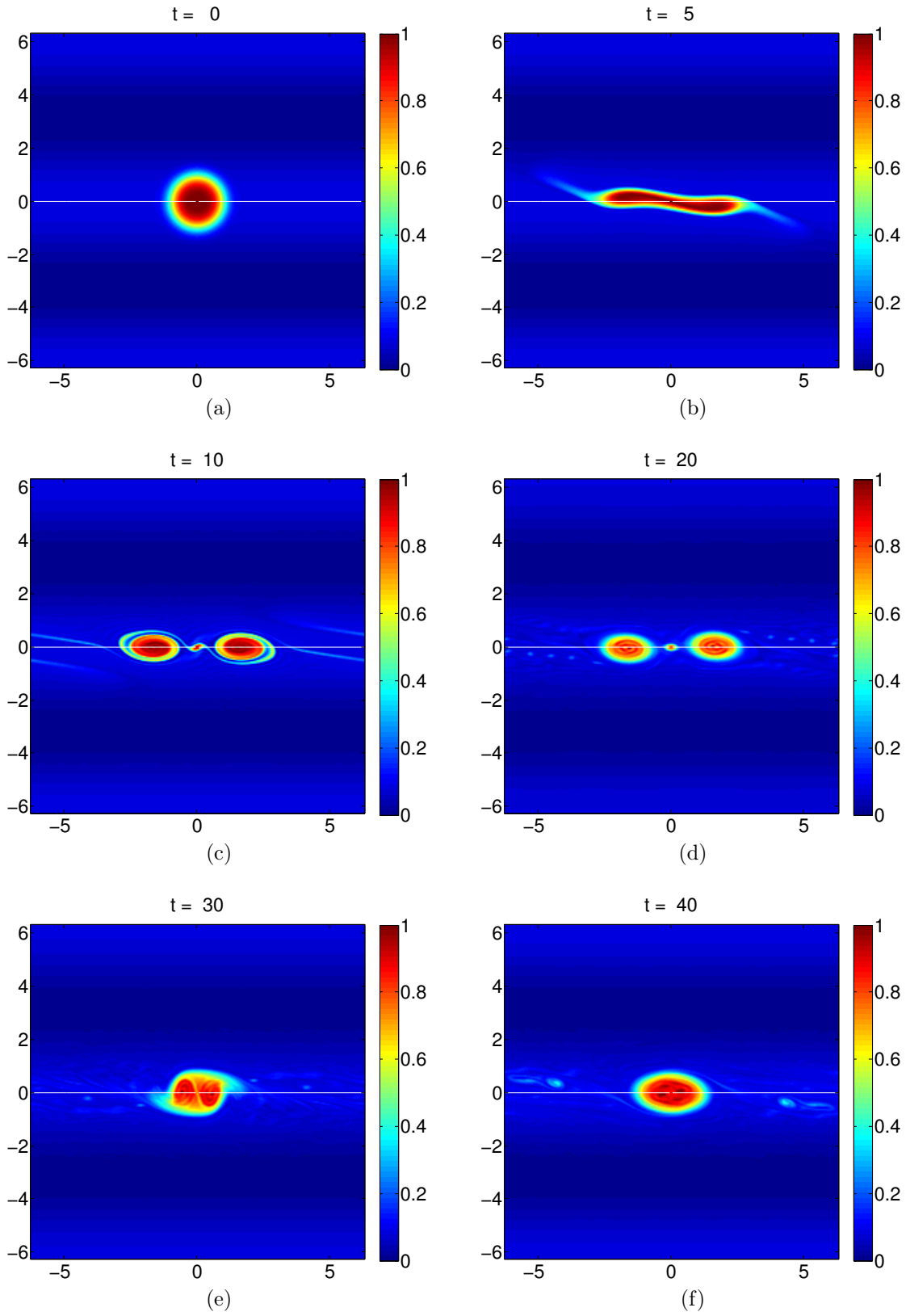

Figure 3-11: $A = 20$, $a = \pi/3$, $R_d/a = 0.25$, $y_o = 0$, $\beta = 0$.

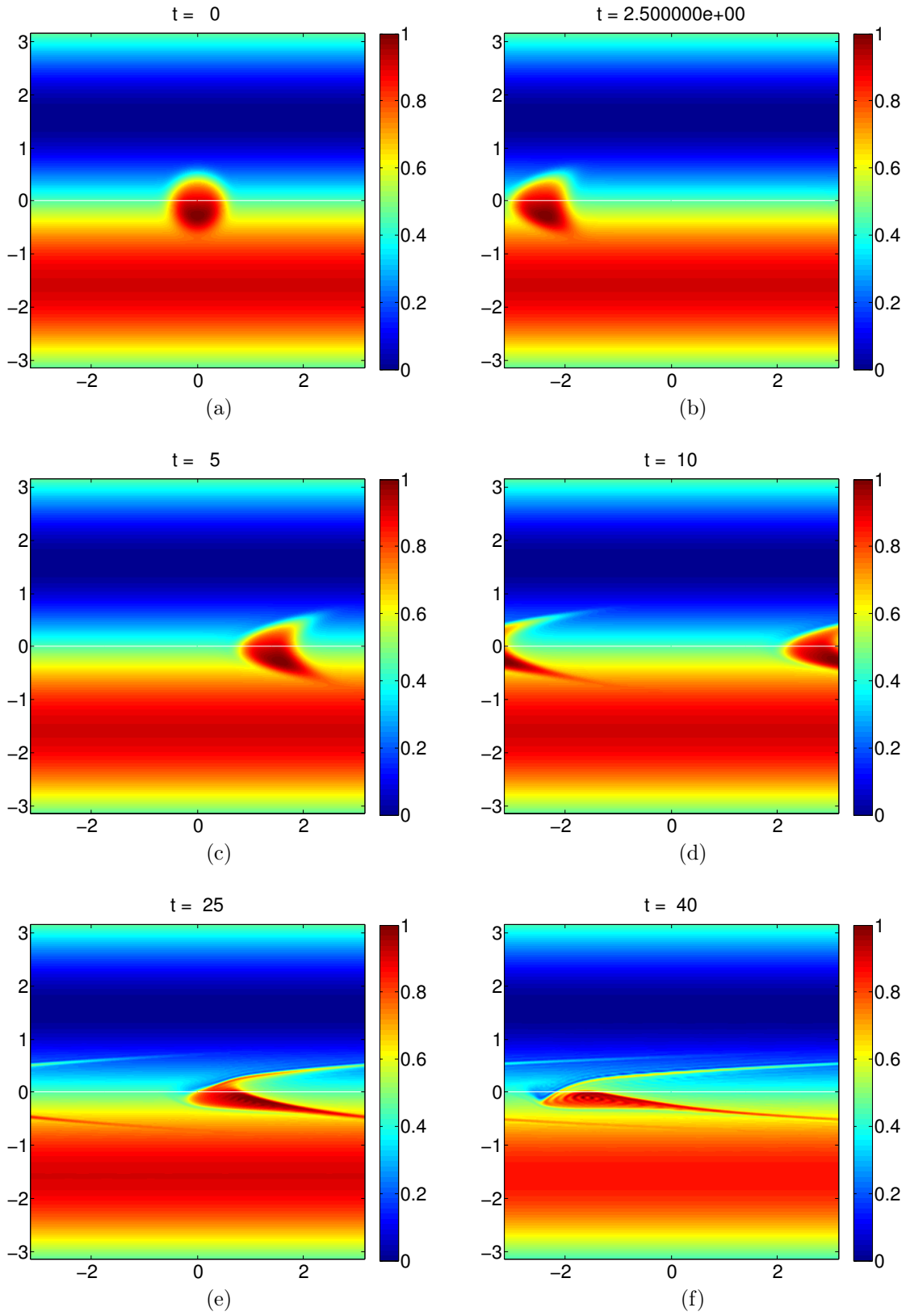

Figure 3-12: $A = 1$, $a = \pi/6$, $R_d/a = 0.25$, $y_o = \pi/2$, $\beta = 0$.

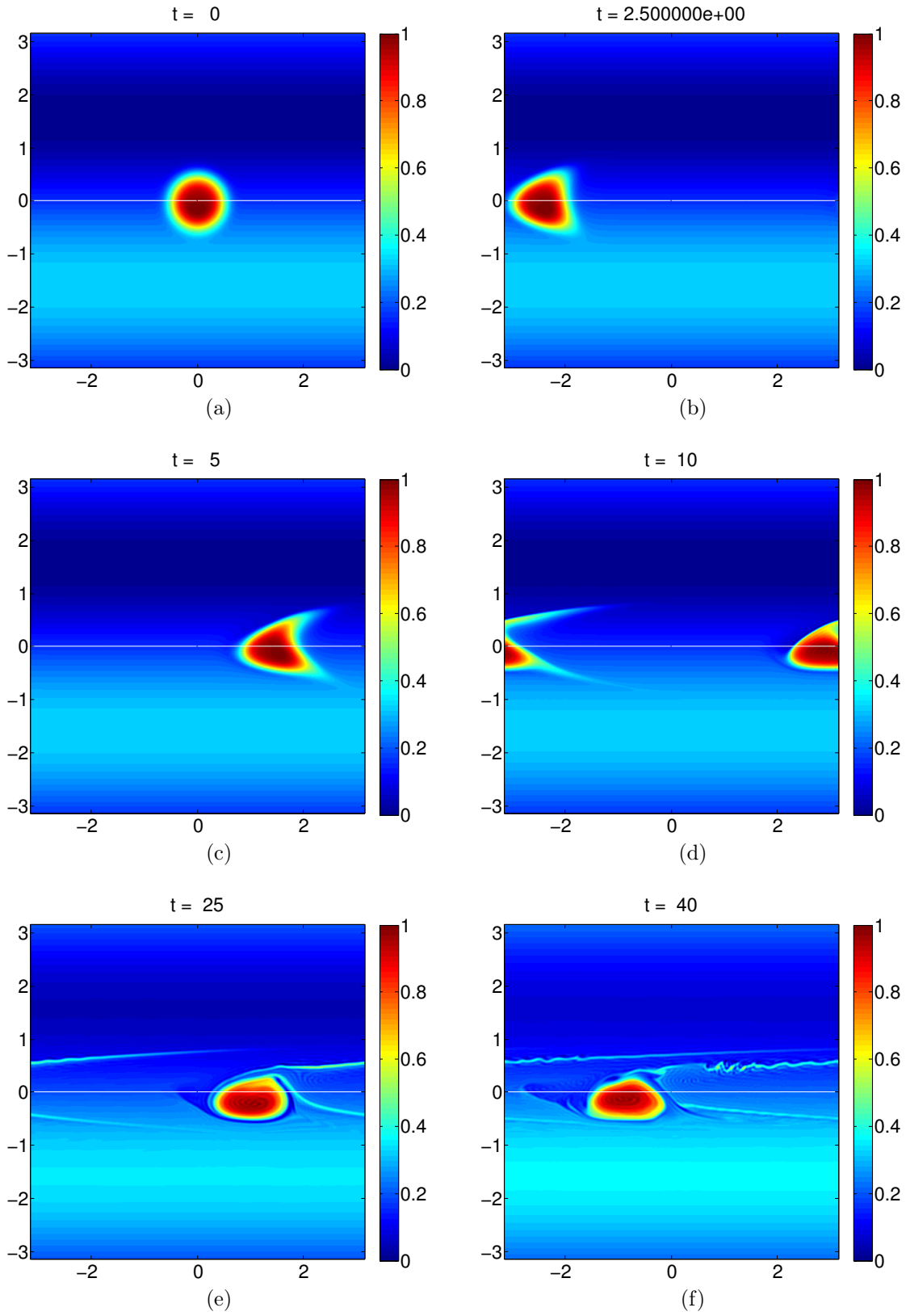

Figure 3-13: $A = 5$, $a = \pi/6$, $R_d/a = 0.25$, $y_o = \pi/2$, $\beta = 0$.

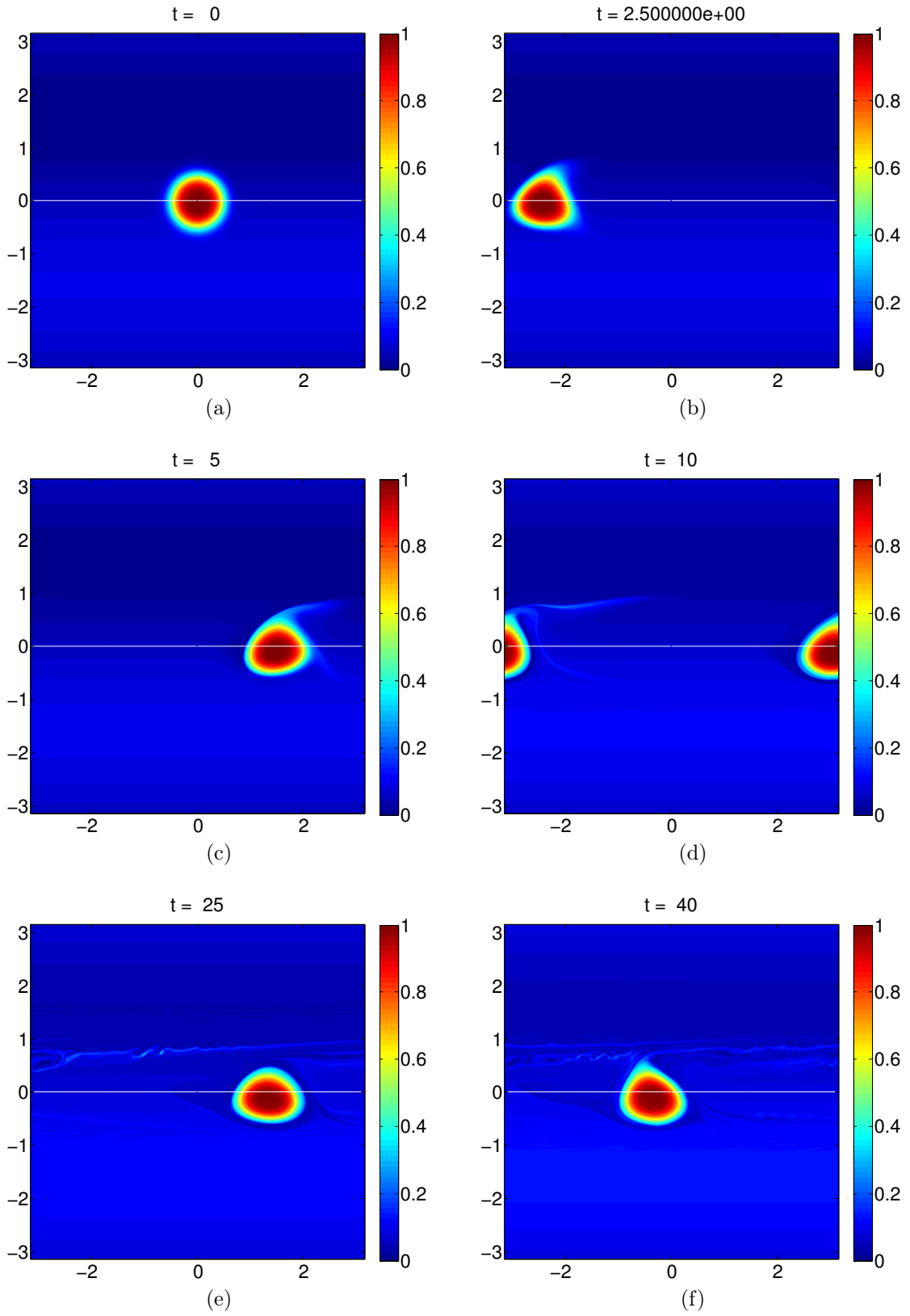

Figure 3-14: $A = 20$, $a = \pi/6$, $R_d/a = 0.25$, $y_o = \pi/2$, $\beta = 0$.

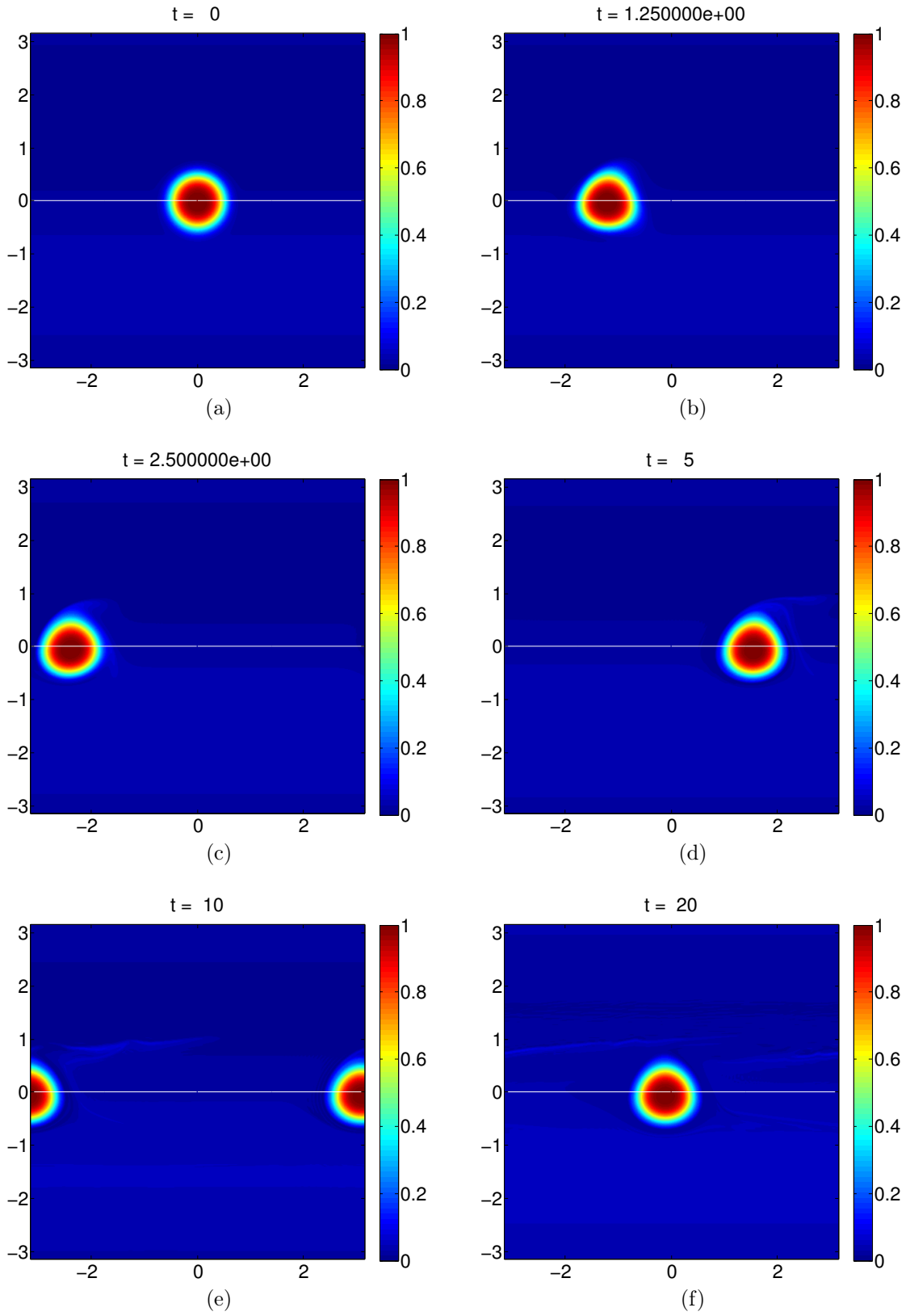

Figure 3-15: $A = 50$, $a = \pi/6$, $R_d/a = 0.25$, $y_o = \pi/2$, $\beta = 0$.

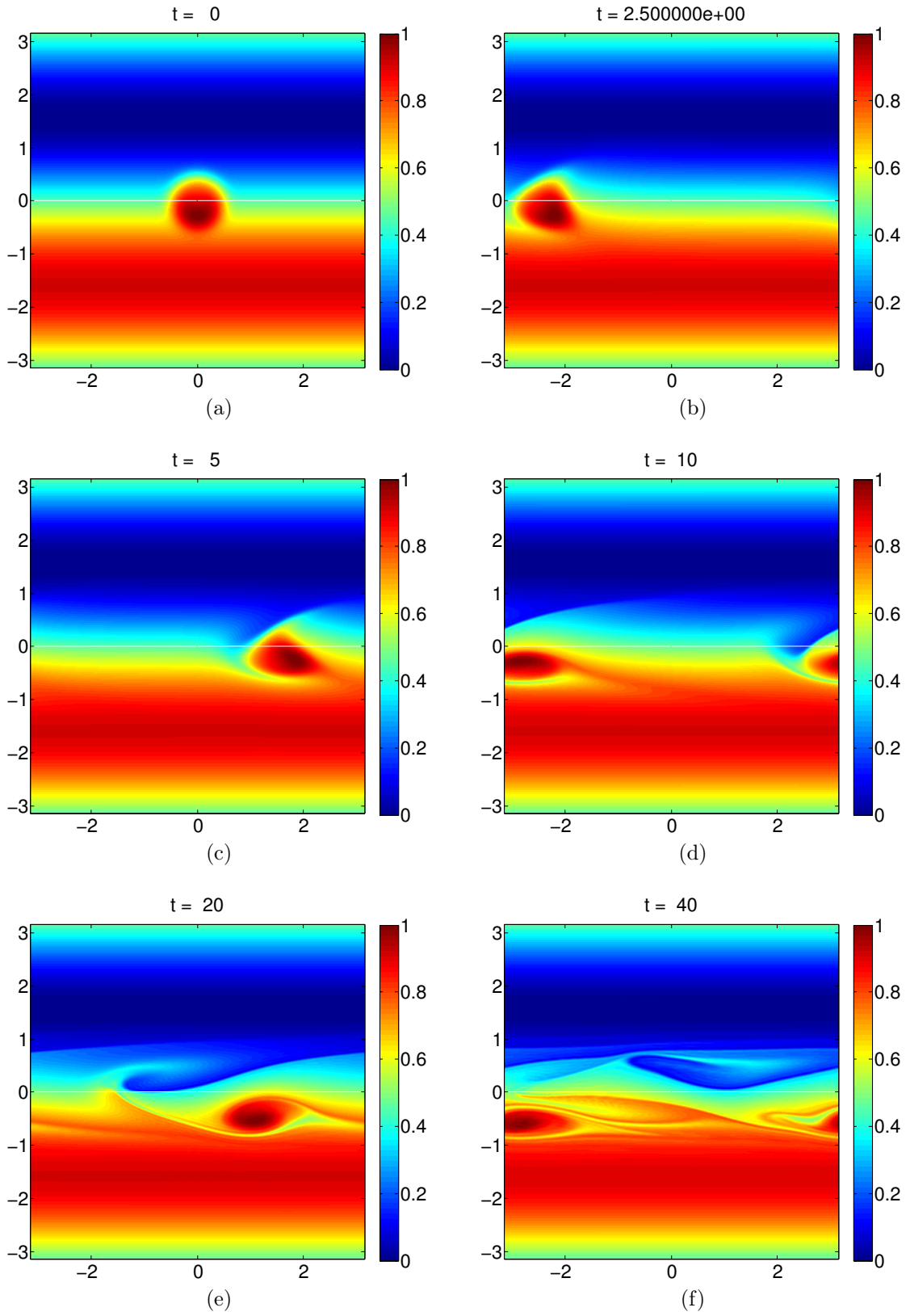

Figure 3-16: $A = 1$, $a = \pi/6$, $R_d/a = 1$, $y_o = \pi/2$, $\beta = 0$.

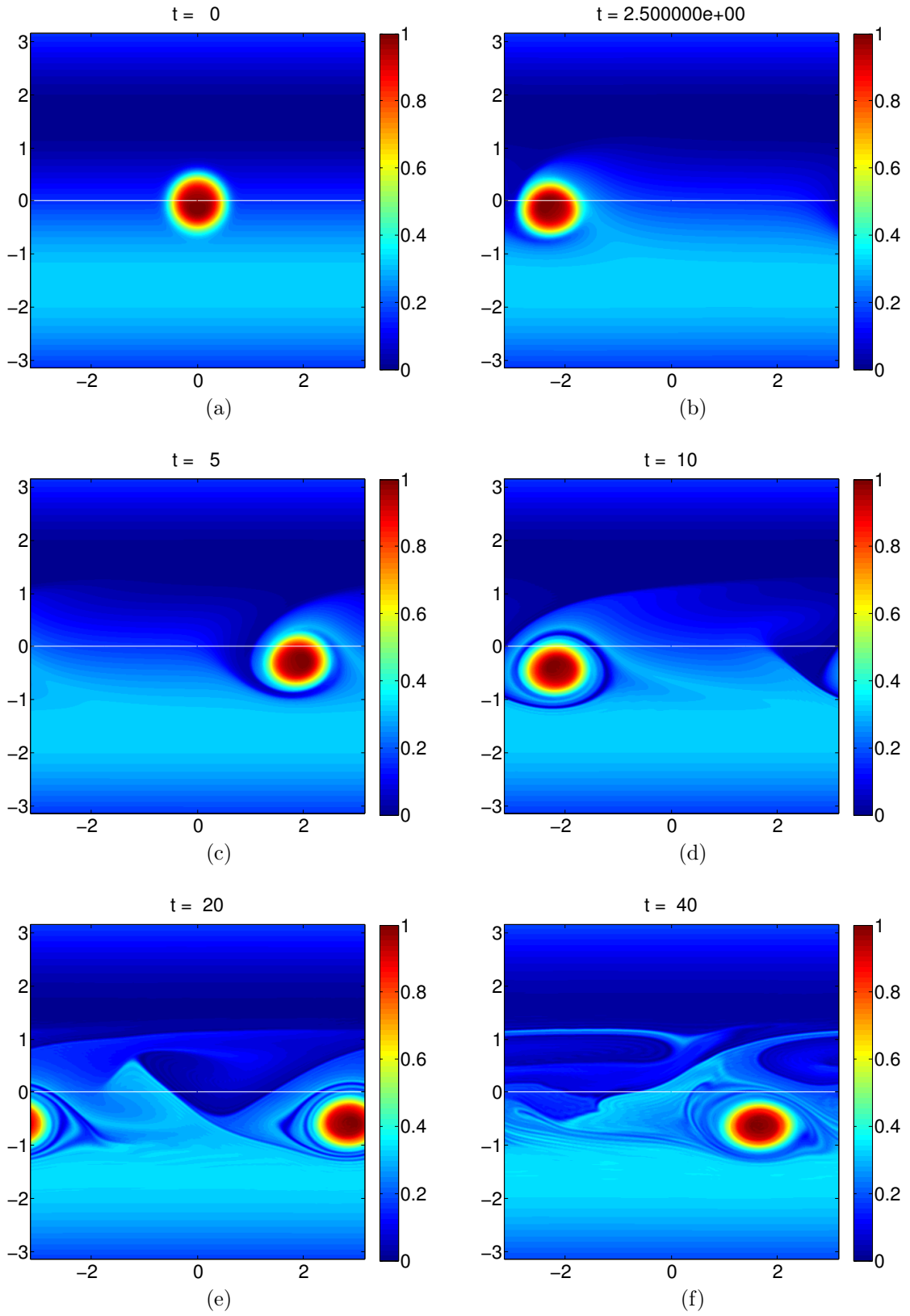

Figure 3-17: $A = 5$, $a = \pi/6$, $R_d/a = 1$, $y_o = \pi/2$, $\beta = 0$.

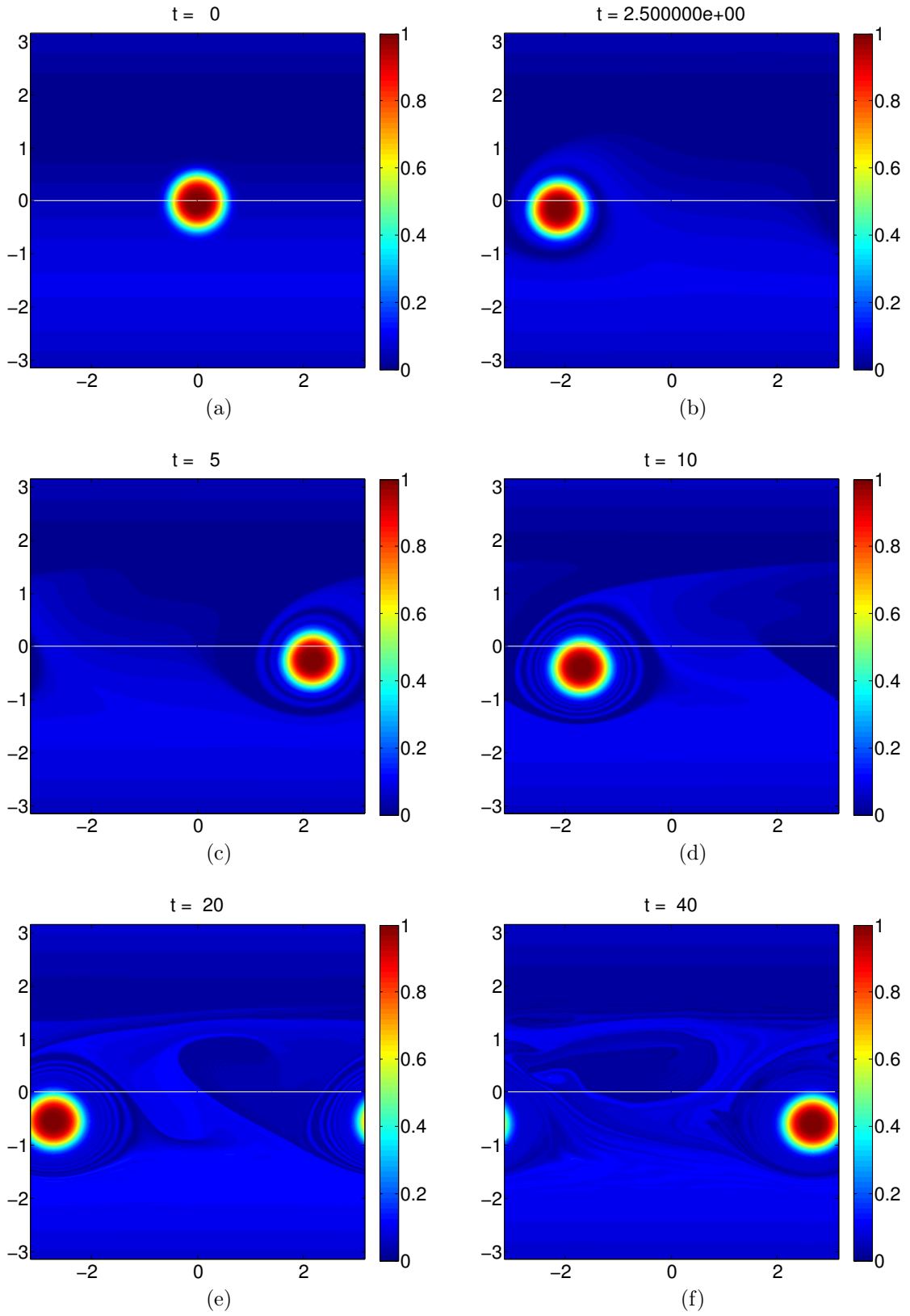

Figure 3-18: $A = 20$, $a = \pi/6$, $R_d/a = 1$, $y_o = \pi/2$, $\beta = 0$.

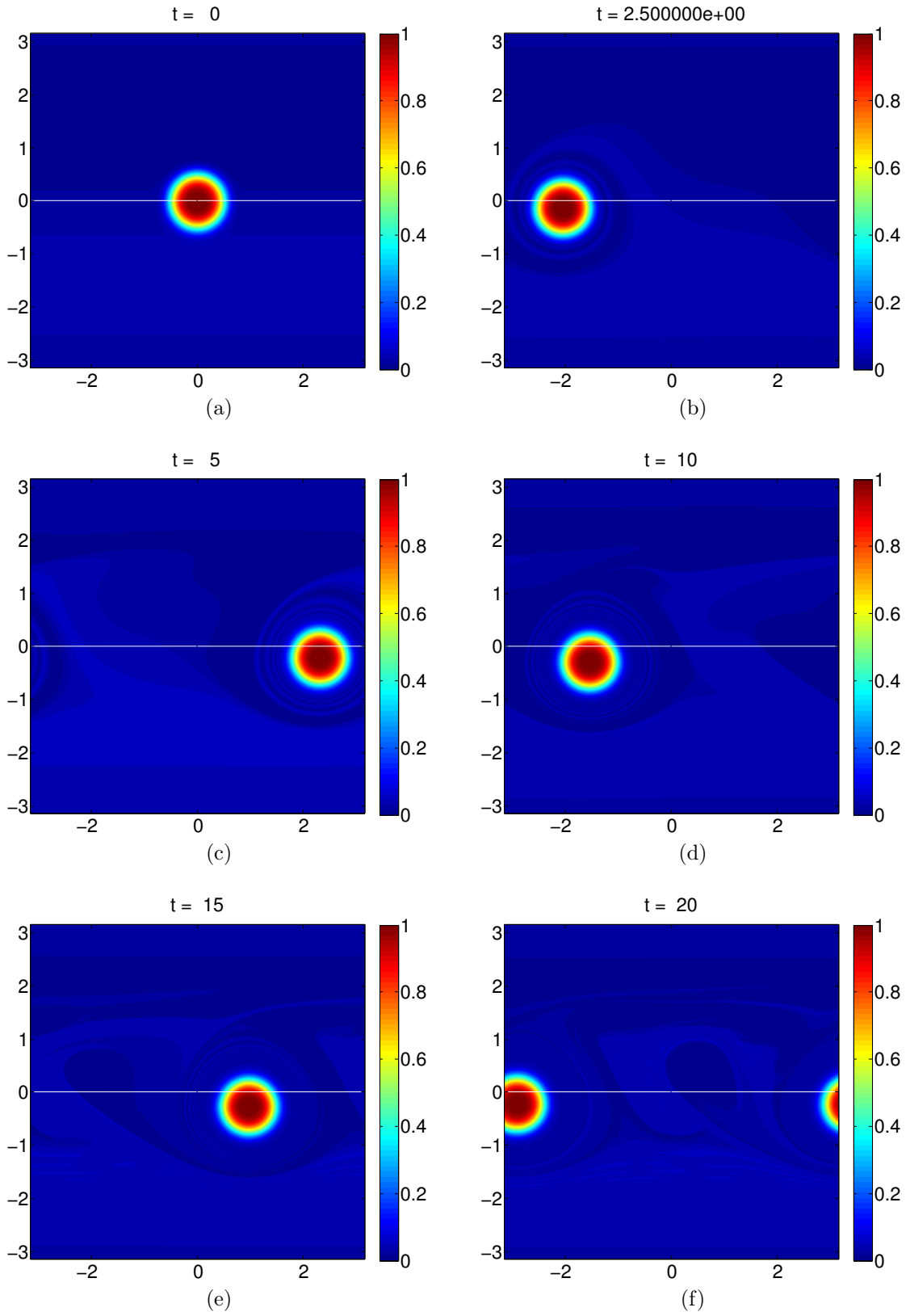

Figure 3-19: $A = 50$, $a = \pi/6$, $R_d/a = 1$, $y_o = \pi/2$, $\beta = 0$.

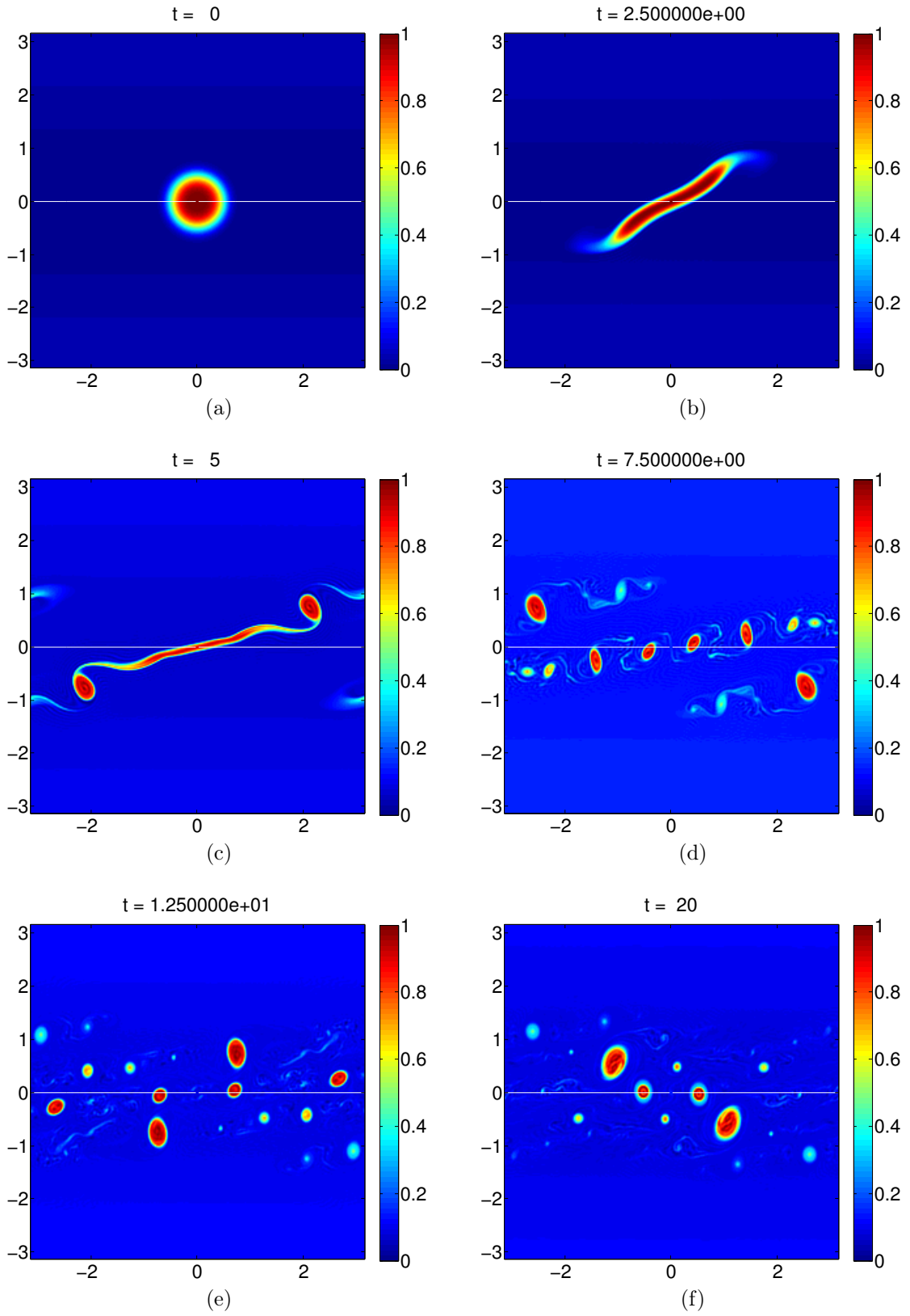

Figure 3-20: $A = 50$, $a = \pi/6$, $R_d/a = 0.25$, $y_o = \pi$, $\beta = 0$.

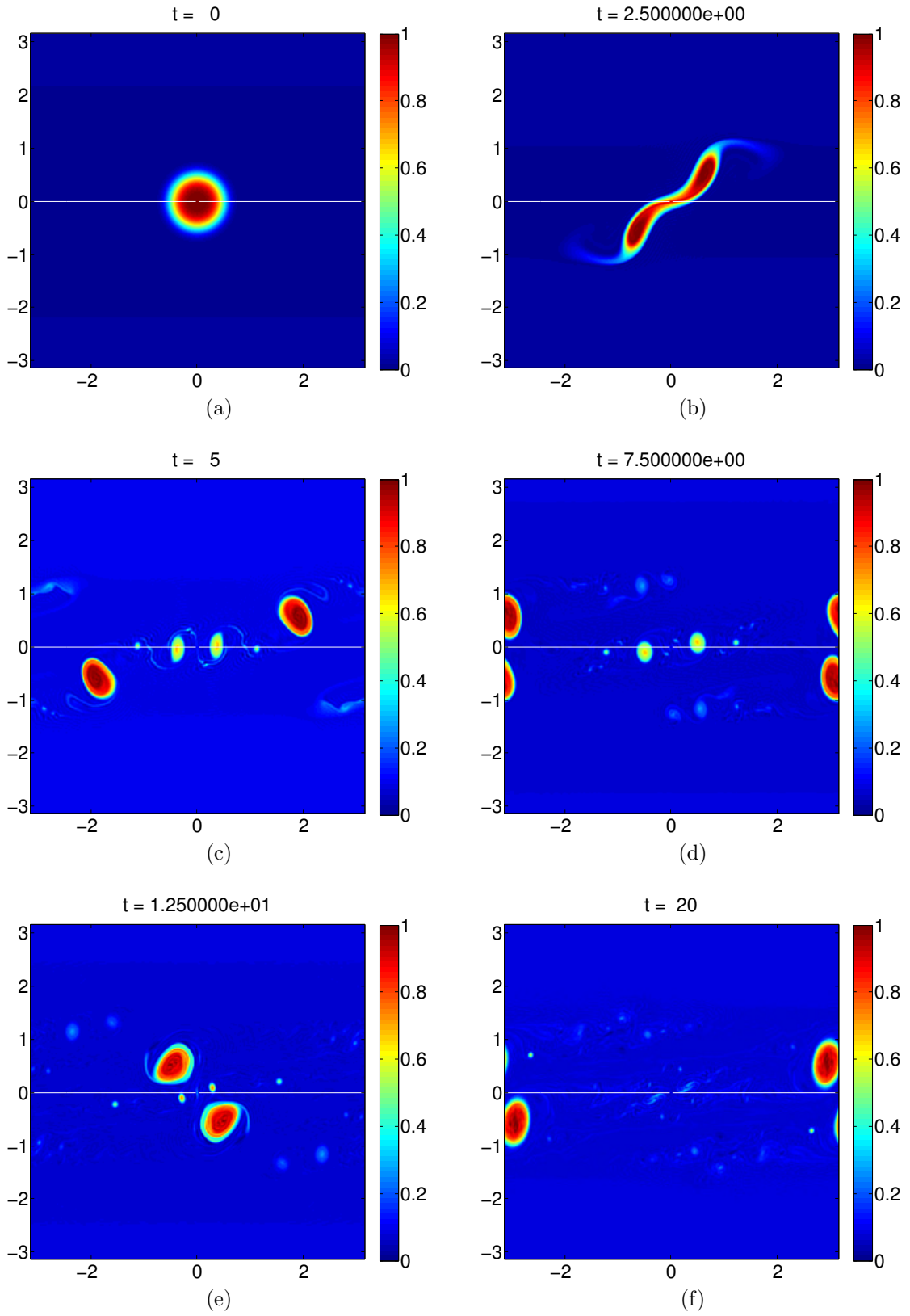

Figure 3-21: $A = 100$, $a = \pi/6$, $R_d/a = 0.25$, $y_o = \pi$, $\beta = 0$.

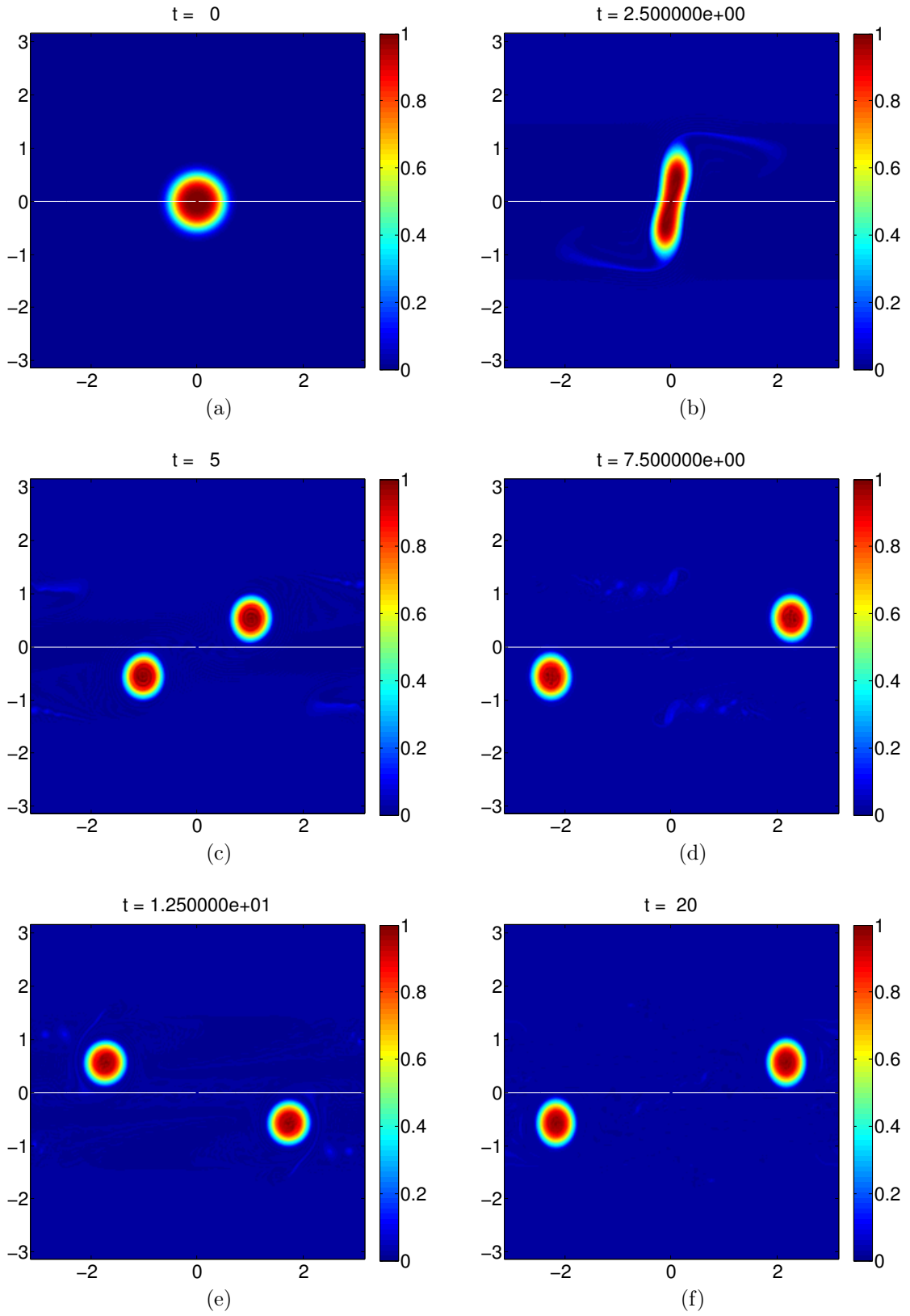

Figure 3-22: $A = 200$, $a = \pi/6$, $R_d/a = 0.25$, $y_o = \pi$, $\beta = 0$.

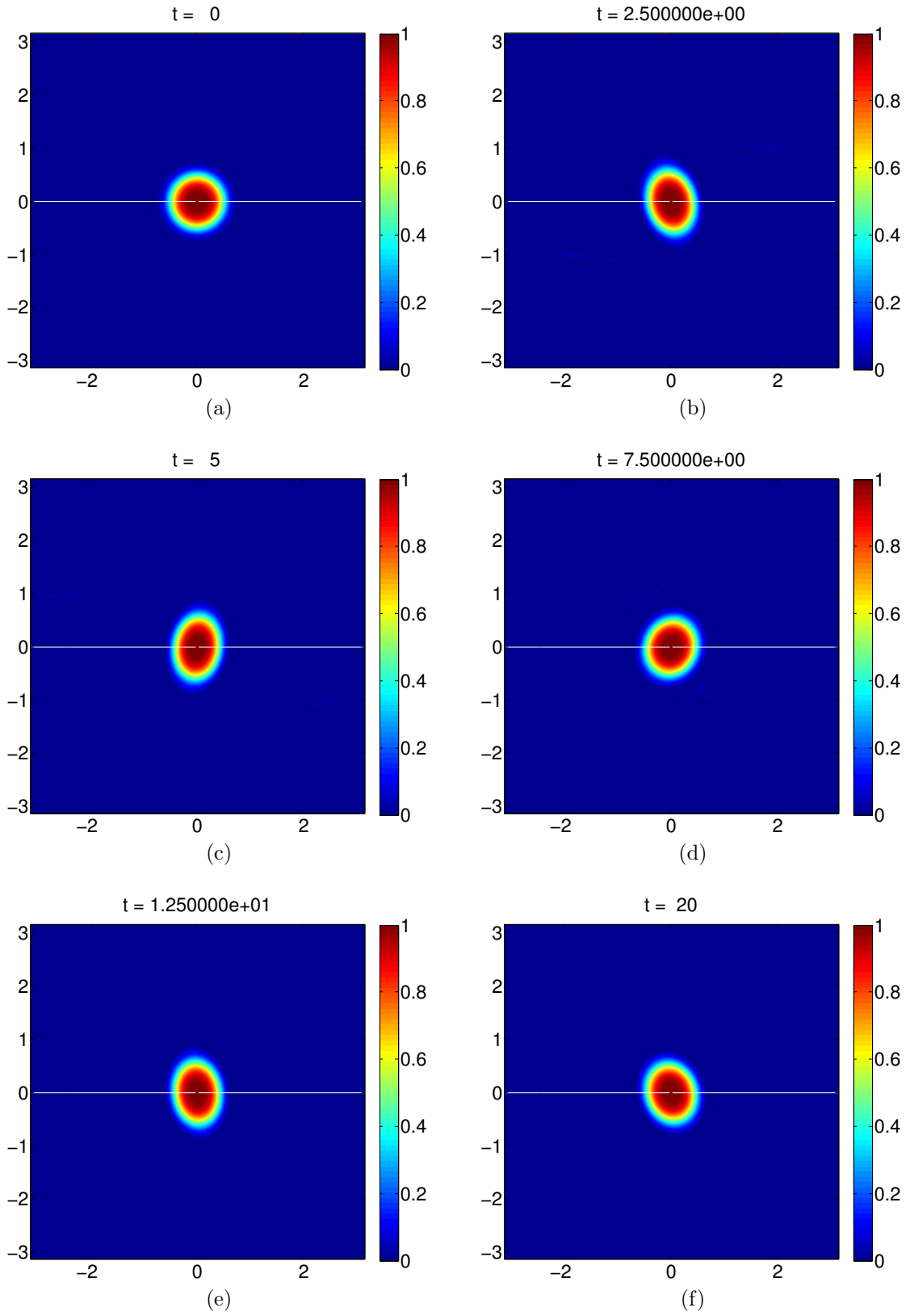

Figure 3-23: $A = 400$, $a = \pi/6$, $R_d/a = 0.25$, $y_o = \pi$, $\beta = 0$.

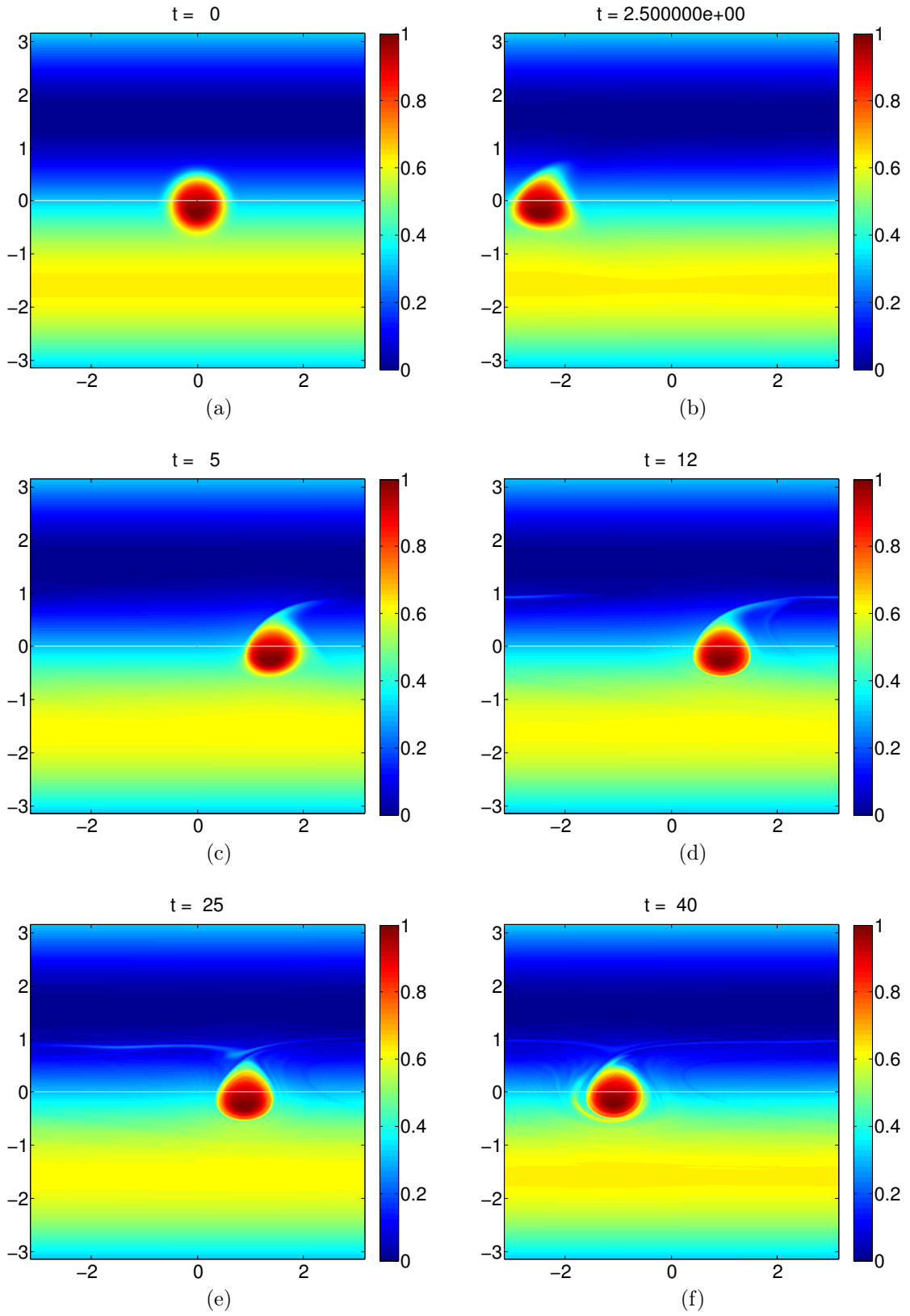

Figure 3-24: $A = 2$, $a = \pi/6$, $R_d/a = 1$, $y_o = \pi/2$, $\beta = 1$.

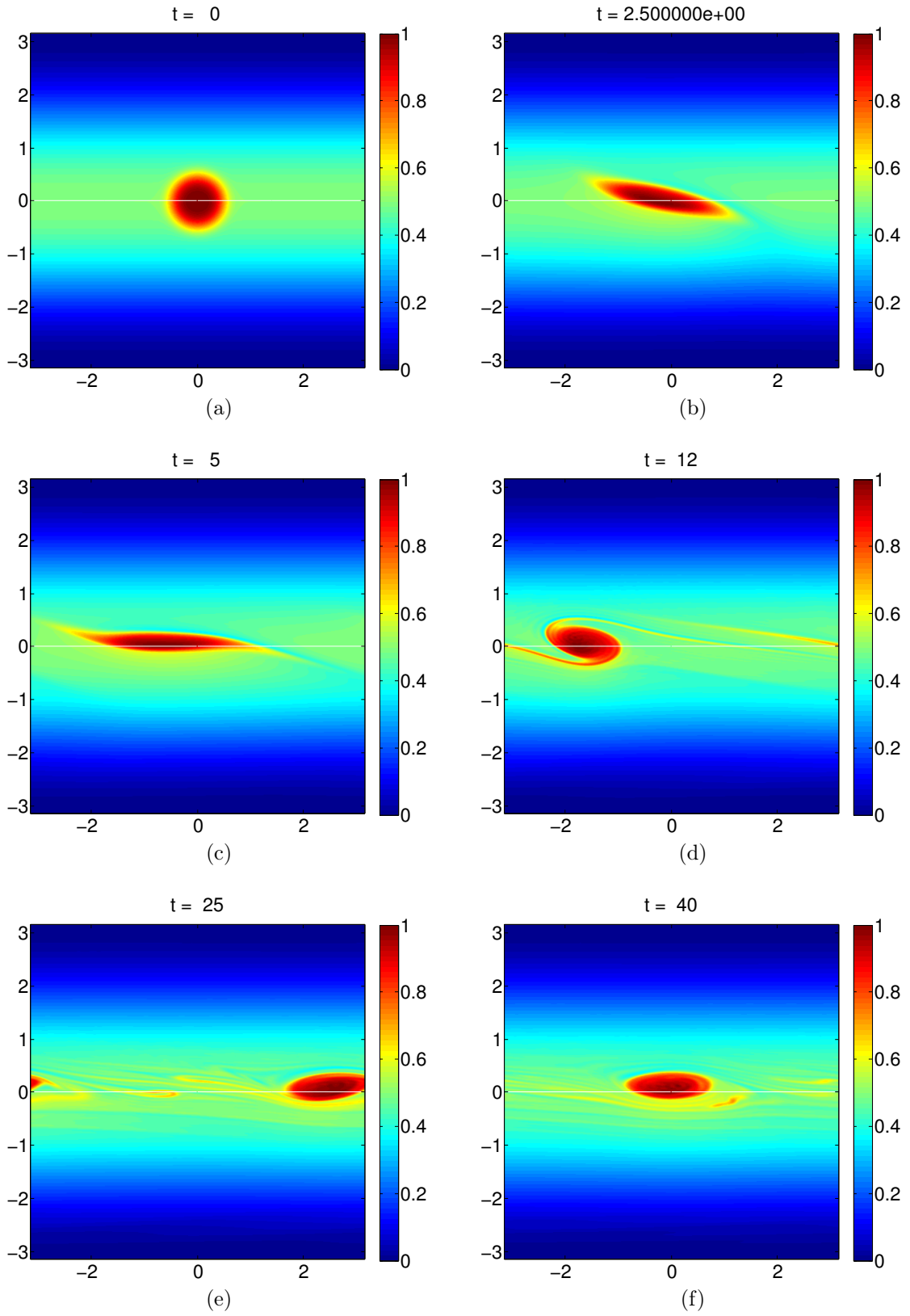

Figure 3-25: $A = 2$, $a = \pi/6$, $R_d/a = 1$, $y_o = 0$, $\beta = 1$.

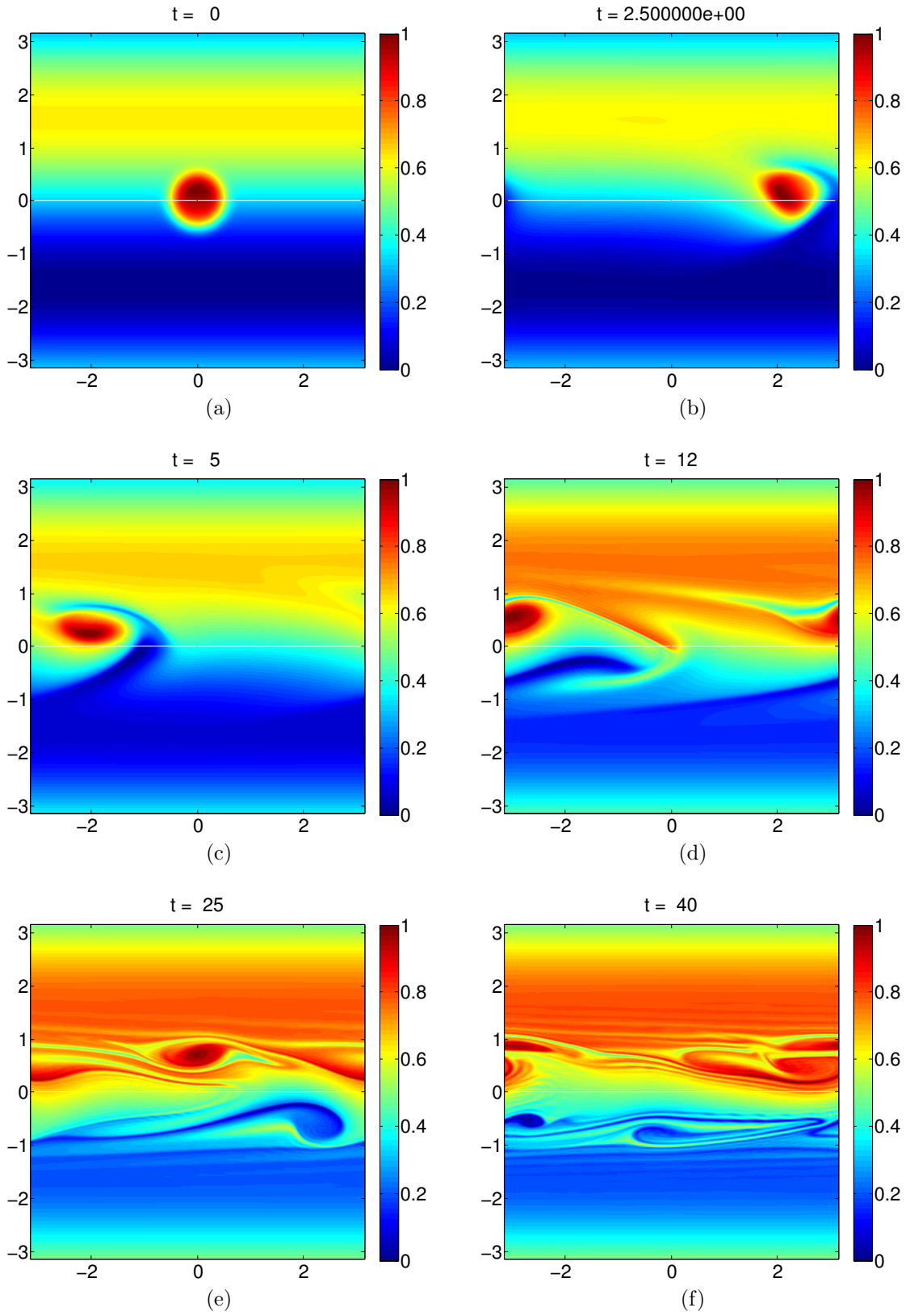

Figure 3-26: $A = 2$, $a = \pi/6$, $R_d/a = 1$, $y_o = -\pi/2$, $\beta = 1$.

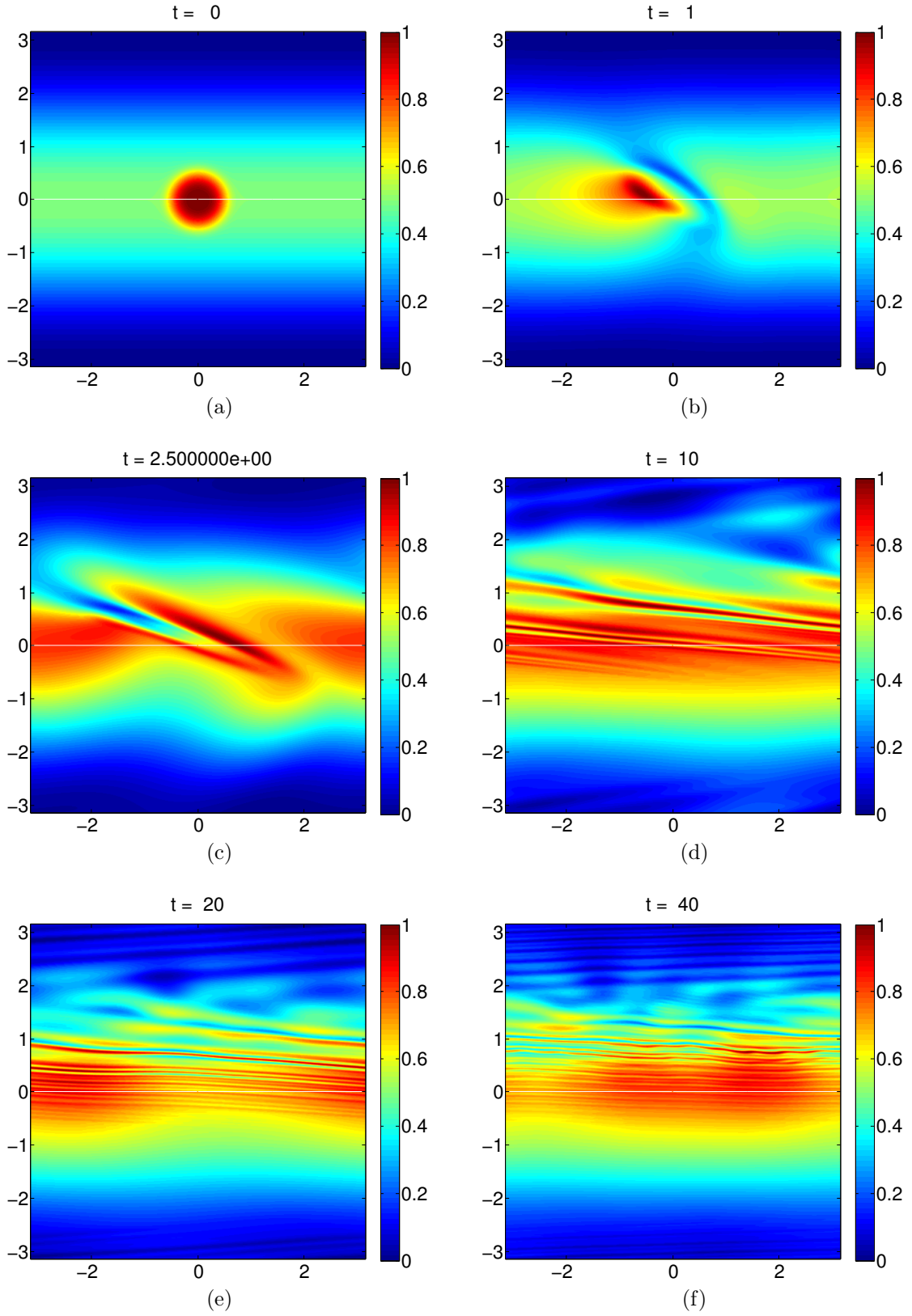

Figure 3-27: $A = 2$, $a = \pi/6$, $R_d/a = 1$, $y_o = 0$, $\beta = 10$.

3.3 Simulated annealing dynamics

Here, we attempt to find steady or quasi-steady vortex states using mainly two methods. We use HDSA when the vortex is not centered ($y_o \neq 0$). We use SA for $y_o = 0$. For HDSA dynamics, we have used the x center of potential vorticity and y center of potential vorticity for the entire flow as our constraints. Remember that these constraints need to be periodic for HDSA. We have made the constraints periodic by introducing boundary layers at the edge of the domain. We have varied a from $\pi/9$ to $\pi/3$, y_o from 0 to $\pi/2$, R_d/a from 0.25 to 1 and A from 5 to 20. Further, we have tracked the x center of potential vorticity of vortex, y center of potential vorticity of vortex, ellipticity (ratio of second moment in x direction to second moment in y direction) of vortex, and the skewness (third moment in y direction, normalized appropriately) of the vortex. Of course, we also track the Hamiltonian and the constraints. Regarding the constraints, not applying them for the $y_o \neq 0$ position leads to the vortex jumping from the initial position to $y_o = 0$ since that is an energy extremum. Further, we have assigned equal weights for ideal and dissipative dynamics ($\alpha = \sigma = 1$ in 2.21) in HDSA or SA. Here is a collection of results that contains most of the behavior.

First, we consider the case $a = \pi/6$ and $A = 5$. We place the vortex at $y_o = 0$ and vary R_d. Refer Figs. 3-28, 3-29 and 3-30. For $R_d = 0.25$, we can clearly see that vortex very quickly goes to the steady state. Remember that in the original Hamiltonian dynamics, the vortex had elongated at an angle to the background flow which depended on the magnitude of shear. Once it had done that, it then rotated (precessed) to become horizontal. Here however, the elongation already happens almost along the x axis or direction of flow, especially the contours of vorticity with higher magnitude. The outer lower vorticity contours visibly elongate more at an angle and then rotate and stretch out into filaments. All this happens due to the symmetric bracket, which acts like a dissipation. Further, the Hamiltonian or energy maximizes (tends to a maximum value). In addition, the area between the vorticity

contours tries to remain constant. Due to all of this, there is little filamentation compared to the H dynamics, or barely any loss of enstrophy. The area of the vortex essentially remains constant. The final vortex is still symmetric because it is at $y_o = 0$, where background vorticity is symmetric. Next, we increase the R_d to 0.625, which means the vorticity of the vortex dominates for a larger radius. We can clearly see that, obeying similar dynamics to the $R_d = 0.25$ case, this vortex becomes elliptical. This time, however, there is much less filamentation. Further, there is a discernible decrease in the aspect ratio of the ellipse because of the greater R_d. In the $R_d = 1$ case, there are barely any filaments and the final steady state looks elliptical with a smaller aspect ratio. Hence as R_d increases, the final vortex tends more towards a circular vortex. In all the cases, the Hamiltonian maximized.

For the next set of simulations, we place the vortex at $\pi/4$ (Figs. 3-31, 3-32, 3-33 with $R_d = 0.25$). This is midway between the center of the prograde region and the tip of the adverse region. The vorticity is not symmetric about the center of vorticity and the vortex begins to feel the curvature in the flow. Due to this the final vortex state is slightly asymmetric about the horizontal due to the $m = 3$ mode slowly creeping in. The vortex begins to have skewness, albeit very small. Another point to note is the asymmetry in the filaments, due to which one of the filaments begins to resemble a tail, Further, note that the final state is not as thin as that for the $y_o = 0$ case. The reason for this is because the background vorticity is higher in the $y_o = 0$ case and hence flattens the vortex more. Next we increase R_d to 0.625. It is seen here that the ellipticity decreases. Further the vortex has a clear tail now.The Hamiltonian maximizes and the vortex reaches a steady state. For $R_d = 1$, the vorticity of the vortex is far more pronounced and the vortex wraps the background over itself. Remember that we had constrained the x center and the y center of vorticity. However, this applies to the entire flow. The vortex can in fact drift (North or South depending on where you are) as well as translate east or west by simply wrapping vorticity around itself (which moves the center of vorticity of the flow up and lets the vortex move down to compensate). Once we have measured the

statistics, we can see that there is a slight negative drift as well as translation. The skewness is still very small since the vortex isn't large enough to sense the curvature in the flow properly. The tail no longer exists. However, the ellipticity decreases as we move from y_o=0 to $y = \pi/2$.

Next, we place the vortex at $y_o = \pi/2$, which is half in the prograde shear and the other half in the adverse shear (Figs. 3-35, 3-35 and 3-35). For $R_d = 0.25$, the final state is seen to be resembling an $m = 3$ or an upright triangle. We have already explained the physics behind such a shape in the previous section. The only issue here is that the Hamiltonian keeps increasing and does not show any signs of reaching an asymptotic value. The ellipticity becomes less than 1. The skewness on the other hand increases dramatically to 0.2 at time $t = 1$ from 0 at $t = 0$. There is also a very slight movement of the center of vorticity towards South-West. It could be that there is no steady state at $y_o = \pi/2$, and perhaps the vortex has to drift down slightly to find a latitude at which it can settle. This is similar to what was reported by **?**. The behavior is similar for the higher R_d cases, except that it drifts and translates more, since a higher R_d means it can in fact wrap the background around it. However, in the higher R_d cases (more dominant vorticity), the skewness is lowered and the vortex resembles more a circular vortex.

The remaining simulations examine $A = 10$ and $A = 20$. As A is increased to 10 and beyond for R_d of 0.625 or 1, keeping the rest of the variables constant, the ellipticity decreases. Further, the skewness also decreases. In addition, we begin to see a lot of unsteady states or ones that drift and translate. Also, the vortices begin to dominate and alter the background. Only $R_d = 0.25$ cases give steady states and even then it is unsteady for the $y_o = \pi/2$ case. The $a = \pi/9$ simulations gave a lot of steady states except of course at $y_o = \pi/2$ and higher R_d, where the shape was at least quasi-steady. The vortex was found to be too small to come under any major influence of the curvature of the flow.

The simulations for $a = \pi/9$ and $a = \pi/6$ have been listed in the form of tables (Tables 3.1 and 3.2) with appropriate comments. The $a = \pi/3$ behavior is similar for

$A = 5$. However, for $A = 10$ and $A = 20$, the background flow is altered drastically, especially for the higher R_d cases, where the vortex drifts (also an issue for $A = 20$ case for $y_o \neq 0$. $A = 2$ showed better steady states.

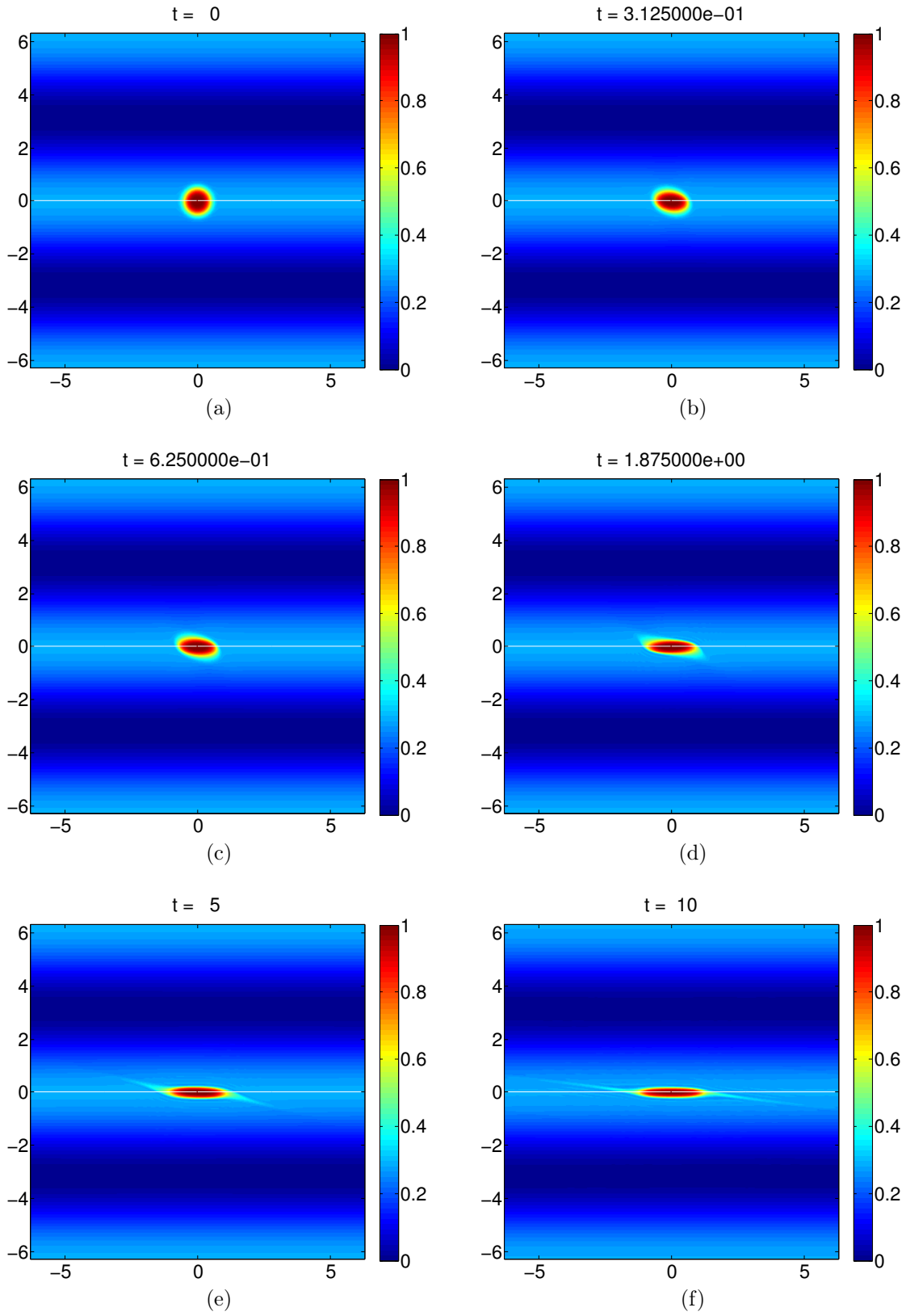

Figure 3-28: $A = 5$, $a = \pi/6$, $R_d/a = 0.25$, $y_o = 0$, $\beta = 0$.

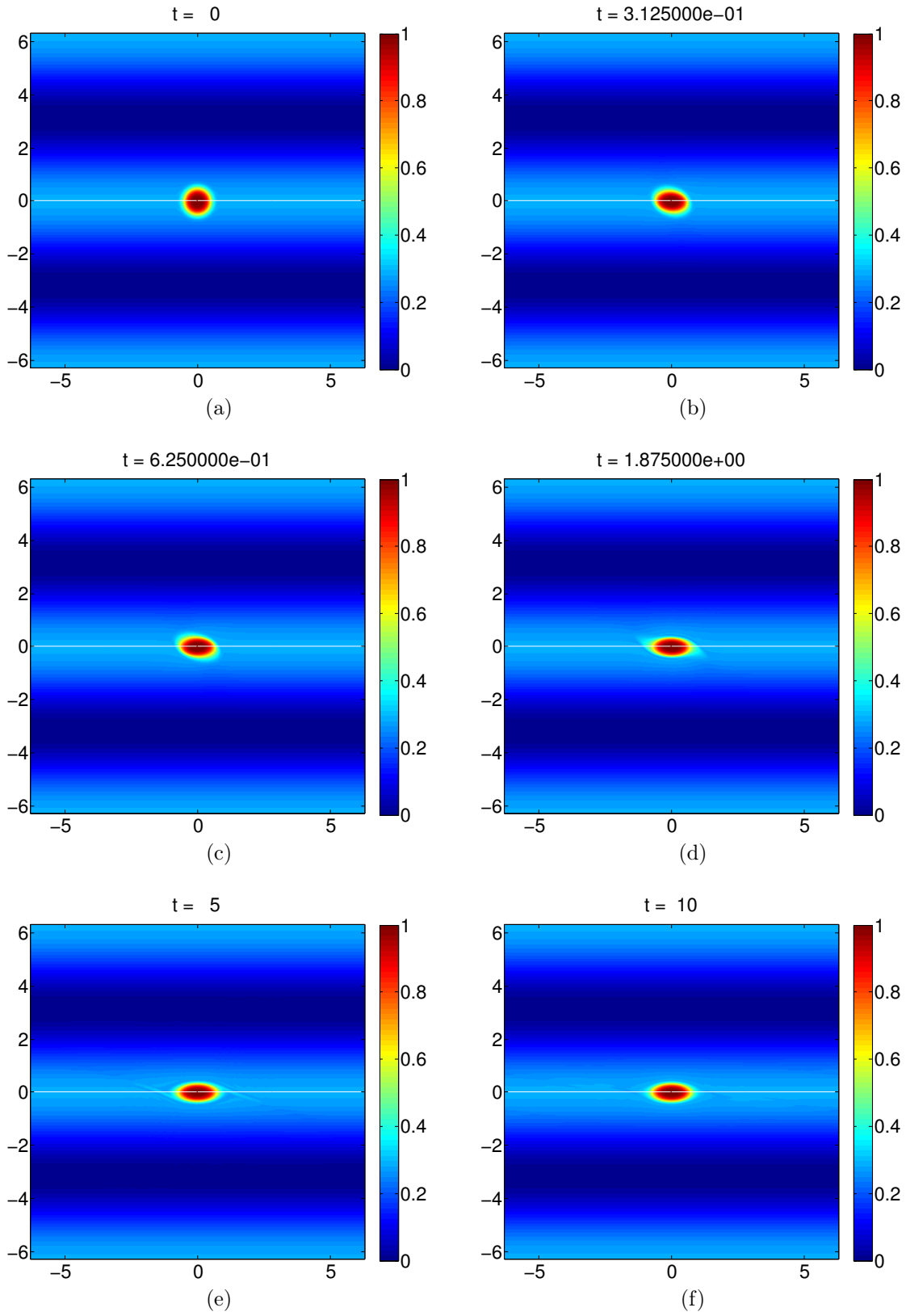

Figure 3-29: $A = 5$, $a = \pi/6$, $R_d/a = 0.625$, $y_o = 0$, $\beta = 0$.

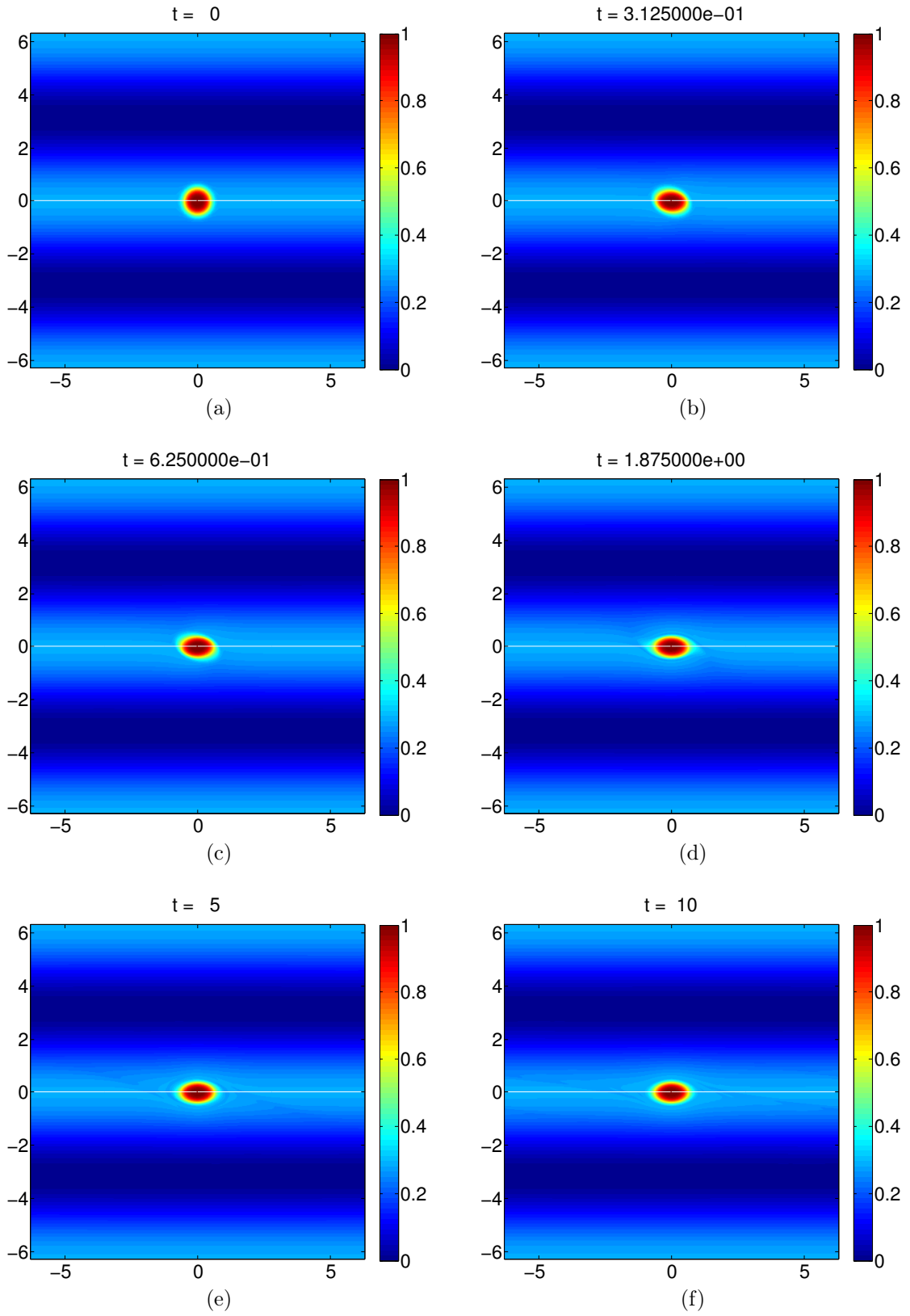

Figure 3-30: $A = 5$, $a = \pi/6$, $R_d/a = 1$, $y_o = 0$, $\beta = 0$.

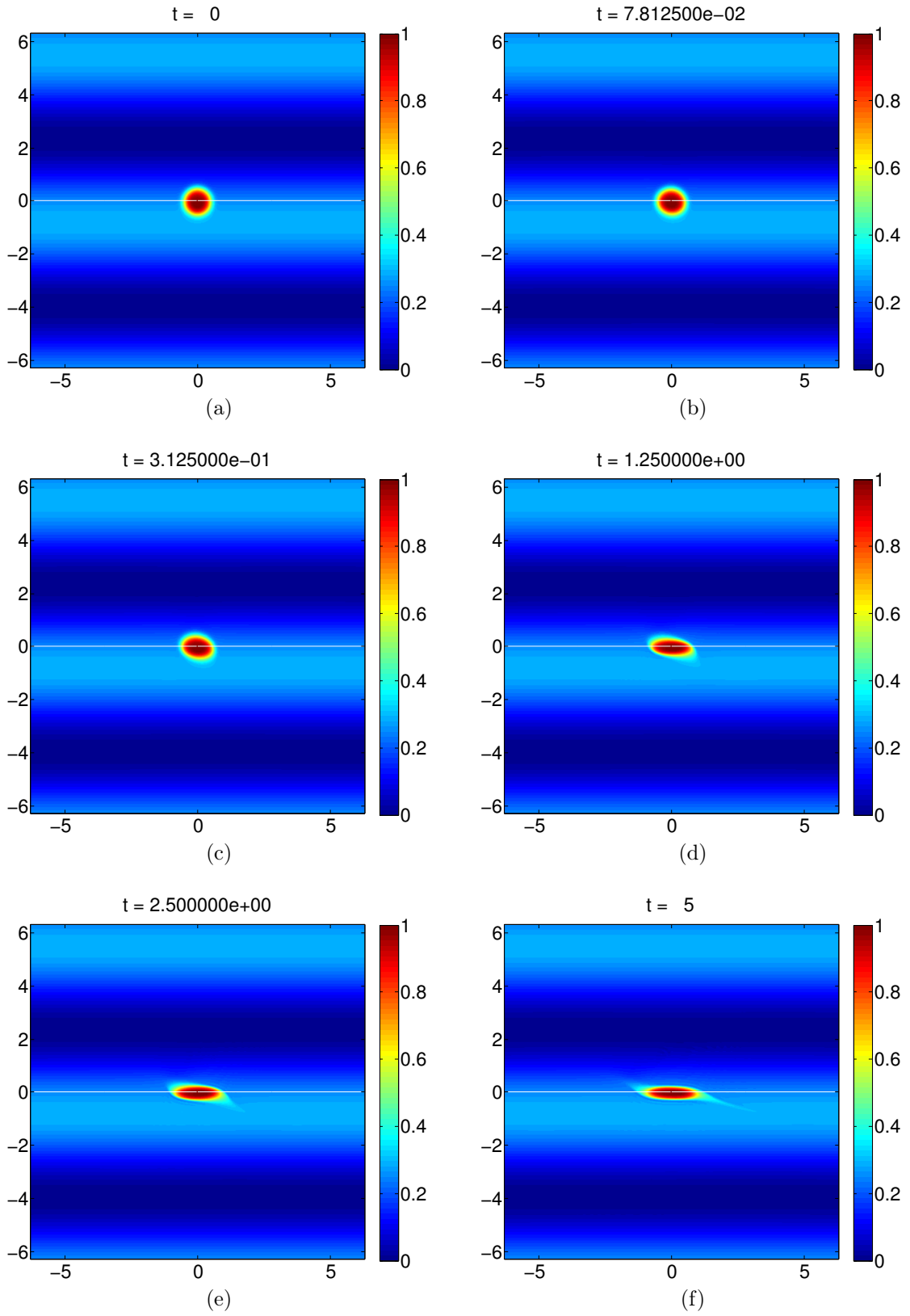

Figure 3-31: $A = 5$, $a = \pi/6$, $R_d/a = 0.25$, $y_o = \pi/4$, $\beta = 0$.

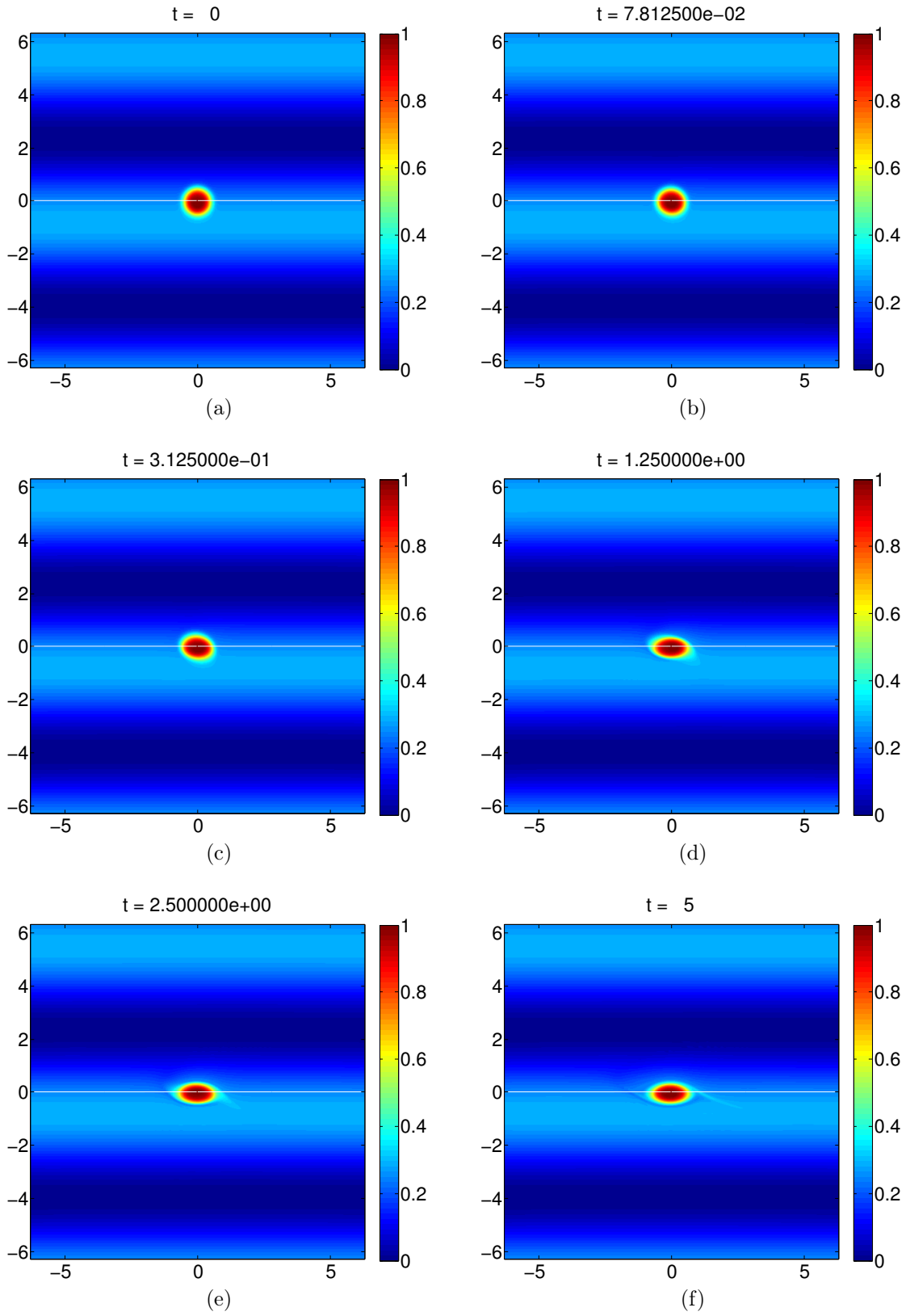

Figure 3-32: $A = 5$, $a = \pi/6$, $R_d/a = 0.625$, $y_o = \pi/4$, $\beta = 0$.

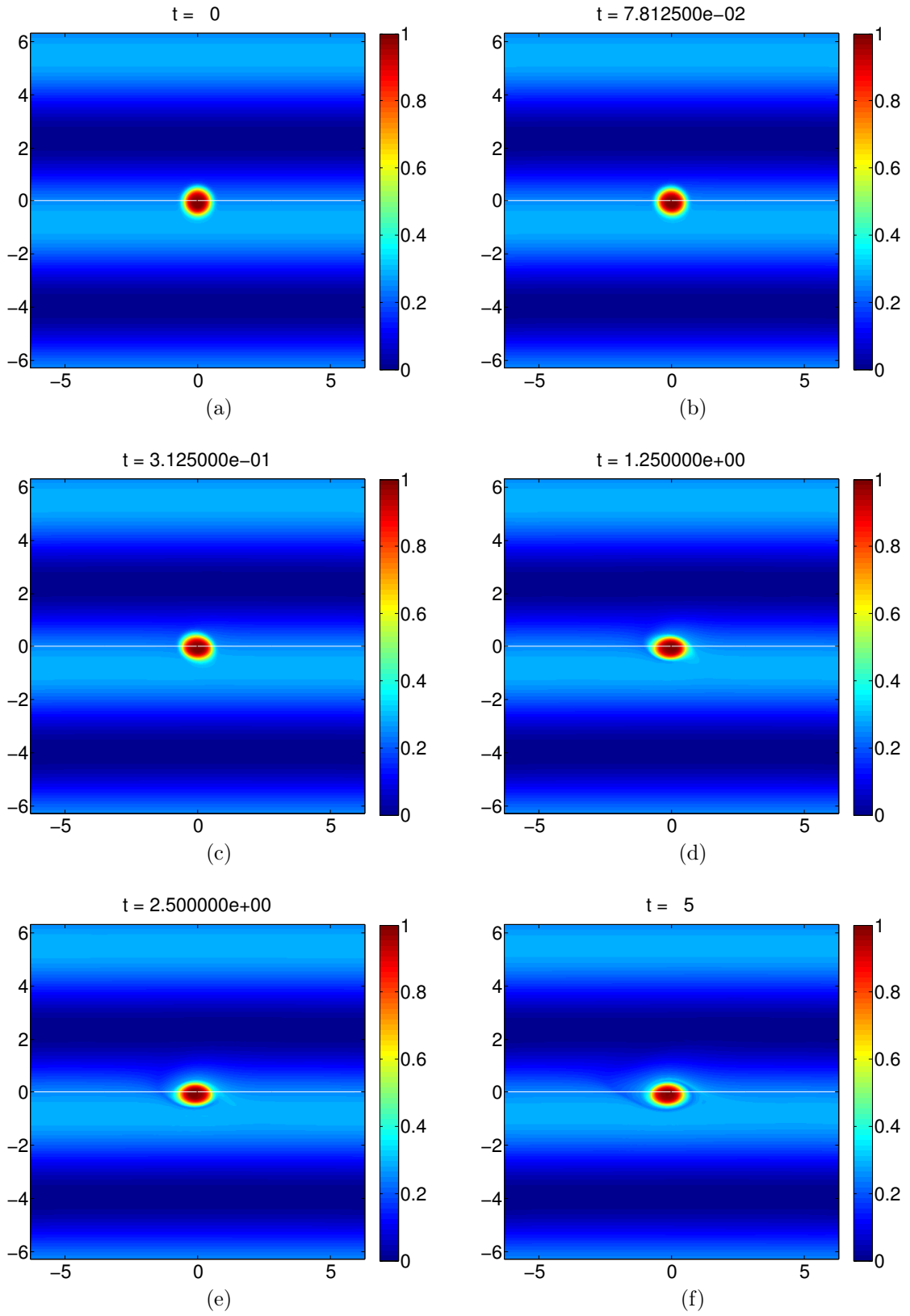

Figure 3-33: $A = 5$, $a = \pi/6$, $R_d/a = 1$, $y_o = \pi/4$, $\beta = 0$.

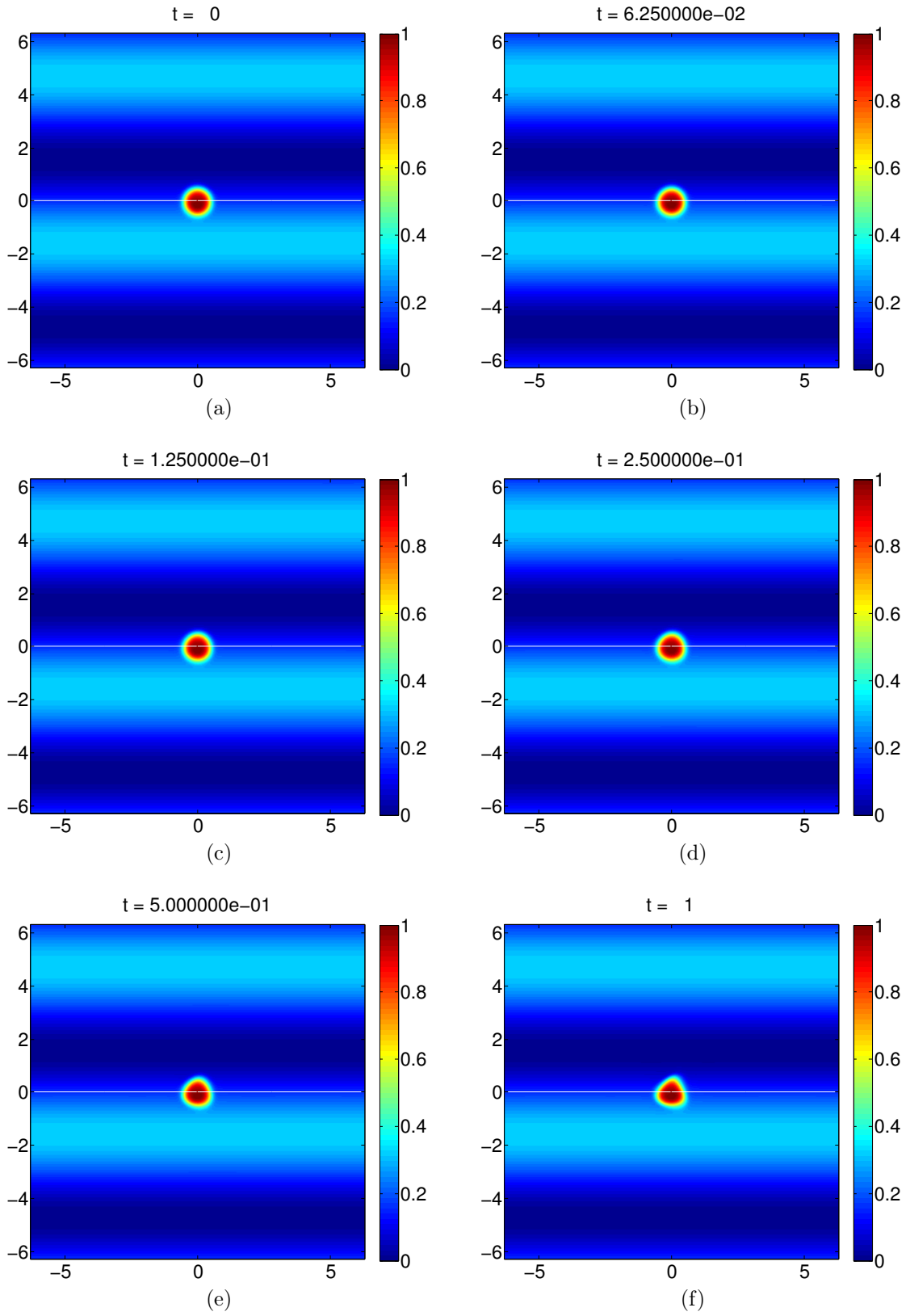

Figure 3-34: $A = 5$, $a = \pi/6$, $R_d/a = 0.25$, $y_o = \pi/2$, $\beta = 0$.

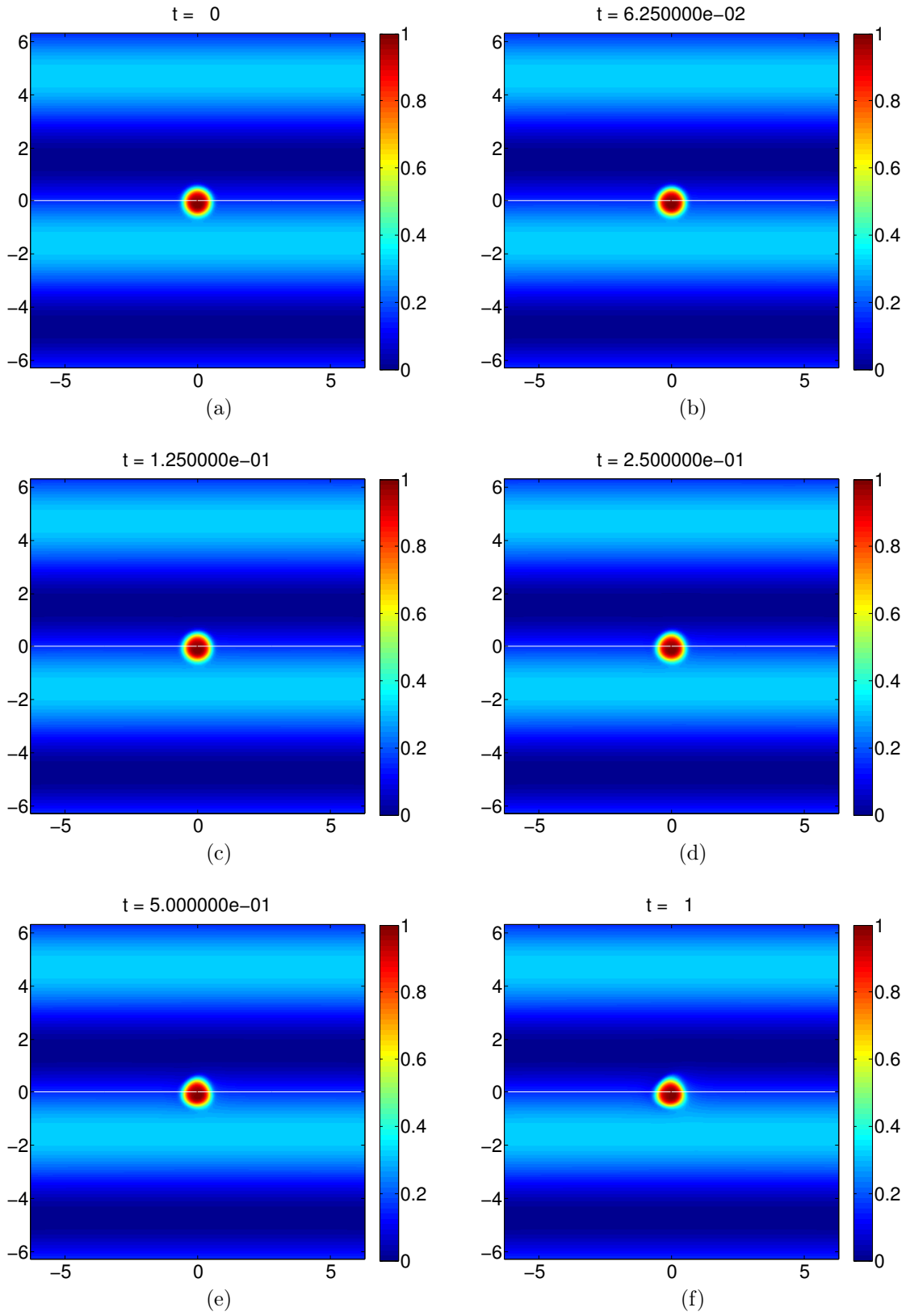

Figure 3-35: $A = 5$, $a = \pi/6$, $R_d/a = 0.625$, $y_o = \pi/2$, $\beta = 0$.

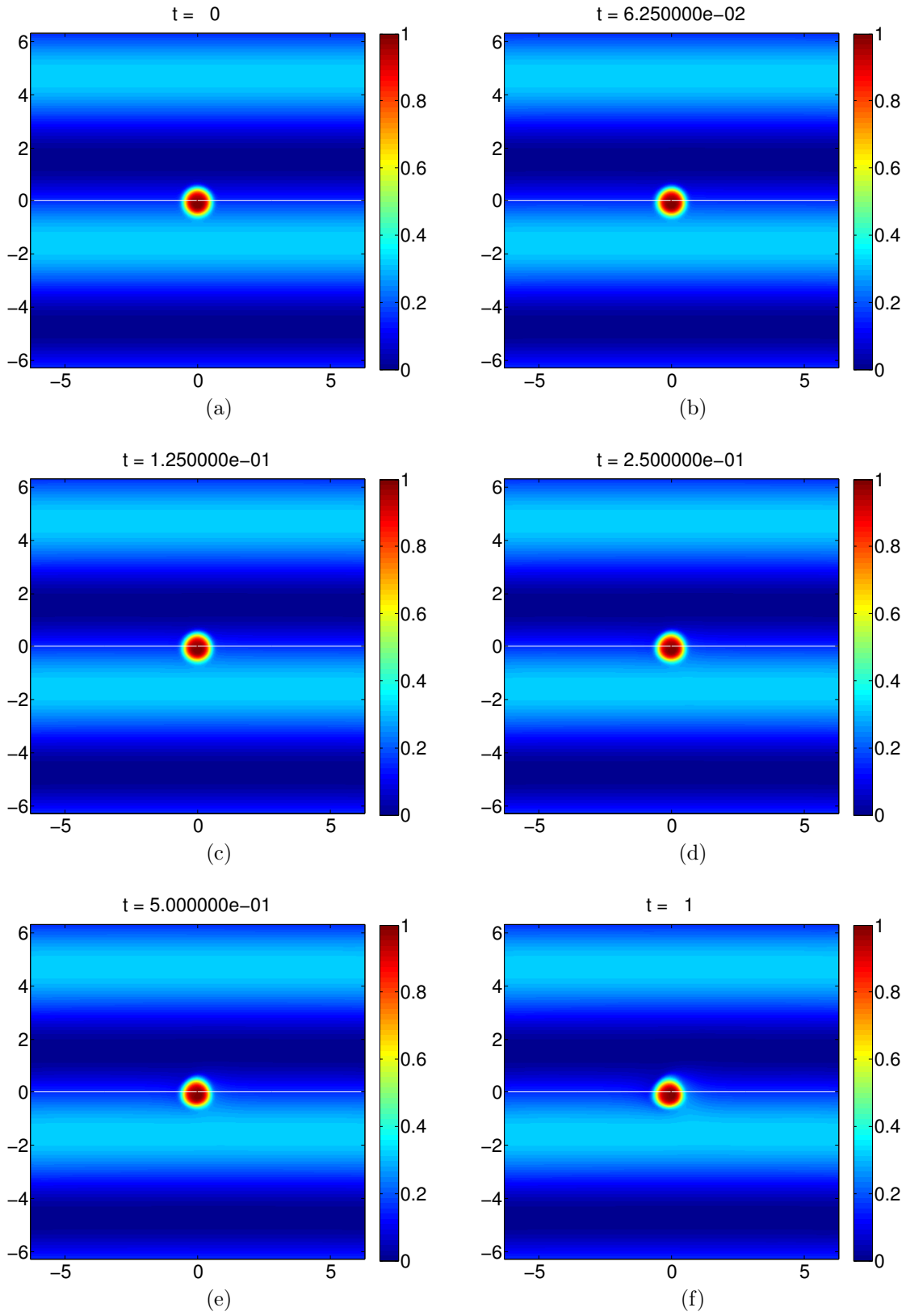

Figure 3-36: $A = 5$, $a = \pi/6$, $R_d/a = 1$, $y_o = \pi/2$, $\beta = 0$.

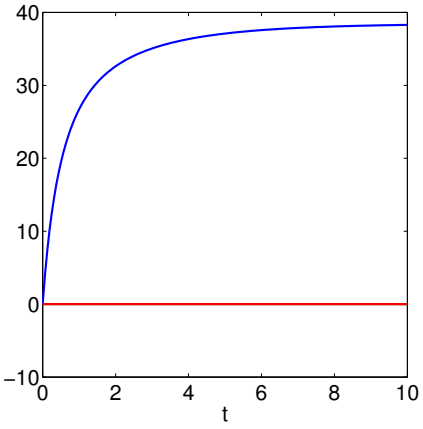

(a) $y_o = 0$

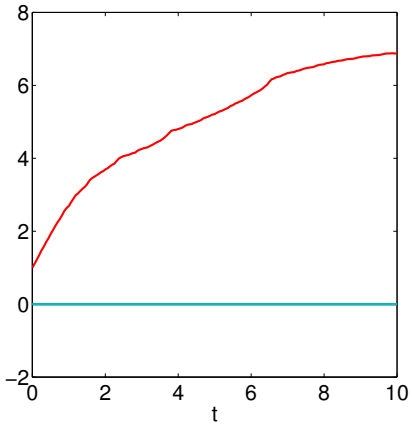

(b) $y_o = 0$

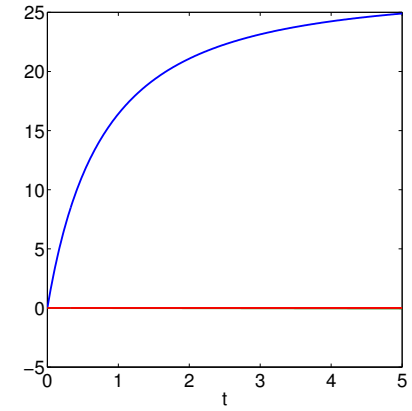

(c) $y_o = \pi/4$

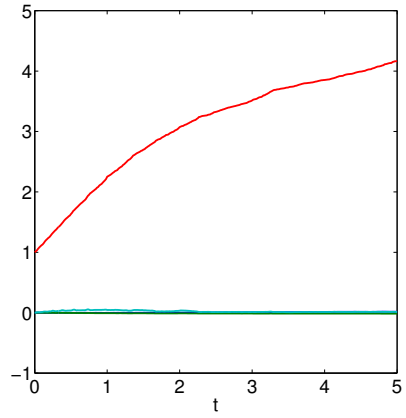

(d) $y_o = \pi/4$

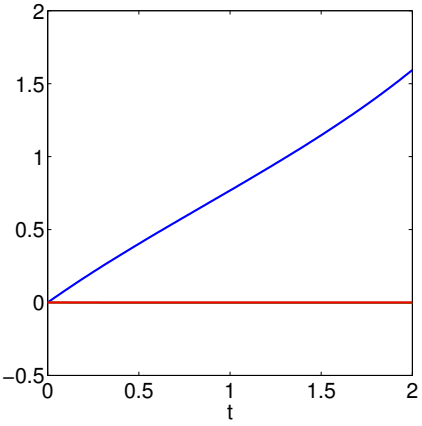

(e) $y_o = \pi/2$

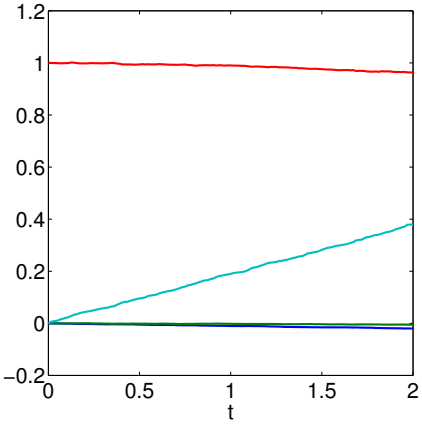

(f) $y_o = \pi/2$

Figure 3-37: $A = 5$, $a = \pi/6$, $R_d/a = 0.25$, $y_o = 0$. Plots on the left show the Hamiltonian (blue) and the constraints c1 (green) and c2 (red) . On the right, we have the statistics - Ellipticity (red), skewness (cyan), x center of vorticity (blue), y center of vorticity (green).

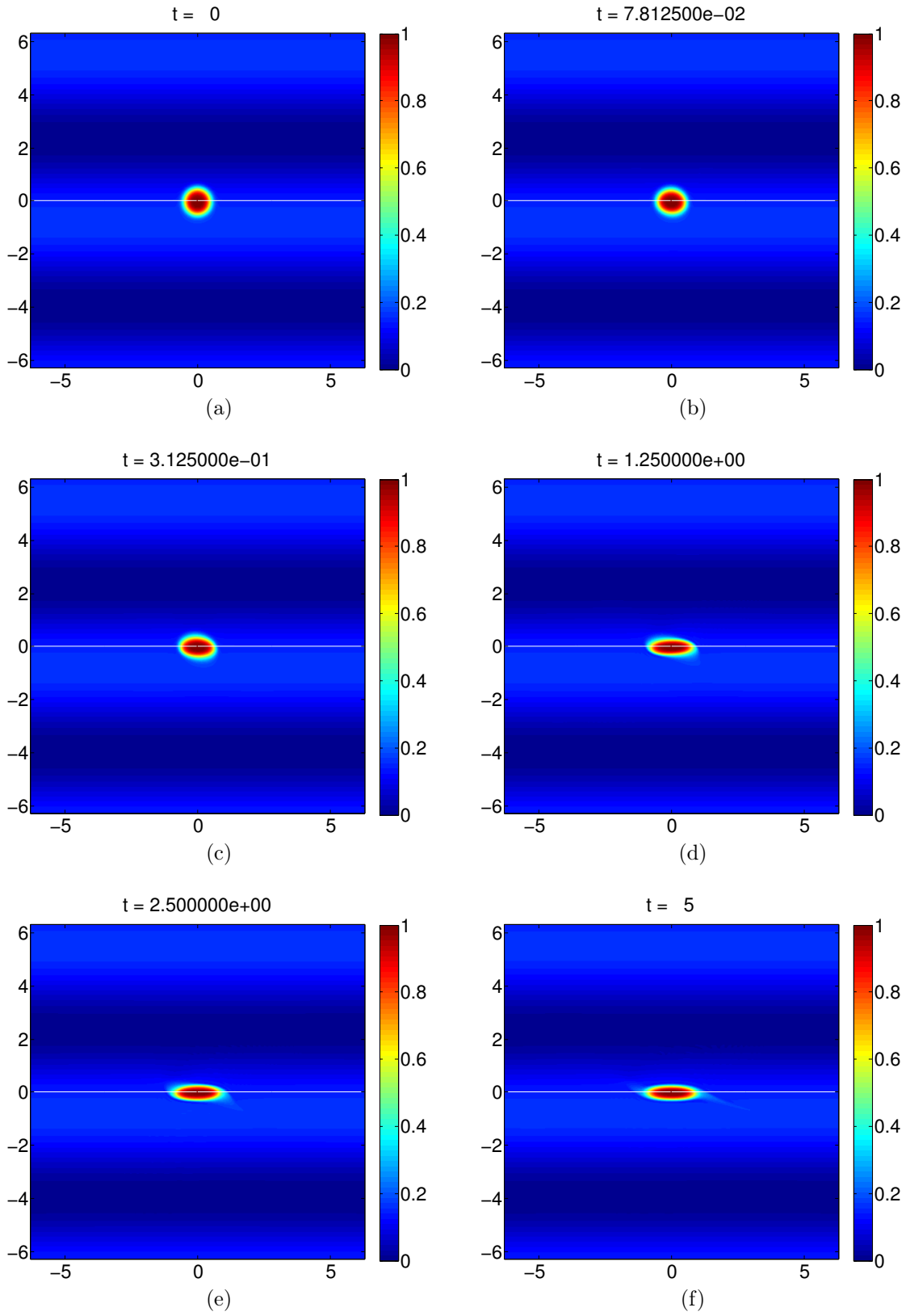

Figure 3-38: $A = 10$, $a = \pi/6$, $R_d/a = 0.25$, $y_o = \pi/4$, $\beta = 0$.

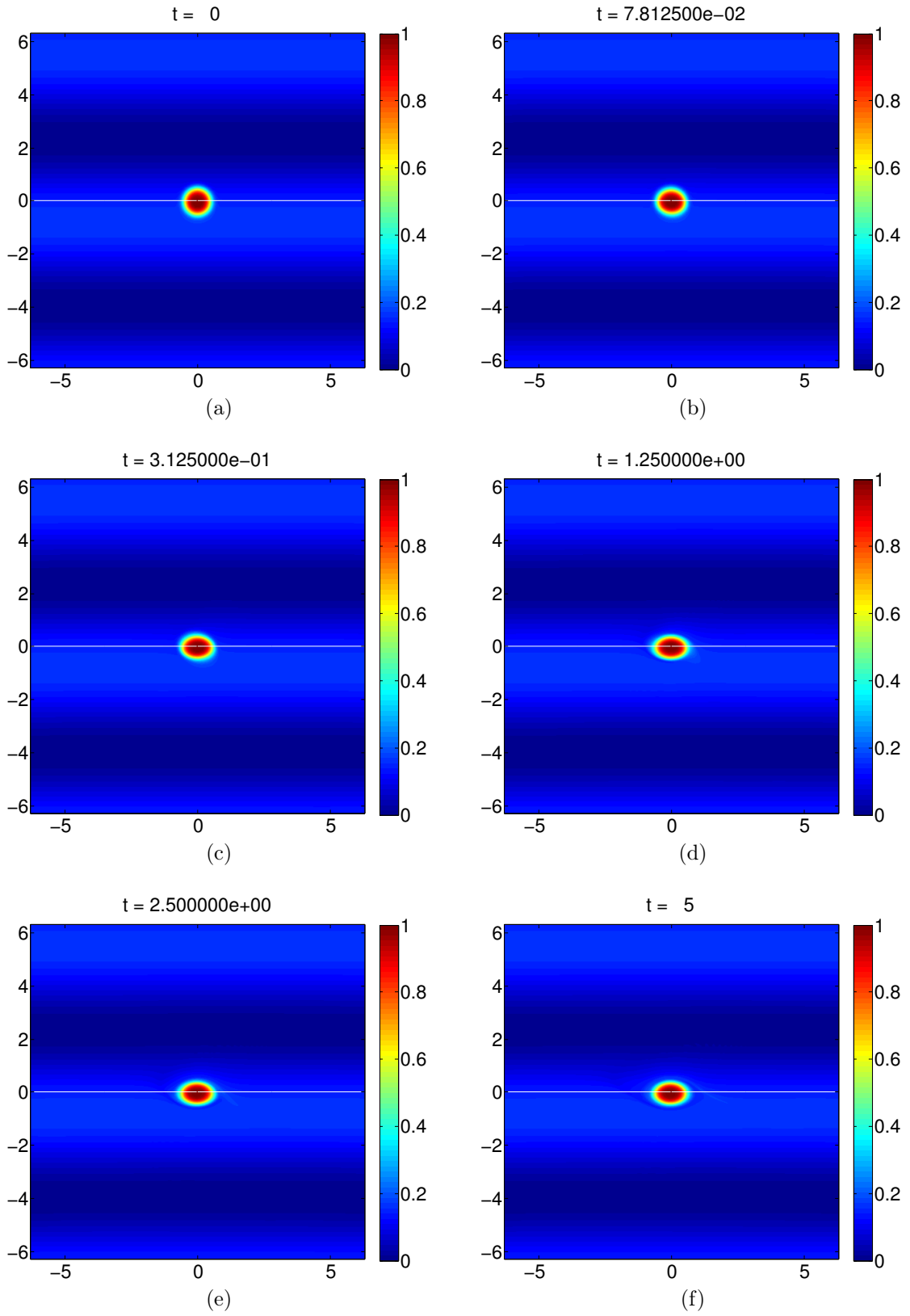

(a) (b) (c) (d) (e) (f)

Figure 3-39: $A = 10$, $a = \pi/6$, $R_d/a = 0.625$, $y_o = \pi/4$, $\beta = 0$.

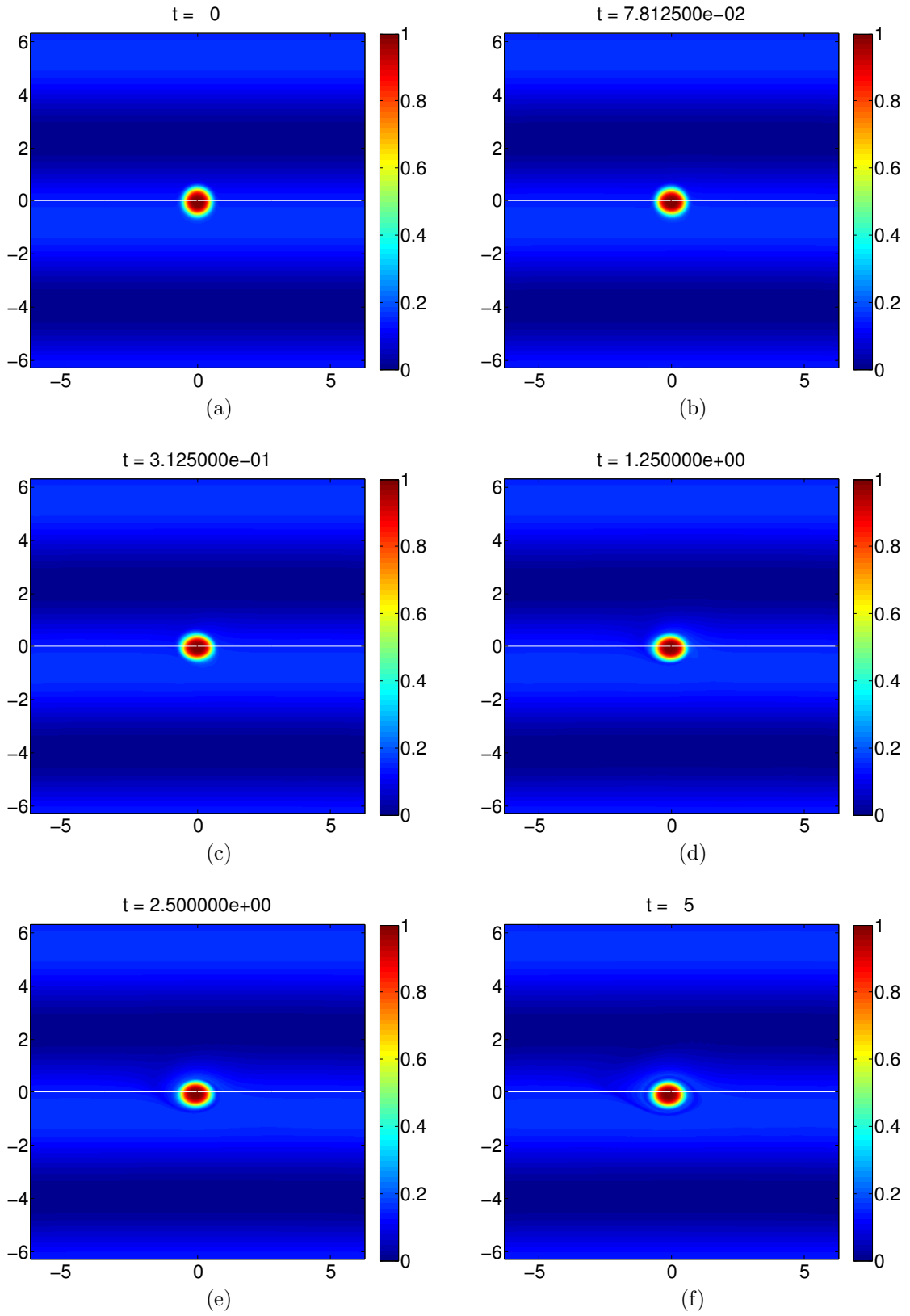

Figure 3-40: $A = 10$, $a = \pi/6$, $R_d/a = 1$, $y_o = \pi/4$, $\beta = 0$.

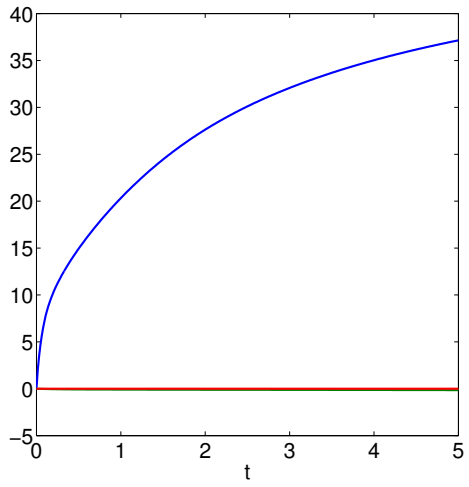

(a) $y_o = 0$

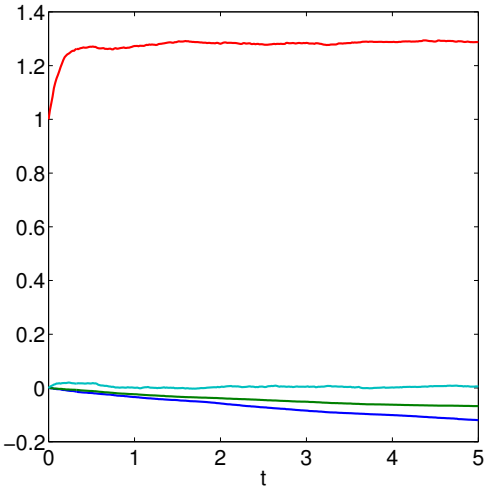

(b) $y_o = 0$

Figure 3-41: $A = 10$, $a = \pi/6$, $R_d/a = 1$, $y_o = \pi/4$. (a) shows the Hamiltonian (blue) and the constraints c1 (green) and c2 (red) . (b) shows the statistics - Ellipticity (red), skewness (cyan), x center of vorticity (blue), y center of vorticity (green).

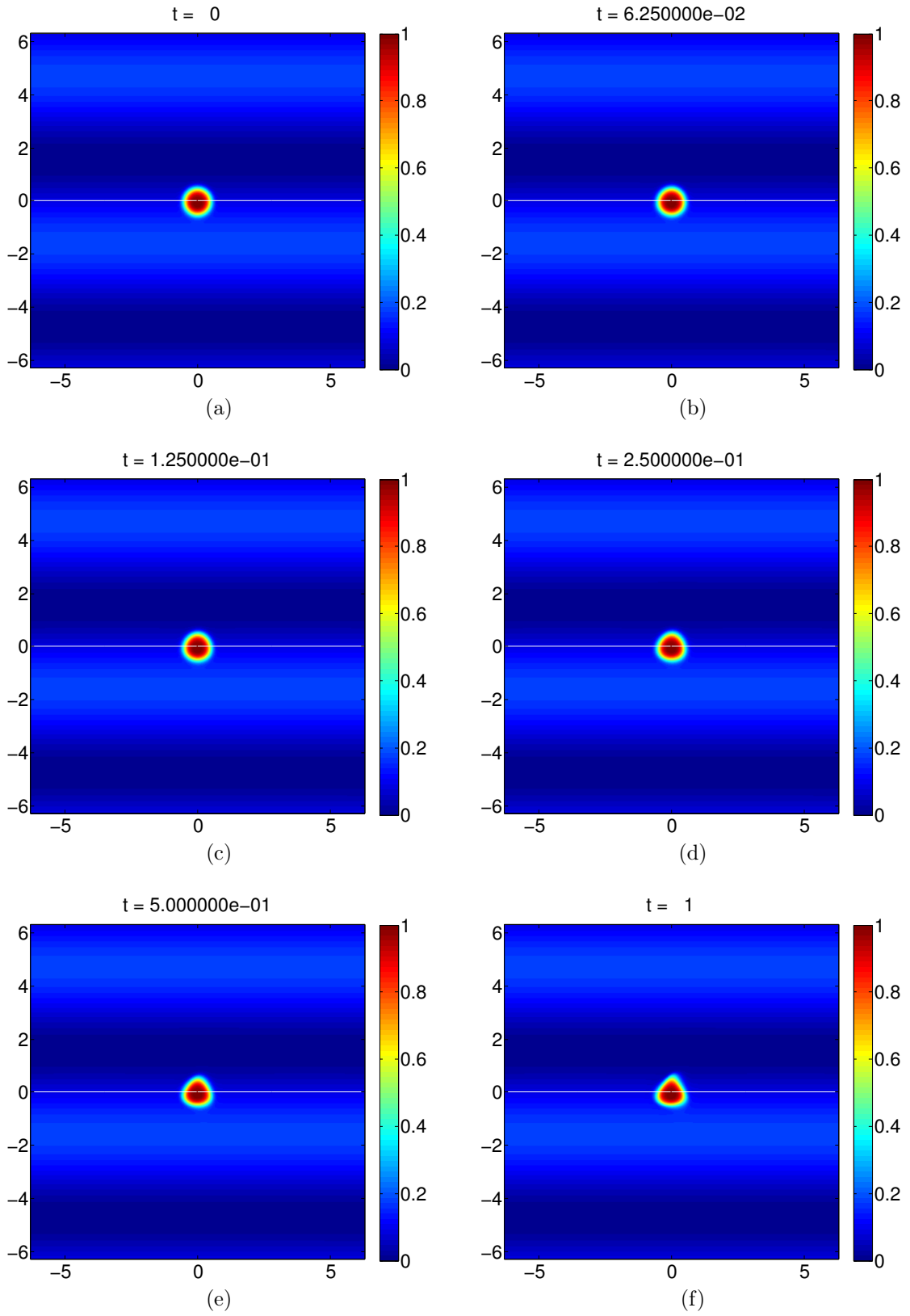

Figure 3-42: $A = 10$, $a = \pi/6$, $R_d/a = 0.25$, $y_o = \pi/2$, $\beta = 0$.

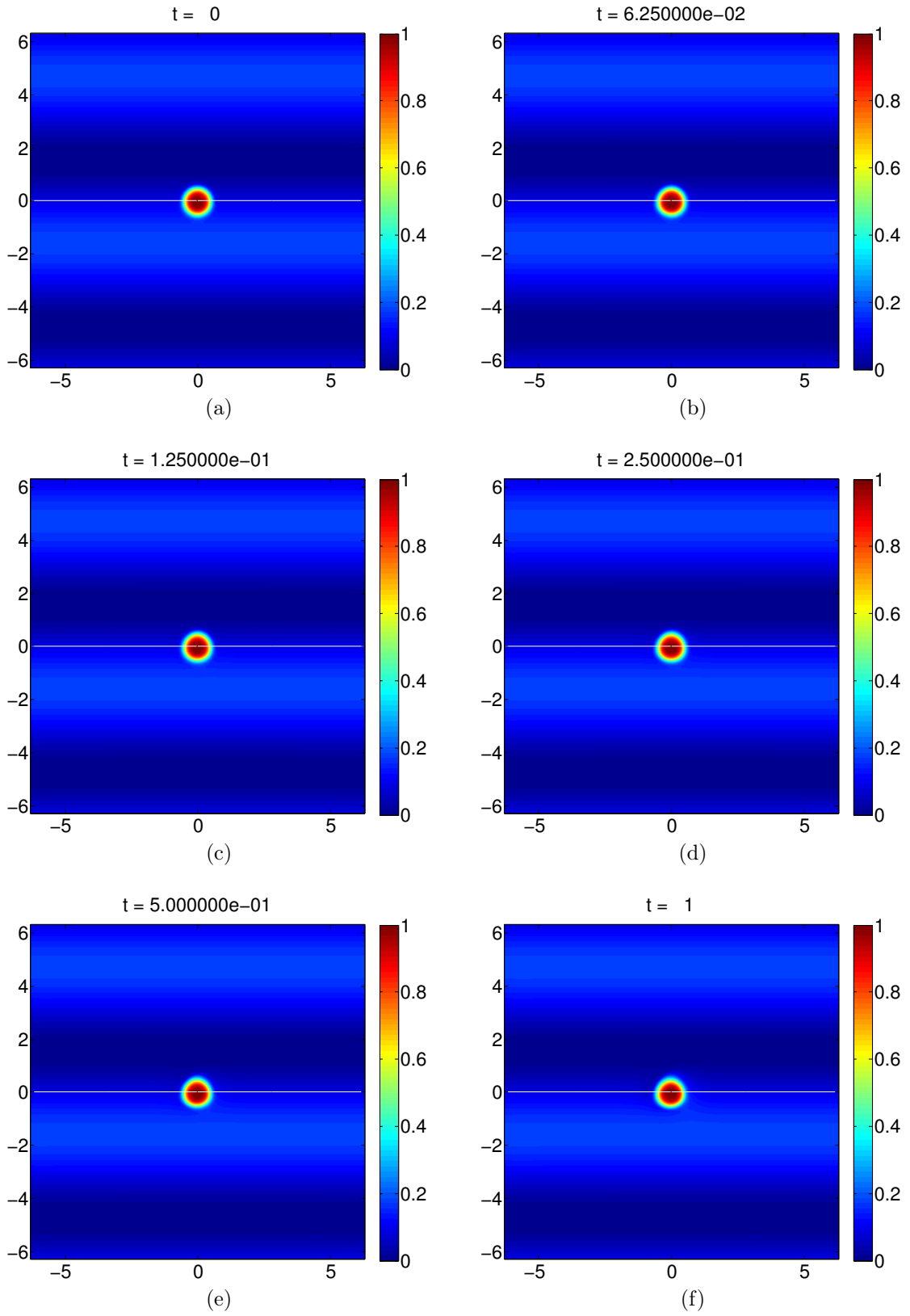

Figure 3-43: $A = 10$, $a = \pi/6$, $R_d/a = 0.625$, $y_o = \pi/2$, $\beta = 0$.

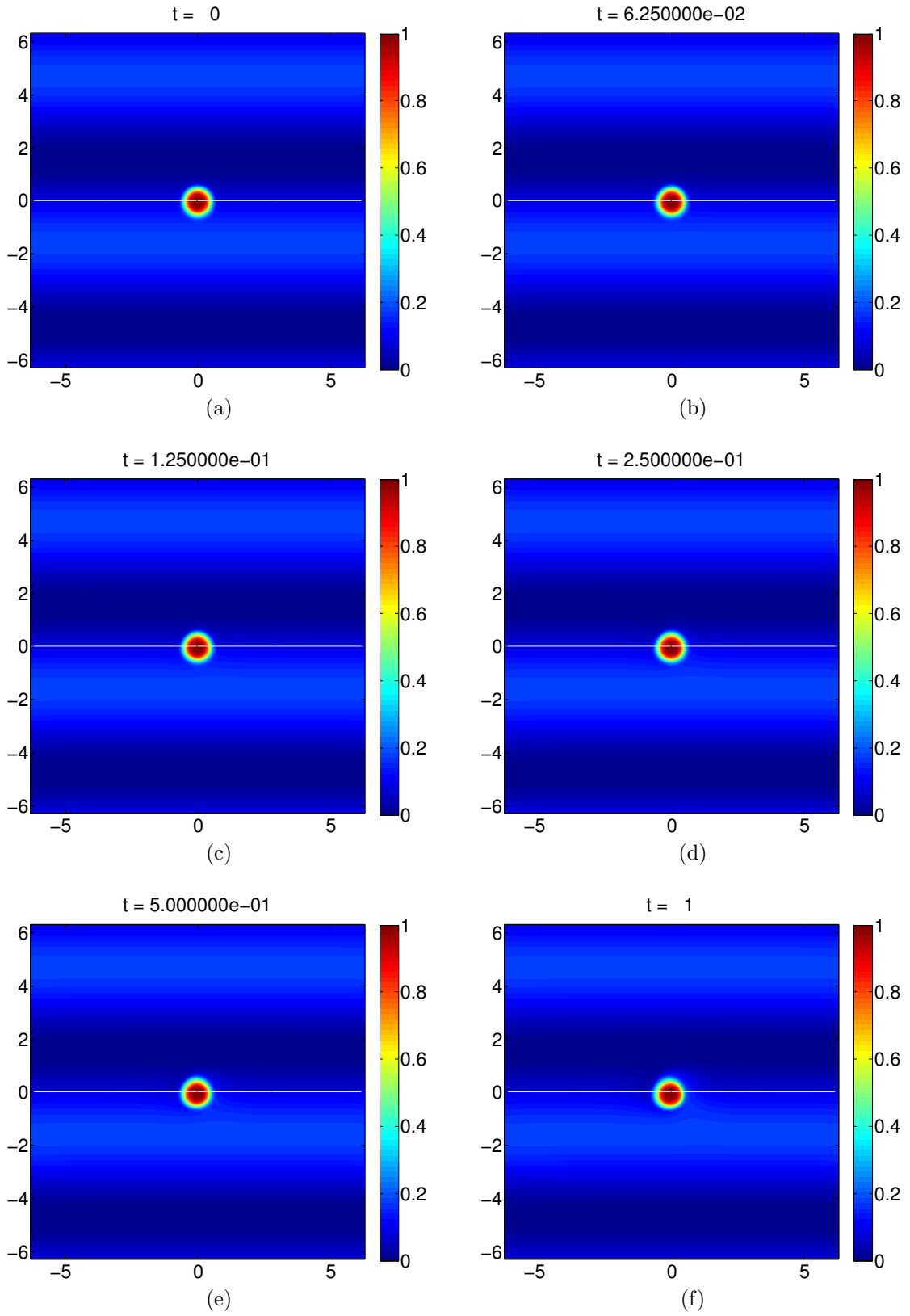

Figure 3-44: $A = 10$, $a = \pi/6$, $R_d/a = 1$, $y_o = \pi/2$, $\beta = 0$.

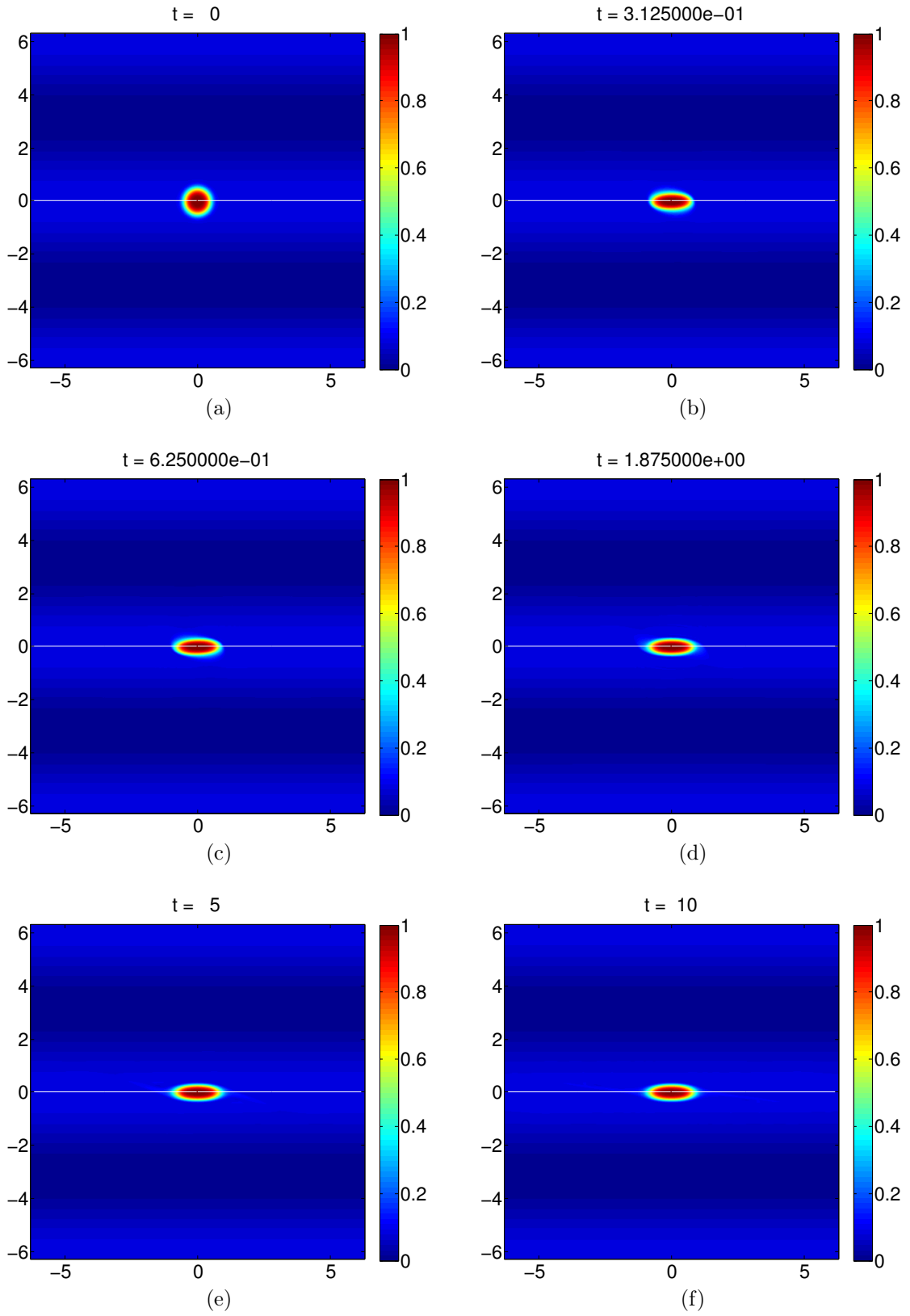

Figure 3-45: $A = 20$, $a = \pi/6$, $R_d/a = 0.25$, $y_o = 0$, $\beta = 0$.

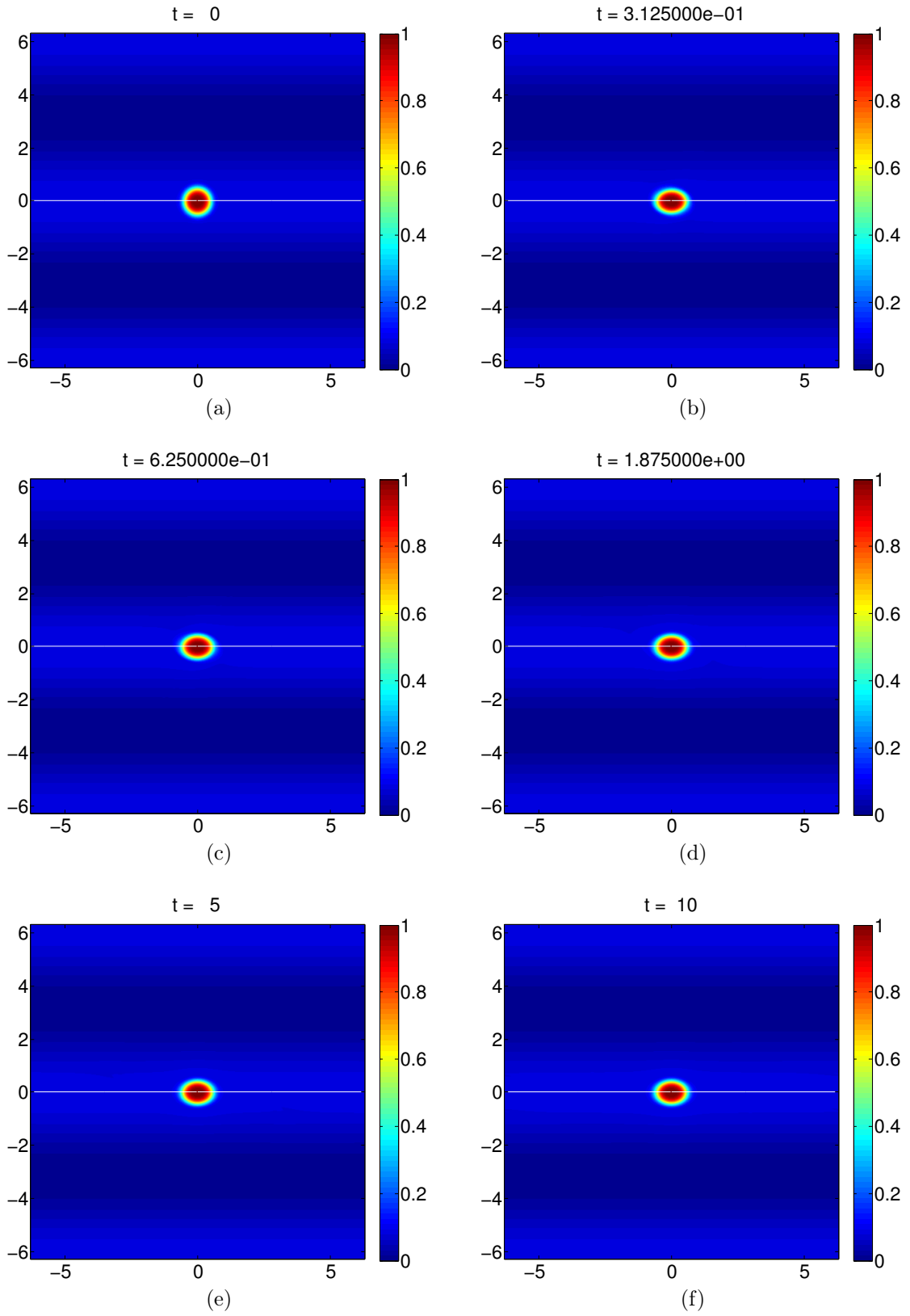

Figure 3-46: $A = 20$, $a = \pi/6$, $R_d/a = 0.625$, $y_o = 0$, $\beta = 0$.

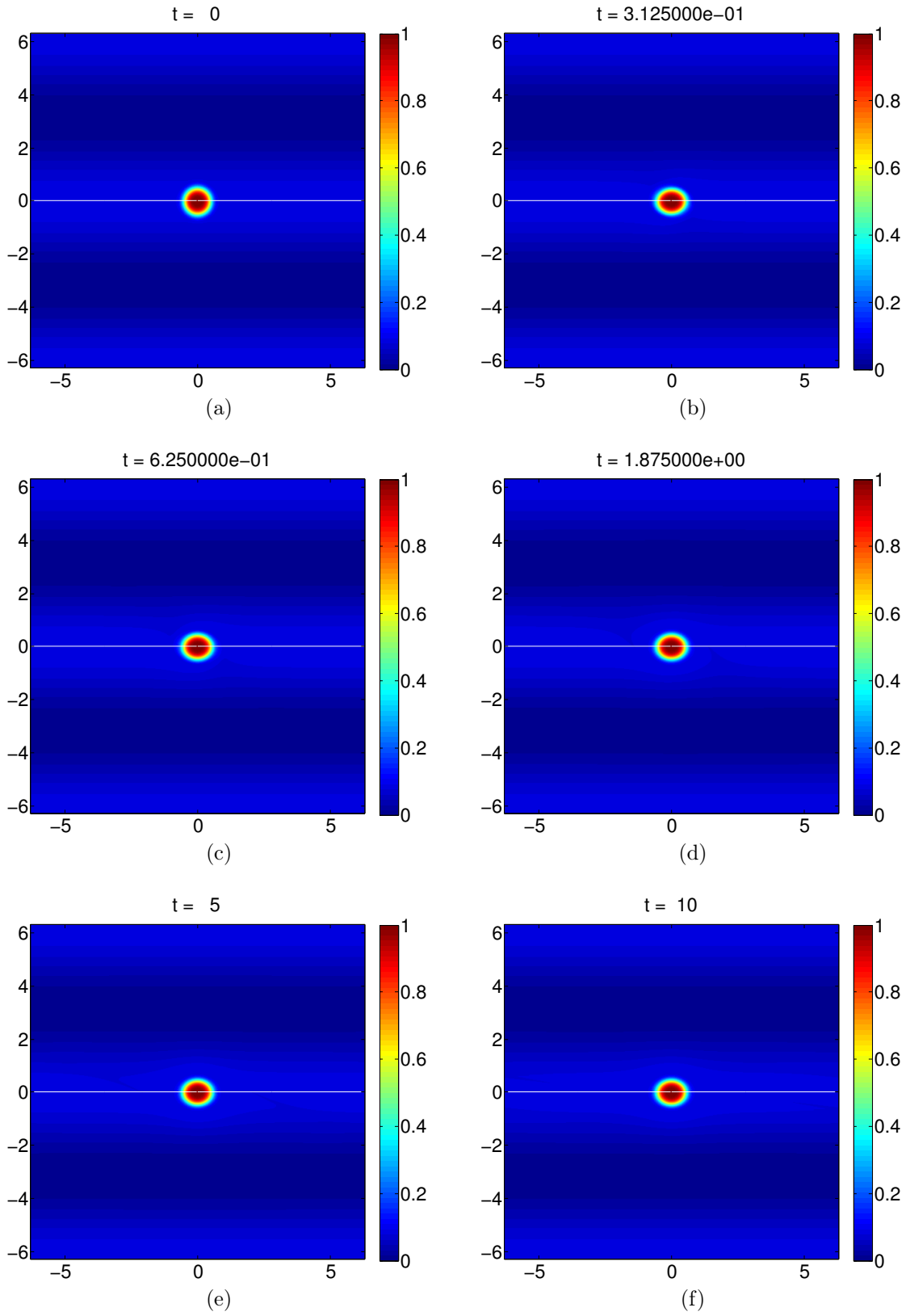

Figure 3-47: $A = 20$, $a = \pi/6$, $R_d/a = 1$, $y_o = 0$, $\beta = 0$.

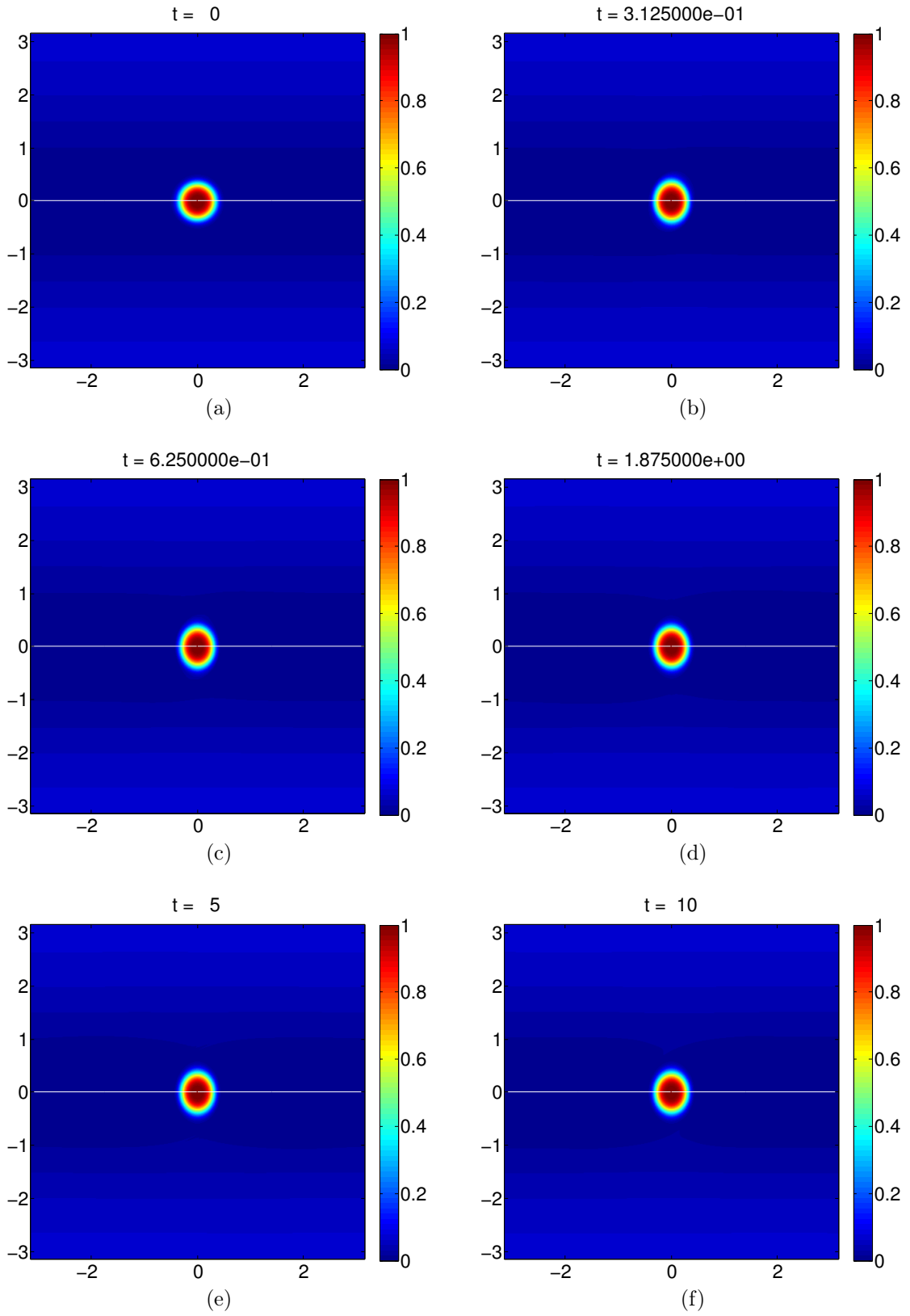

Figure 3-48: $A = 30$, $a = \pi/9$, $R_d/a = 1$, $y_o = \pi$, $\beta = 0$. Vortex in the adverse shear region.

Table 3.1: $a = \pi/9$ simulations

A	y_o	R_d/a	Comments
5	0	0.25	Steady
5	0	0.625	Steady
5	0	1	Steady
5	$\pi/4$	0.25	Steady/Quasi-steady
5	$\pi/4$	0.625	Steady/Quasi-steady
5	$\pi/4$	1	Unsteady, drift, translation
5	$\pi/2$	0.25	linear Hamiltonian, skewness linear, little drift, little translation
5	$\pi/2$	0.625	linear Hamiltonian, drift linear, linear translation
5	$\pi/2$	1	linear Hamiltonian, drift linear, linear translation
10	0	0.25	Steady
10	0	0.625	Steady
10	0	1	Steady
10	$\pi/4$	0.25	Steady/Quasi-steady
10	$\pi/4$	0.625	Steady/Quasi-steady
10	$\pi/4$	1	Unsteady, drift, translation
10	$\pi/2$	0.25	linear Hamiltonian, skewness linear, little drift, trnsln.
10	$\pi/2$	0.625	linear Hamiltonian, linear drift, linear translation
10	$\pi/2$	1	linear Hamiltonian, linear drift, linear translation
20	0	0.25	Steady
20	0	0.625	Steady
20	0	1	Steady
20	$\pi/4$	0.25	Steady/Quasi-steady
20	$\pi/4$	0.625	Steady/Quasi-steady
20	$\pi/4$	1	Unsteady, drift, translation
20	$\pi/2$	0.25	linear Hamiltonian, skewness linear, little drift, trnsln.
20	$\pi/2$	0.625	linear Hamiltonian, linear drift, linear translation
20	$\pi/2$	1	linear Hamiltonian, linear drift, linear translation

Table 3.2: $a = \pi/6$ simulations

A	y_o	R_d/a	Comments
5	0	0.25	Steady
5	0	0.625	Steady
5	0	1	Steady
5	$\pi/4$	0.25	Steady/Quasi-steady
5	$\pi/4$	0.625	Steady/Quasi-steady
5	$\pi/4$	1	Unsteady, drift, translation
5	$\pi/2$	0.25	linear Hamiltonian, linear skewness, little drift, little translation
5	$\pi/2$	0.625	linear Hamiltonian, linear drift, linear translation
5	$\pi/2$	1	linear Hamiltonian, linear drift, linear translation
10	0	0.25	Steady
10	0	0.625	Steady
10	0	1	Steady
10	$\pi/4$	0.25	Steady/Quasi-steady
10	$\pi/4$	0.625	Steady/Quasi-steady
10	$\pi/4$	1	Unsteady, drift, translation
10	$\pi/2$	0.25	Tine, Hamiltonian>linear, linear skewness, little drift, trnsln.
10	$\pi/2$	0.625	linear Hamiltonian, linear drift, linear translation
10	$\pi/2$	1	linear Hamiltonian, linear drift, linear translation
20	0	0.25	Steady
20	0	0.625	Steady
20	0	1	Steady

Chapter 4

Conclusion

Thus, we have been able to obtain steady states for vortices embedded in a sinusoidal shear flow using the optimization technique of Hamiltonian Dirac simulated annealing in a 1.75 layer quasi-geostrophic framework. To complement and contrast these results, we have also presented original Hamiltonian dynamics simulations.

Although the original Hamiltonian dynamics simulations are rich, we find that there is a measurable loss of enstrophy through filamentation and instabilities. Most of the instabilities occur on route to the apparent steady state. Thus the area of the final steady or quasi-steady vortex if any is reduced from the initial area.

Since the area between two vorticity contours is preserved in the HDSA simulations, we overcome the problems faced in the H simulations and obtain vortex steady/quasi-steady states that have roughly the same area as we initially started out with. Further, the SA and HDSA simulations allowed us to explore a much wider range of steady state parameters since the vortices remained stable on route to the steady/quasi-steady state or shape.

By constraining the x and y centers of potential vorticity for vortex positions other than $y_o = 0$, we are able to prevent the vortex from jumping to the $y_o = 0$ position ($y_o = 0$ represents an energy extremum), thereby giving the vortex a chance to settle into a steady state.

We have given simulations for the following range of parameters : $5 \leq A \leq 20$,

$\pi/9 \leq a \leq \pi/3$, $0.25 \leq R_d/a \leq 1$ and $0 \leq y_o \leq \pi/2$, $\beta = 0$. We have not yet incorporated the non-zero β case.

We uniformly obtained elliptical steady states for the $y_o = 0$ simulations. It looks like the symmetry in background vorticity holds the vortex in place. The aspect ratio or the ellipticity decreases as R_d increases. Further, the ellipticity increases as the size of the vortex increases.

For $y_o = \pi/4$, we got a mix of the $m = 2$ and $m = 3$ modes, especially for $a = \pi/3$ since it can sense the curvature in the flow. On that note, we must point out that $A = 10$ or $A = 20$ is too high a value for magnitude of vorticity in the $a = \pi/3$ case to give steady states. Also, a large value of A combined with a large value of R_d lead to the vortex dominating over the background. Thus the vortex wraps the background vorticity around itself and drifts south and translates west in such cases. We tried $A = 2$ and found it to be a much better value for $a = \pi/3$.

We find that the position $y_o = \pi/2$ is not conducive to steady states. In fact all $y_o = \pi/2$ simulations uniformly led to a continuous increase in the Hamiltonian, and the vortex drifted South and translated west. This suggests that there do not exist any steady states at that latitude. It must be pointed out that although we are not able to find vortex steady states at $y_o = \pi/2$, we still obtain the characteristic triangle shaped vortices, especially for the $R_d/a = 0.25$ cases. Further $R_d/a = 1$ leads to translation and drifting in all the $y \neq 0$ cases.

The results so far suggest many avenues of future work. For example a non-zero β value had in fact held the vortex at $y_o = \pi/2$ in the original Hamiltonian dynamics simulations. We believe that the β plane can be incorporated by bringing in a boundary layer for f since we need the latter to be periodic in the HDSA framework. However, we expect this to be tricky to code.

With these steady or quasi-steady states, we can now go ahead and give vortex merger simulations, where we have two or more vortices interacting in the presence of a background shear flow.

Appendix A

M-code

A.1 Simulated annealing and time stepping

```
%%%%%%%%%%%%%%%%
switch(nx)
    case 128
      cphi = 0.69*pi;
    case 256
      cphi = 0.715*pi;
    case 512
      cphi = 0.735*pi;
    otherwise
      cphi = 0.65*pi;
end

wvx=sqrt((k*dx).^2+(l*dy).^2);
%exponential cut-off filter for single and double precision respectively
%filtr=exp(-18*(wvx-cphi).^7).*(wvx>cphi)+(wvx<=cphi);
filtr=exp(-37*(wvx-cphi).^7).*(wvx>cphi)+(wvx<=cphi);
filtr(isnan(filtr))=1;
%truncating at Nyquist wavenumber for de-aliasing
```

```
kmax2=((nx/2-1)*k0x).^2;
trunc=(wv2<kmax2);

%%%%%%%%%%%%%%%%%%%%%%%%%

t=0;
tc=0;

qh1=fft2(q1);
qh2=fft2(q2);

dqh1dt_p=0;
dqh2dt_p=0;
dt0=dt;dt1=0;

while t<=tmax+dt/2
  %truncating for dealiasing
  q1=real(ifft2(qh1.*trunc));
  %inverting {\nabla}^2-F operator to get q1-F*p2
  [ph1,ph2]=invert(qh1,qh2,a11,a12,a21,a22);
  %calculating u1 for advection
  [u1,v1]=caluv(ph1,k,l,trunc);
  p1=real(ifft2(ph1.*trunc));
  %advecting q1 with u1 to get [q,psi]
  dqh1dt=-advect(q1,u1+U1,v1,k,l)-beta1*1i*k.*ph1;

%%%%%%%%%%%%%%%%%%%%%%%%%
%  Simulated Annealing SA
%%%%%%%%%%%%%%%%%%%%%%%%%
  %%calculating modified streamfunction phi from q1dot by inverting laplacian
%   pah1=invertlap(dqh1dt,det2);
  %%calculating u1 from phi for advection
%   [u1,v1]=caluv(pah1,k,l,trunc);
   %%calculating [q,phi]
%   dqah1dt=-advect(q1,u1+U1,v1,k,l)-beta1*1i*k.*pah1;
```

```
%%%%%%%%%%%%%%%%%%%%%%%%%
%  End of SA
%%%%%%%%%%%%%%%%%%%%%%%%%

%%%%%%%%%%%%%%%%%%%%%%%%%%%%%%%%
%  Dirac Simulated Annealing DSA
%%%%%%%%%%%%%%%%%%%%%%%%%%%%%%%%
  %calculating [c1,c2]
  bc1c2=intint(q1,jc1c2,dx);
  %truncating [q,psi]
  bq1h=real(ifft2(dqh1dt.*trunc));
  %calculating [psi,q1]-([psi,c2][c1,q1]-[psi,c1][c2,q1])/[c1,c2]
  %function intint just integrates over domain
  aa1=-intint(c2,bq1h,dx)/bc1c2;
  aa2=intint(c1,bq1h,dx)/bc1c2;
  dqh1dt=advect1(q1,dqh1dt,k,l,aa1,aa2,c1x,c1y,c2x,c2y);

  %calculating modified streamfunction phi from q1dot by inverting laplacian
  pah1=invertlap(dqh1dt,det2);
  %calculating u1 from phi for advection
  [u1,v1]=caluv(pah1,k,l,trunc);
  %calculating [q,phi]
  dqah1dt=-advect(q1,u1+U1,v1,k,l)-beta1*1i*k.*pah1;

  %truncating [q,phi]
  bq1h=real(ifft2(dqah1dt.*trunc));
  %calculating [phi,q1]-([phi,c2][c1,q1]-[phi,c1][c2,q1])/[c1,c2]
  %function intint just integrates over domain
  bb1=-intint(c2,bq1h,dx)/bc1c2;
  bb2=intint(c1,bq1h,dx)/bc1c2;
  dqah1dt=advect1(q1,dqah1dt,k,l,bb1,bb2,c1x,c1y,c2x,c2y);%
%%%%%%%%%%%%%%%%%%%%%%%%%%%
%  End of DSA
%%%%%%%%%%%%%%%%%%%%%%%%%%%
  %SA or DSA
```

```
89    %combining ideal and dissipative dynamics
90    dqh1dt=beta11*dqh1dt+alpha11*dqah1dt;
91    %Filtering the small scales and update q1 by advecting with modified
92    %streamfunction
93    qh1=filtr.*(qh1+dt0*dqh1dt+dt1*dqh1dt_p);
94
95    dqh1dt_p=dqh1dt;
96
97    if tc==0
98      %coefficients for AB2
99      dt0=1.5*dt;dt1=-0.5*dt;
100   end
101   tc=tc+1;
102   t=tc*dt;
103
104 end
```

A.2 Advection

```
1  function qdot=advect(q,u,v,k,l)
2    qdot=1i*k.*fft2(u.*q)+1i*l.*fft2(v.*q);
```

```
1  function qdot3=advect1(q,qdot2,k,l,ab1,ab2,c1x,c1y,c2x,c2y)
2    qdot3=qdot2-1i*k.*fft2((-ab1*c1y-ab2*c2y).*q)-1i*l.*fft2((ab1*c1x+ab2*c2x).*q);
```

Bibliography

C. Canuto, M. Y. Hussaini, A. Quarteroni, and T. A. Zang. *Spectral Methods : Fundamentals in Single Domains*. Springer, 2006.

D. Choi, D. Banfield, P. J. Gierasch, and A. Showman. Velocity and vorticity measurements of Jupiter's Great Red Spot using Automated Cloud Feature Tracking. *Icarus*, 188:35–46, 2007.

T. E. Dowling and A. P. Ingersoll. Potential Vorticity and layer thickness variations in the flow around jupiter's great red spot and white oval bc. *J. Atmos. Sci.*, 45 (8):1380–1396, 1988.

T. E. Dowling and A. P. Ingersoll. Jupiter's Great Red Spot as a Shallow Water system. *J. Atmos. Sci.*, 46(21):3256–3278, 1989.

G. R. Flierl and P. J. Morrison. Hamiltonian-Dirac simulated annealing: Application to the calculation of vortex states. *Physica D*, 240:212–32, 2011.

R. Hide. Origin of Jupiter's Great Red Spot. *Nature*, 190(4779):895–896, 1961.

A. P. Ingersoll. Inertial columns and Jupiter's Great Red Spot. *J. Atmos. Sci.*, 26: 744–752, 1969.

A. P. Ingersoll. Atmospheric dynamics of the outer planets. *Science*, 248:308–315, 1990.

A. P. Ingersoll and P. G. Cuong. Numerical model of long-lived Jovian vortices. *J. Atmos. Sci.*, 38(10):2067–2076, 1981.

A. P. Ingersoll and D. Pollard. Motion in the interiors and Atmospheres of Jupiter and Saturn: Scale analysis, anelastic equations, Barotropic stability criterion. *Icarus*, 52:62–80, 1982.

A. P. Ingersoll, P. J. Gierasch, D. Banfield, A. R. Vasavada, and the Galileo Imaging Team. Moist convection as an energy source for the large-scale motions in Jupiter's atmosphere. *Icarus*, 403:630–632, 2000.

S. Kida. Motion of an Elliptic vortex in a uniform shear flow. *J. Phys. Soc. Jpn.*, 50 (10):3517–3520, 1981.

M.-M. Mac Low and A. P. Ingersoll. Merging of vortices in the atmosphere of Jupiter: An analysis of Voyager images. *Icarus*, 65:353–369, 1986.

P. S. Marcus. Numerical simulation of Jupiter's Great Red Spot. *Nature*, 331:693–696, 1988.

P. S. Marcus. Vortex dynamics in a shearing zonal flow. *J. Fluid Mech.*, 215:393–430, 1990.

P. S. Marcus. Jupiter's Great Red Spot and other vortices. *Annu. Rev. Astron. Astrophys.*, 31:523–573, 1993.

T. Maxworthy and L. G. Redekopp. A solitary wave theory of the Great Red Spot and other observed features in the jovian atmosphere. *Icarus*, 29:261–271, 1976.

S. P. Meacham, G. R. Flierl, and U. Send. Vortices in shear. *Dyn. Atmos. Oceans*, 14:333–386, 1989.

J. L. Mitchell, R. J. Terrile, B. A. Smith, J. P. Muller, G. E. Hunt A. P. Ingersoll, S. A. Collins, and R. F. Beebe. Jovian cloud structure and velocity fields. *Nature*, 280:776–778, 1979.

J. L. Mitchell, R. F. Beebe, A. P. Ingersoll, and G. W. Garneau. Flow fields within Jupiter's Great Red Spot and White Oval BC. *J. Geophys. Res.*, 86:8751–8757, 1981.

D. W. Moore and P. G. Saffman. Structure of a line vortex in an imposed strain. In J. Olsen, A. Goldberg, and N. Rogers, editors, *In Aircraft Wake Turbulence and its Detection*. New York: Plenum, 1971.

P. J. Morrison. Poisson bracket for fluids and plasmas. In Tabor and Treve (1982).

P. J. Morrison. Hamiltonian description of the ideal fluid. In R. Salmon and B. Ewing-DeRemer, editors, *1993 Summer Study Program in Fluid Dynamics*, GFD summer school. Woods Hole Oceanographic Institution, 1993.

J. Pedlosky. *Geophysical Fluid Dynamics*. Springer-Verlag, second edition, 1987.

P. B. Rhines and B. Young. Homogenization of potential vorticity in planetary gyres. *J. Fluid Mech.*, 122:347–367, 1982.

A. A. Simon-Miller, P J. Gierasch, R F. Beebe, B. Conrath, F. Michael Flasar, R. K. Achterberg, and the Cassini CIRS Team. New observational results concerning Jupiter's Great Red Spot. *Icarus*, 158:249–266, 2002.

B. A. Smith, L. A. Soderblom, R. F. Beebe, G. A. Briggs J. Boyce, M. H. Carr, S. A. Collins, A. F. Cook 11, G. E. Danielson, M. E. Davies, G. E. Hunt, A. P. Ingersoll, T. V. Johnson, H. Masursky, J. F. McCauley, D. Morrison, T. Owen, C. Sagan, E. M. Shoemaker, R. Strom, V. E. Suomi, and J. Veverka. The galilean satellites and jupiter: Voyager 2 imaging science results. *Science*, 206(4421):927–950, 1979a.

B. A. Smith, L. A. Soderblom, T. V. Johnson, A. P. Ingersoll, S. A. Collins, E. M. Shoemaker, G. E. Hunt, H. Masursky, M. H. Carr, M. E. Davies, A. F. Cook 11, J. Boyce, G. E. Daniel-son, T. Owen, C. Sagan, R. F. Beebe, J. Veverka, R. G. Strom, J. F. McCauley, D. Morrison, G. A. Briggs, and V. E. suomi. The jupiter system through the eyes of voyager 1. *Science*, 204(4396):951–972, 1979b.

J. Sommeria, S. D. Meyers, and H. L. Swinney. Laboratory simulation of Jupiter's Great Red Spot. *Nature*, 331:689–693, 1988.

M. Tabor and Y. Treve, editors. *Mathematical methods in hydrodynamics and integrability in dynamical systems*, AIP Conf. Proc., 1982. Am. Inst. Phys., New York.

G. K. Vallis, G. Carnevale, and W. R. Young. Extremal energy properties and construction of stable solutions of the Euler equations. *J. Fluid. Mech*, 207:133–152, 1989.